Computational Studies of Unsteady Flow in Arterio-Venous Fistulae

by

Lorenza Grechy

Department of Aeronautics

Imperial College London, South Kensington Campus, London

SW7 2AZ, United Kingdom

This thesis is submitted for the degree of

Doctor of Philosophy of Imperial College London

Abstract

Arterio-venous fistulae (AVF) are surgically created vascular connections between an artery and a vein in patients with End Stage Renal Disease, and are regarded as the 'gold standard' method of vascular access for patiets who require haemodialysis. However, up to 60% of AVF do not mature, and hence fail, as a result of various pathologies such as Intimal Hyperplasia (IH).

Highly oscillatory flow patterns are one of the factors implicated in the development of IH, and they will be studied in this thesis. Previous studies have investigated the effect of arterial curvature on blood flow in AVF using idealised (planar) AVF configurations and non-pulsatile inflow conditions. These studies are extended here to more realistic non-planar AVF configurations with pulsatile inflow conditions. Results show that, converse to previous findings, forming an AVF by connecting a vein onto the outer curvature of an arterial bend does not, necessarily, suppresses unsteady flow in the artery.

Subsequently, an optimisation process for idealised 3-dimensional geometries is introduced to identify an optimal configuration that suppress high-frequency fluctuations under steady inflow. Performance of the optimal configuration is then successfully verified with a fully pulsatile simulation. A novel medical device for maintaining AVF in the optimal shape is also proposed, and a first animal experiment is reported as a proof of principle study, which led to promising preliminary results.

Finally, realistic AVF geometries are reconstructed from 60 MRI scans. Ul-

trasound measurements of the flow were also collected, together with details of patient outcomes, so that computational simulations could investigate the relationships between geometrical features, flow unsteadiness and AVF maturation. Results show high variability of the geometric parameters between AVF formed in the upper arm and AVF formed in the wrist. Also, some geometric parameters in upper arm AVF resulted to be correlated with flow stabilisation and AVF maturation. However results were found to be not statistically significant.

Acknowledgements

First and foremost I would like to thank Dr. Peter Vincent who has given me the opportunity to undertake a PhD under his supervision. He has always been very supportive and has motivated me through the whole project with his precious feedbacks and his contagious enthusiasm. I am especially grateful for the freedom he has given me to pursue this research, knowing at the same time how and when advice me to guide this research toward a coherent story. I would also like to thank my co-supervisor Prof. Colin Caro. I am extremely grateful for the support he has always provided me, with his kind feedbacks and suggestions.

My sincere thanks go to Dr. Richard Corbett, especially for all the hours we spent together analysing the patient's data, and to the rest of the Renal Group, Prof. Neill Duncan and Prof. Wady Wladyslaw for the insights they provided during our monthly meetings. I am very grateful for the technical help of Roland Hutchins, Alan Smith and Jonathan Cole, who helped me with 3d-printing the vascular device prototype, and with the first attempt of mould for the final device.

I would also like to express my sincere gratitude to the EPSRC for funding this project, and for allowing me to continue it during the next year, and to the Imperial College High Performance Computing service, for provifing some of the computer resources used in this work.

I thank Francesco Iori, a brilliant researcher and a wonderful partner. I cannot be grateful enough for all the help, both technical and emotional, he has given me during these years. Without his love and his careful attentions this project

would have been immensely more difficult.

A special thanks go to my sister Alice, who I have always felt close, despite living in different cities. Finally, I would like to thank my parents, my father Carlo and my mother Maria Cristina. They have always encouraged me during the studies, and our almost daily Skype conversations have been of great support in these years.

Declaration of Originality

The work presented in this thesis comprises only my original work and does not contain material which to a substantial extent has been accepted for the award of any other degree or diploma of the university or other institute of higher learning, except where due acknowledgement has been made in the text.

Copyright Declaration

The copyright of this thesis rests with the author and is made available under a Creative Commons Attribution Non-Commercial No Derivatives licence. Researchers are free to copy, distribute or transmit the thesis on the condition that they attribute it, that they do not use it for commercial purposes and that they do not alter, transform or build upon it. For any reuse or redistribution, researchers must make clear to others the licence terms of this work.

Nomenclature

Abbreviations

LWNOF$^-$ Potentially Pathologically Low $\overline{q}_t$

WSS$^+$ Potentially Pathologically High $\overline{\boldsymbol{\tau}}_t$

WSS$^-$ Potentially Pathologically Low $\overline{\boldsymbol{\tau}}_t$

AVF Arterio-Venous Fistula

AVG Arterio-Venous Graft

BAI Brachial Arterial Inlet

BB Black blood acquisition mode

BBF Brachio-Basilic Fistula

BCF Brachio-Cephalic Fistula

CFD Computational Fluid Dynamics

CVC Central Venous Catheter

DA Distal Artery

DAO Distal Arterial Outlet

DMD Dynamic Mode Decomposition

DVO Distal Venous Outlet

ESRD End Stage Renal Disease

FA MRI flip angle

HD Haemodialysis

IFIR Inhance inflow inversion recovery acquisition mode

IH Intimal Hyperplasia

IN Inner Configuration

LHS Latin Hypercube Sampling

LWNOF Lumen-to-Wall Normal Oxygen Flux

MADS Mesh Adaptive Direct Search

MISR Cross-sectional Maximum Inscribed Sphere Radius

OSI Oscillatory Shear Index

OUT Outer Configuration

P1 Patient 1

P2 Patient 2

PA Proximal Artery

PAI Proximal Arterial Inlet

PD Peritoneal Dialysis

POD Proper Orthogonal Decomposition

PSD Power Spectral Density

PTFE Polytetrafluro-Ethylene

RAO Radial Arterial Outlet

RCF Radio-Cephalic Fistula

RRT Renal Replacement Therapy

SMC Smooth Muscle Cells

TAWSS Time Averaged WSS

TE MRI echo time

TR MRI repetition time

UAO Ulnar Arterial Outlet

VENC Velocity encoding acquisition mode

VO Venous Outlet

WD Dyastolic Temporal Window

WS Systolic Temporal Window

WSS Wall Shear Stress

WSS-RRT WSS-Relative-Residence-Time

WT Full Pulse Period

Constants

μ Blood Viscosity

ρ Blood Density

K Oxygen Diffusivity in Plasma

Dimensionless Numbers

De Dean Number

Pe Peclet Number

Re Reynolds Number

Sc Schmidt Number

Wo Womersley Number

Operators

$\cup$ Union

$\boldsymbol{\nabla}$ Nabla

Subscripts

W Wall

A Artery

BAI Brachial Arterial Inlet

DA Distal Artery

DAO Distal Arterial Outlet

DVO Distal Venous Outlet

L Lofted

PA Proximal Artery

PAI Proximal Arterial Inlet

R Realistic

RAO Radial Arterial Outlet

UAO Ulnar Arterial Outlet

V Vein

VO Venous Outlet

Symbols

α	Bifurcation Angle between $\mathbf{x}_A$ and $\mathbf{x}_V$
$\chi_{[]}$	Planarity Index of []
$\delta_{[]}$	Non-Dimensional Centerline Curvature in []
γ	DMD Intensity
κ	Centerline Curvature
$\mathbf{B}$	Frenet Binormal Vector
$\mathbf{m}_{[]}$	Tangent versor in []
$\mathbf{N}$	Frenet Normal Vector
$\mathbf{O}$	Origin
$\mathbf{p}_{[]}$	Centerline point in []
$\mathbf{s}$	parameter set
$\mathbf{S}_k$	Set of tried parameters at step k
$\mathbf{S}_L$	Lofted Surfaces
$\mathbf{S}_R$	Realistic Surfaces
$\mathbf{T}$	Frenet Tangent Vector
$\mathbf{u}$	Blood Velocity
$\mathbf{x}_{[]}$	centerline of []
$\overline{\psi}_t(\mathbf{x})$	Time-Average of $\psi(\mathbf{x}, t)$
$\overline{\boldsymbol{\tau}}_t$	Time-averaged WSS
$\overline{\boldsymbol{\tau}}_{tS}$	Space-Time-averaged WSS
$\overline{q}_t$	Time-averaged LWNOF
$\overline{q}_{tS}$	Space-Time-averaged LWNOF
$\overline{u}_{[]}$	Section-Averaged velocity in []
ϕ	Polar Angle of the Venous Tangent in $\mathbf{O}$
Ψ	Cost Function which quantifies Flow Stability
$\psi(\mathbf{x}, t)$	Indicator function of $\tau_D(\mathbf{x}, t)$
$\boldsymbol{\tau}$	WSS vector
$\tau_D(\mathbf{x}, t)$	Percentage difference of WSS magnitude between steady and unsteady simulation
θ	Azimuthal Angle of the Venous Tangent in $\mathbf{O}$
$\widetilde{\mathbf{S}}_k$	Set of feasible tried parameters at step k
ξ	Paramater for the position of $\mathbf{p}_3$
c	Oxygen Concentration
$C_{[]}$	Vascular Capacitance at []
$D_{[]}$	Mean diameter of the region []
d_p	Deviation of the perimeter rate between realistic and lofted geometries
$L_{[]}$	Vascular Inductance at []
p	Section Perimeter
$P_{[]}$	Section-Averaged Pressure in []
$Q_{[]}$	Section-Averaged Flow in []
$R_{[]}$	Vascular Resistance at []
s	Arc Length of a Curve
t_0	Day of surgery

t_1	Period between 7 and 14 days since surgery
t_c	Simulation Characteristic Time
$W(\mathbf{S}_k)$	Set of unfeasible tried parameters at step k

Contents

1 Introduction **21**

1.1 Background 21

1.2 Thesis Overview 22

1.3 Resulting Publications 24

2 Literature Review **26**

2.1 Arterio-Venous Fistulae 26

2.1.1 End Stage Renal Disease Treatment 26

2.1.2 Vascular Access for Haemodialysis 27

2.2 Arterio-Venous Fistula Maturation 29

2.3 Complications and Failure 30

2.3.1 Intimal Hyperplasia 31

2.3.2 Wall Shear Stress and Intimal Hyperplasia 32

2.3.3 Blood Flow Unsteadiness and Intimal Hyperplasia 34

2.3.4 Hypoxia and Intimal Hyperplasia 35

2.4 Computational Fluid Dynamics 36

2.4.1 Computational Fluid Dynamics in Anastomotic Connections 36

2.4.2 Flow Unsteadiness Measurements through Computational Fluid Dynamics 40

2.4.3 Oxygen Transport and Computational Fluid Dynamics . . 42

3 The Effect of Arterial Curvature on Blood Flow in Arterio-Venous Fistulae: Realistic Geometries and Pulsatile Flow 44

3.1 Introduction . . . 44

3.2 Methods . . . 45

3.2.1 Geometries . . . 45

3.2.1.1 Native Vessels . . . 45

3.2.1.2 Forming an Arterio-Venous Fistulae . . . 47

3.2.2 Governing Equations . . . 48

3.2.2.1 Blood Flow . . . 48

3.2.2.2 Oxygen Transport . . . 49

3.2.2.3 Non-Dimensional Quantities . . . 49

3.2.3 Boundary Conditions . . . 50

3.2.3.1 Blood Flow . . . 50

3.2.3.2 Oxygen Transport . . . 54

3.2.4 Computational Method . . . 55

3.2.4.1 Mesh Independence . . . 56

Polyhedral Unstructured Volume Mesh . . . 56

Prismatic Boundary Layer Mesh . . . 60

3.2.4.2 Period Independence . . . 61

3.3 Results . . . 63

3.3.1 Unsteady Analysis . . . 63

3.3.1.1 Qualitative Insight . . . 63

3.3.1.2 Quantitative Insight . . . 66

3.3.1.3 Summary . . . 68

3.3.2 Time-Averaged Analysis . . . 70

3.3.2.1 Wall Shear Stress and Wall Normal Oxygen Flux 70

3.3.2.2 Summary . . . 73

3.4 Conclusions . . . 73

4 Optimisation of Arterio-Venous Fistulae for Suppressing Unsteady Flow **74**

4.1 Introduction . . . 74

4.2 Optimisation . . . 75

4.2.1 Overview . . . 75

4.2.2 Parameterisation . . . 75

4.2.3 Cost Function . . . 78

4.2.3.1 Definition . . . 78

4.2.3.2 Computational Method . . . 79

4.2.4 Optimisation Framework . . . 80

4.2.4.1 Initial Seeding . . . 80

4.2.4.2 Mesh Adaptive Direct Search Method . . . 83

4.2.5 Results and Discussion . . . 88

4.3 Pulsatile Simulations . . . 93

4.3.1 Overview . . . 93

4.3.2 Governing Equations and Boundary Conditions . . . 93

4.3.2.1 Computational Method . . . 94

4.3.3 Results and Discussion . . . 95

4.3.3.1 Velocity and Vorticity . . . 95

4.3.3.2 Dynamic Mode Decomposition . . . 98

4.4 Conclusions . . . 100

5 A Device for Shaping Arterio-Venous Fistulae **101**

5.1 Introduction . . . 101

5.2 Methods . . . 101

5.2.1 Device Design . . . 101

5.2.2 Device Prototyping and Manufacturing . . . 102

5.2.3 Porcine Model . . . 104

5.3 Results . . . 107

5.4 Conclusions 108

6 Realistic Geometries and Flow Unsteadiness 110

6.1 Introduction 110

6.2 Methods 111

6.2.1 Image Acquisition 111

6.2.2 Image Segmentation and Geometry Reconstruction 113

6.2.3 Geometric Characterisation 116

6.2.4 Ultrasound Measurements 119

6.2.5 Computational Fluid Dynamics Simulations 120

6.2.5.1 Governing Equations 121

6.2.5.2 Boundary Conditions 121

6.2.5.3 Computational Method 122

6.3 Results I: Geometries and Clinical Measurements 123

6.3.1 Geometry Reconstruction 123

6.3.2 Anatomic Variability 126

6.3.2.1 Anatomic Variability and Arterio-Venous Fistulae Maturation 129

6.3.3 Ultrasound Measurements 133

6.4 Results II: Computational Fluid Dynamics Simulations 134

6.4.1 Blood Flow under Patient-Specific Boundary Conditions . 134

6.4.1.1 Blood Flow Unsteadiness 134

6.4.1.2 Blood Flow Sensitivity to Geometry Reconstruction 136

6.4.2 Blood Flow under Average Boundary Conditions 137

6.4.2.1 Blood Flow Unsteadiness 137

6.4.3 Blood Flow Unsteadiness and Anatomic Variability 138

6.4.4 Blood Flow Unsteadiness and Clinical Outcome 141

6.5 Discussion 142

7 Conclusions **145**

Bibliography **147**

Appendix A **166**

A.1 Simple Kriging 166

A.2 Dynamic Mode Decomposition 169

List of Figures

2.1 Example of BCF 28
2.2 Schematic Vessels with Intimal Hyperplasia 32

3.1 CT-scan Reconstructed Vessels 45
3.2 AVF Configurations Digitally Created 47
3.3 Windkessel Model 53
3.4 Flow Profiles at Boundaries 54
3.5 Grid Convergence: Simulated Time-Averaged WSS 58
3.6 Grid Convergence: Simulated time-averaged LWNOF 59
3.7 Grid Convergence: Surface-Time Averaged WSS and LWNOF . . 60
3.8 Prismatic Boundary Layer Convergence: Surface-Time Averaged WSS and LWNOF 61
3.9 Period Independence: P1-IN Time-Averaged WSS 62
3.10 Period Independence: P1-IN Time-Averaged LWNOF 62
3.11 Period Independence: P1-IN Characteristic Frequencies in T1 and T2 63
3.12 Plane-Normal Vorticity in Two Instants in Time 65
3.13 Arterial and Venous Regions 67
3.14 WSS Dynamic Mode Decomposition Intensity 68
3.15 Quad-Color Maps of Potentially Pathological Flow Patterns in Excised and Flattened Vascular Regions 70

3.16 Percentage Area of Potentially Pathological Flow Patterns 71

4.1 AVF Parameters 77
4.2 Latin Hypercube Sampling Simulations: Objective Function and AVF parameters 81
4.3 Subsample of Configurations Tried During the Initialisation Step . 82
4.4 MADS Flow Diagram 86
4.5 Objective Function and Vascular Parameters During the MADS Optimisation Framework 87
4.6 Optimal Configuration 89
4.7 Box Plots of the Parameters Associated with a Small Value of the Objective Function 91
4.8 Kriging Prediction Varying the Parameters from the Optimal Set 92
4.9 Boundary Flow Waveforms 94
4.10 Snapshots of the Velocity Magnitude 96
4.11 Snapshots of the Vorticity Magnitude 97
4.12 Snapshots of Blood Flow Streamlines Coloured by Velocity Magnitude 98
4.13 Dynamic Mode Decomposition Intensity of WSS 99
4.14 Power Spectral Density of the Inflow 99

5.1 CAD Model of a Device for Holding AVF 103
5.2 3d-Printed Device for Holding AVF 104
5.3 Device implanted in a Swine Model 106
5.4 PSD of the Stethoscope Recording Before and After Implanting the Device 108

6.1 Cohort Study Diagram 112
6.2 Reconstruction of an AVF from MRI 115

6.3 Example of Vascular Curvature, Fistula Angle, and Non-Planarity Measurements 118
6.4 Flow Chart summarising the simulations run for each patient and the results analysis. 121
6.5 Frontal View of the Reconstructed AVF 124
6.6 Transversal View of the Reconstructed AVF 125
6.7 Sagittal View of the Reconstructed AVF 126
6.8 Geometric Parameters wich Correlates with AVF Maturation . . . 129
6.9 Comparison of MRI Reconstructed Geometries at t_0 and at t_1 . . 131
6.10 Unsteadiness Quantification via Dynamic Mode Decomposition and Function Ψ 134
6.11 Geometric Differences in the Reconstruction Method and Predicted Blood Flow 137
6.12 Steady Geometries 138
6.13 AVF Angle and Curvature in Steady and Unsteady Geometries . . 139
6.14 AVF Planarity in Steady and Unsteady Geometries 140
6.15 AVF Failure Rate in Steady and Unsteady Geometries 142

List of Tables

3.1 Windkessel Parameters 53

3.2 Grid Convergence: element dimensions 57

3.3 Prismatic Boundary Layer Convergence: Number of Layers 60

4.1 Optimal Parameter Values 88

6.1 Mean Value and Standard Deviation of the Geometric Parameters Values for AVF at t_0 127

6.2 Geometrical Parameters at t_0 and at t_1 132

6.3 US Measurements at t_0 133

6.4 Mature and Non-Mature AVF Divided by AVF Position and Predicted Unsteady or Steady Flow 141

Chapter 1

Introduction

1.1 Background

The term end-stage-renal disease (ESRD) refers to the permanent reduction or loss of renal function, when kidneys can no longer clear the blood of daily metabolic waste products. Patients affected by ESRD need a renal transplant or renal replacement therapy (RRT) to remain alive.

Arterio-venous fistulae (AVF) are connections surgically formed between an artery and a vein, commonly in the wrist or upper arm of patients affected by ESRD, who use haemodialysis as RRT. Because of their reliability in terms of lower risk of infections, thrombosis, and greater patency, AVF are the preferred form of vascular access for haemodialysis. Nonetheless, intimal hyperplasia (IH), an inflammatory disease which causes the AVF to block and fail, affects up to 60% of fistulae in the first three months since their creation, reducing patient's quality of life, and leading to significant additional costs for healthcare systems. One of the main hypotheses is that blood flow patterns and oxygen transport within AVF play an important role in determining whether AVF block and fail. So far, however, there has been little discussion about which is the predominant

effect or if there is one.

Understanding AVF flow characteristics can be crucial to elucidate the IH initiation process. This research focuses on investigating the mechanics of flow unsteadiness via computational modeling. The unsteady nature of the flow, the complexity of the vascular geometries and the difficulties in obtaining clear clinical data are some of the major challenges of this project. Patient variability of the AVF geometry may play a vital role in AVF failure or success. Therefore it was decided to investigate the flow mechanics of AVF in both idealised and patient specific computational models. Idealised models can be manipulated and modified to help understanding the contribution of geometric features to flow stability/unsteadiness, while patient-specific models can be studied to have a better understanding of the multi-parametric nature of the flow. The project started with looking at the effect of one single parameter, the arterial curvature in native arteries. It was then expanded with an idealised, multi-parametric model interested in suppressing flow unsteadiness through numerical optimization. Finally, it continued investigating the possible correlation between geometric parameters of realistic AVF reconstructed form MRI scans, flow unsteadiness, and AVF failure.

1.2 Thesis Overview

The aim of this thesis is to explore the flow mechanics in AVF, focusing on highly unsteady flow patterns. The thesis is divided in 7 main chapters:

- Chapter 1, Introduction.
- Chapter 2, Literature Review. The purpose of this chapter is to give a wider introduction to the problem, explaining thoroughly the concepts of AVF maturation and failure. In addition, a critical literature review on the state of the art on computational models of AVF and grafts and on the analysis of blood flow unsteadiness is provided.

- Chapter 3, The Effect of Arterial Curvature on Blood Flow in Arterio-Venous Fistulae. Realistic Geometries and Pulsatile Flow. In this chapter, which represents an extension of the work published in [1], a first attempt to study blood flow in a computational model of a semi-realistic AVF is presented. The arterial configuration of healthy patients was reconstructed to perform simulations on semi-idealised AVF. Grid independence is investigated together with the boundary conditions needed to impose a pulsatile inflow at the inlet.

- Chapter 4, Optimisation of Arterio-Venous Fistulae for Suppressing Unsteady Flow. A Kriging-based optimisation methodology is presented, in which computational simulations are performed to suppress unsteadiness inside the vascular configuration. The resulting optimised geometry is then tested with an accurate pulsatile simulation to verify the efficacy of the optimisation method.

- Chapter 5, A Device for Shaping Arterio-Venous Fistulae Connections. A preliminary version of a device for maintaining AVF in the shape proposed in Chapter 4 is illustrated. Data from a preliminary animal study are also reported as a proof of concept.

- Chapter 6, Realistic Geometries and Flow Unsteadiness. Patient specific simulations on 60 reconstructed AVF are analysed under steady boundary conditions. The main purpose of the chapter is to analyse the relationship between geometry induced flow unsteadiness and vascular parameters (such as vascular curvature, vascular non-planarity and anastomotic angle). A first study on the correlation between flow unsteadiness and AVF failure is also performed.

- Chapter 7, Conclusions. A critical summary of the work and future applications.

- Appendix: some of the numerical methods adopted in this work are reported and commented upon.

1.3 Resulting Publications

Part of the work reported here has been presented in the following journal papers, patent application, oral and poster presentations.

Journal Papers

- L. Grechy, F. Iori, R. W. Corbett, W. Gedroyc, N. D. Duncan, C. G. Caro, P. E. Vincent, The Effect of Arterial Curvature on Blood Flow in Arterio-Venous Fistulae: Realistic Geometries and Pulsatile Flow, Cardiovascular Engineering and Technology, Under Review.

- L. Grechy, F. Iori, R. W. Corbett, S. Shurey, W. Gedroyc, N. D. Duncan, C. G. Caro, P. E. Vincent, Suppressing Unsteady Flow in Arterio-Venous Fistulae, Physics of Fluids, Under Review.

- R. W. Corbett, L. Grechy, F. Iori, J. Crane, P. E. Herbert, P. Di Cocco, W. Gedroyc, P. E. Vincent, C. G. Caro, N. D. Duncan, Significant Heterogeneity Exists in the Non-Planarity and Arterial Curvature of Arterio-Venous Fistulae In Vivo, Kidney International, Under Review.

Patent Application

- L. Grechy, P. E. Vincent, R. W. Corbett, A Device for Maintaining Vascular Connections, Patent Application Number 1603501.6.

Oral Presentations

- ECCOMAS 2016, 5-10 June 2016, Crete Island, Greece. Oral Presentation. Investigating Flow Unsteadiness in Realistic and Optimised Arterio-Venous Fistulae.

- IMA 2014, Conference on Mathematical Modelling of Fluid Systems, 10-12 September 2014, Bristol, UK. Oral Presentation. Blood Flow and Oxygen Transport in Arterio-Venous Fistulae: Studying the Effect of Vascular Curvature.

Poster Presentations

- BMES 2014 Annual Meeting, 22-25 October 2014, San Antonio, Texas, USA. Poster Presentation: The Effect of Vascular Curvature on Blood Flow and Oxygen Transport in Arterio-Venous Fistulae.

Chapter 2

Literature Review

2.1 Arterio-Venous Fistulae

2.1.1 End Stage Renal Disease Treatment

Patients with End Stage Renal Disease (ESRD) need to have their blood cleared of metabolic waste periodically through renal replacement therapy (RRT).

In Grassman *et al.* [2], the authors estimated that, in 2004, more than 1,300,000 people needed RRT worldwide, with a prevalence value of 215 per million population (p.m.p). Among these, almost 250,000 patients were in the European Union (550 p.m.p.).

There are two main forms of RRT: haemodialysis (HD), and peritoneal dialysis (PD) [3]. HD is the most common: in 2004 more than 89% of the worldwide ESRD population was treated with HD, and in Europe alone the figure was, and still is, more than 90% [4, 5, 2].

HD, or haemofiltration, consists in withdrawing blood from a patient's vascular access, into the dialyzer. The dialyzer has an exchanger chamber with a semi-permeable membrane. The membrane separates blood from dialysate (water plus added solutes), which flows in the opposite direction to the blood, and the con-

centration gradient between the two liquids allows the waste products to pass from the blood to the dialysate. The clean blood is then returned in the patient's vascular access [6, 3].

2.1.2 Vascular Access for Haemodialysis

A good vascular access for HD should provide high flow rate to the dialyzer, should be reliable, durable, easy to use, and should minimize the risk of infection for patients [7].

Three main forms of vascular access are adopted by clinicians:

- Arterio-Venous Fistula (AVF): connection between an artery and a vein surgically formed either in the upper or lower arm of patients.

  AVF were introduced for the first time in 1966 [8, 9], and today they are considered the most reliable form of vascular access for HD [7, 10]. When AVFs are formed in the upper arm, they usually involve the brachial artery and the cephalic vein (brachio-cephalic fistula, or BCF, see Fig. 2.1) or the brachial artery and the basilic vein, if the cephalic vein is not available (brachio-basilic fistula, or BBF). In this case, because of its depth, the basilic vein is usually transposed, and therefore, there is a smaller length of vein available for cannulation. In the lower arm, AVFs are usually created between the radial artery and the cephalic vein (radio-cephalic fistula, or RCF) [11].

  The connection between the artery and the vein can be formed via three different methods:

  – side-to-end anastomosis (Fig. 2.1). The vein is cut and directly connected to the side of the artery. Currently, this is the most common form of AVF [12].

- side-to-side anastomosis: the side of the artery is directly connected to the side of the vein. This was the first type of autologous AVF formed in 1966 by Appell [8, 9], and described in the publication of Brescia, Cimino Appell and Hurwich [8]. It is also called the Brescia-Cimino fistula.
- end-to-end anastomosis: the terminal parts both of the vein and of the artery are cut and connected together. It should be avoided when there is a mismatch in vessels diameter [12].

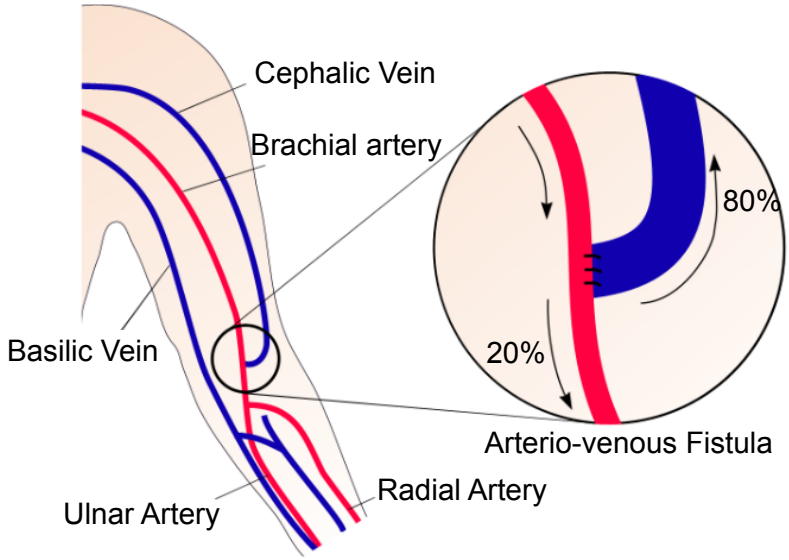


Figure 2.1: A brachio-cephalic fistula in a side-to-end anastomosis. Courtesy of Dr. Richard Corbett.

- Arterio-Venous Graft (AVG): connection between an artery and the venous system through an artificial prosthetic segment [11]. The synthetic materials used for AVGs can vary, but the most common is polytetrafluro-ethylene (PTFE). AVGs can be connected with a great variety of configurations.

  In 2002, in the US, the National Kidney Foundation published the Dialysis Outcome Quality Initiative (KDOQI) guidelines [7], promoting a greater use of AVFs over AVGs, because of their reliability, and suggesting that

AVGs should only be placed when it is not possible to form an AVF. In 2007 similar guidelines were adopted in Europe with the publication of the European Best Practice Guidelines for HD [10]. However, the question seems to be still open [13, 14, 12, 15, 16], and no randomized controlled trials have compared the two kinds of access [17].

- Central Venous Catheter (CVC). A synthetic device connected to the central veins. With the CVC there is no need to connect the arterial with the venous system, since high flow rate is directly provided by the central veins [7]. However, patients with CVCs are predisposed to higher risks of infection, and HD with a venous catheter is associated with higher morbidity and mortality [18]. The current guidelines [7, 10] highly discourage the use of CVC, and reserve it as a last resort for patients in need of HD.

2.2 Arterio-Venous Fistula Maturation

AVF maturation can be described as a series of physiological changes either in the artery or in the vein which leads to the AVF being suitable for dialysis. Detailed insight into this process can be found in the reviews of Riella *et al* [17] of 2013, in the review of Rothuizen *et al.* [19] of the same year, in the review of Dixon published in 2006 [20], or in the papers of Konner *et al.* and of Allon *et al* [12, 16] published in 2003 and 2002 respectively.

When a vein is connected to an artery, the peripheral resistance vessels in the distal part of the arm are bypassed, and a large pressure gradient affects the AVF. Therefore, after surgery there is an immediate increase of blood flow through the AVF. Changes in pressure and flow lead to vascular dilation and remodeling. There is an immediate dilation of the proximal artery and distal vein, which continues over several weeks after AVF creation. It has been estimated that within the first day after surgery, the average diameter of the artery increases by

24%, and the venous diameter by 56% [20]. In order to provide the right amount of blood flow for HD, the vein should totally increase to more then 120% of its initial diameter [20].

The exact mechanism through which vessels re-modelling occurs is still not fully understood, however factors such as Wall Shear Stress (WSS) and pressure, probably play an important role [20, 12].

2.3 Complications and Failure

A mature AVF can provide at least a flow rate of 300 ml/min when cannulated, for the total duration of dialysis [7, 20]. Unfortunately, although AVF are the preferred form of vascular access for HD, a high percentage of AVF fail to mature in the first few months [21, 17, 19, 22, 16].

According to the systematic review of Al-Jaishi *et al.* of 2014 [21], which used data from 46 articles published between January 2000 to June 2012, the rate of AVF primary failure, which was defined as immediate failure of AVF in the first 72 hours after creation; as AVF failure within the first 3 months after creation; as AVF failure in the first 6 months after creation, was estimated to be 23%. However, this figure varies significantly across the publications that were studies (between 5% [23] and 62% [24]), probably because of the heterogeneity of primary failure definition.

In [21], the primary patency rate was estimated to be 60% in the first year, and 51% at year 2, which means that within 2 years of creation, it is estimated that almost half of the AVFs needed an intervention to maintain or restore blood flow. There is high variability also in the primary patency rate data, which vary between 44% [15] and 77% [25] in the first year, and between 40% [15] and 63% [26] during year 2.

The estimated secondary patency rate (the count of all the patent AVF, including AVF that needed a surgical revision) was 71% at year 1 and 64% at year

2, with a variability between 43% [27] and 97% [28] at year 1, and 40% [29] and 94% [28] at year 2.

In conclusion, data from the literature seem to be highly variable, and there is a need for a more systematic way of classifying AVF failure. Nonetheless all the studies analysed suggest that after two years, on average, at least one third of created AVFs cannot be used anymore.

The major causes of AVF primary failure are [20, 19, 14, 12, 30]:

- The development of an inflammatory disease known as neo-intimal hyperplasia (IH), which may lead to vessel stenosis and thrombosis (see Fig. 2.2).
- Vascular wall calcification in uremic patients, resulting in impaired dilation of the AVF.
- Lesions derived from the surgical procedure, with subsequent thrombus formation.
- The presence of IH and/or other obstructive pathologies before AVF creation, that increase the vascular resistance of the anastomosis, and prevents normal AVF maturation.

Other complications that may result in AVF failure are the steal syndrome, aneurysm development and heart failure. The steal syndrome consists in inadequate blood flow to the distal arteries, with subsequent ischemia in the patient's hand [12].

2.3.1 Intimal Hyperplasia

Intimal hyperplasia (IH) is characterised by thickening of the intimal layer of the vessel, with consequent luminal narrowing and stenosis (see Fig. 2.2) [31, 19, 14]. Considerable progress has been made in the last decades, explaining IH formation from a histological point of view, however, the full mechanism is still unclear.

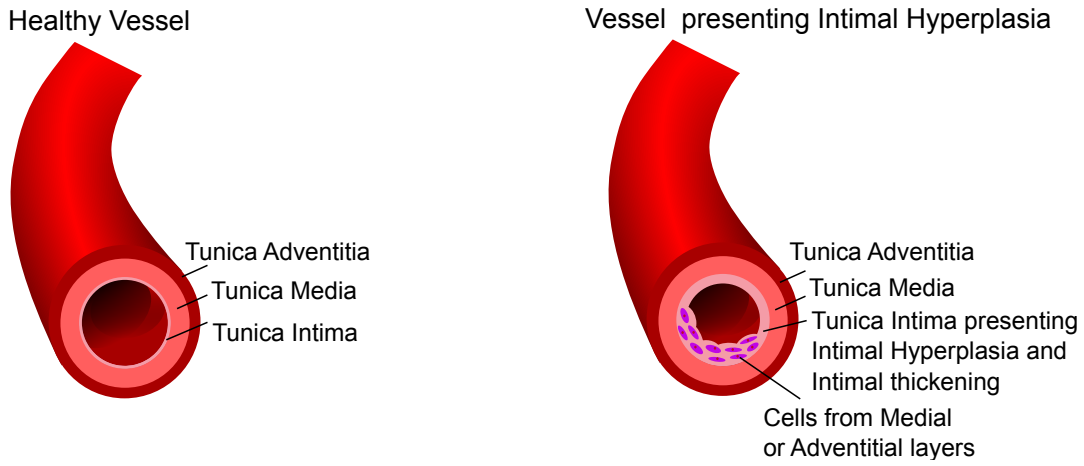


Figure 2.2: (a) Schematic healthy vesses. (b) Vessel presenting intimal hyperplasia.

In 1975 Spaet *et al.* [32] hypothesised for the first time that IH formation was caused by smooth muscle cell (SMC) migration from the medial layer to the tunica intima. This theory has become widely accepted [31]. However, according to the reviews of De Vries *et al.* of 2016 [31] and Roy-Chaudhury *et al.* of 2006 [14], intimal thickening may also be caused by fibroblasts migrating from the adventitial layer, through the medial layer, rather then SMC migration from the medial layer. The hypothesis is that the fibroblasts, once at the tunica intima, acquire the phenotype of myofibroblasts, and express smooth muscle markers [14].

Recent studies have also implicated the possible role of multi-potent vascular stem cells from bone marrow in the pathogenesis of IH [31, 14].

2.3.2 Wall Shear Stress and Intimal Hyperplasia

Since the publications of Caro *et al.* [33, 34] in 1969 and 1971, it has been widely recognised that endothelial exposure to low Time Averaged Wall Shear Stress (low TAWSS) plays an important role in vessel lesion initiation and atherosclerosis development [35]. Even though atherosclerosis and IH are different pathologies,

it is possible that they have a common initiation factor [31].

In the publication of Loth *et al.* in 2002 [36], a relation between low TAWSS and Intimal hyperplastic thickening was found for the juxta-anastomotic region of side-to-end PTFE grafts in an *in vivo* experiment. Other publications have also demonstrated that high spatial WSS gradient can be linked with IH development [37, 38].

Studies of Ku *et al.* in 1985 [39] and Himburg *et al.* in 2004 [40] indicated a possible correlation between exposure to low and oscillatory shear stress and atherosclerotic plaques formation, and introduced the Oscillatory Shear Index (OSI) [39] and the WSS Relative Residence Time (WSS-RRT) [40] as metrics to measure these low and oscillatory shear stress. Specifically, the OSI measures where the main direction of the flow is inverted during the pulse cycle, while the WSS-RRT show the areas having high OSI and low TAWSS.

The review by Chiu *et al.* of 2011 [41] summarised the state of the art of *in vivo* and *in vitro* experiments which correlated disturbed and/or stagnant flow with endothelial pathologies, focusing on how WSS patterns can regulate gene expression on endothelial cells. The authors concluded that there is a need to improve the current surgical procedures with the purpose of manipulating geometries to have more favourable flow patterns [41]. Numerical studies may play an imporant role to achieve this. The systematic review of Peiffer *et al.* in 2013 [35] analysed *in silico* studies which correlated low-TAWSS and/or low instantaneous WSS and/or OSI and/or WSS-RRT with atherosclerotic lesions. The authors found that the current metrics may lead to conflicting results, with some studies finding positive correlation between the metrics and atherosclerotic plaques and some not.

In 2013 Peiffer *et al.* [42] introduced the trans-WSS, a novel metric to measure if there was multi-directional disturbed flow during the pulse period. The authors found a good correlation between atherosclerotic plaque formation and areas with

high trans-WSS [42, 43]. A more detailed description of OSI, WSS-RRT and trans-WSS will be given in Sec 2.4.2

Finally, recent studies have proposed the theory that extremely high values of WSS could be related to cellular damage, which can initiate aneurysms [44, 45], a relatively common problem in AVF [22, 12].

2.3.3 Blood Flow Unsteadiness and Intimal Hyperplasia

Several clinical studies associate the presence of of a high-frequency bruit or thrill with a healthy AVF [11, 7, 29]. However, these observations seem to be in contrast with several experimental findings.

Nathan and Imparato in 1977 [46], Fillinger *et al.* in 1990 [47], and Loth *et al.* in 2002 [36], all linked intimal lesions with areas presenting palpable thrill and bruits in vascular grafts in *in vivo* experiments. The measured frequencies were between 1000 to 2000 Hz in [46], between 1000 to 3000 Hz in [47], and up to 300 Hz in [36]. In [36] a numerical model of the graft was also studied, and the resulting WSS fluctuations had frequencies up to 715 Hz. The experiments in [36] also suggested that wall vibration was a first biomechanical stimulus for producing a cellular mediating factor promoting SMC activation. However, the region of interest was the same affected by flow separation, and hence with the greatest fluctuation of WSS values.

In vitro experiments have also linked cellular response with highly unsteady flows. In 1986 Davies *et al.* [48] studied endothelial cells exposed to turbulent flow. Their results suggested that these cells had an increased cellular turnover, compromising the integrity of the cellular layer, compared to endothelial cells exposed to laminar flow over a comparable range of shear stress. Their results also suggested that endothelial cells are more susceptible to flow unsteadiness rather than to shear stress magnitude. Another *in vitro* study of 2016 [49] showed that macrophages responded with higher proliferation to low-intensity vibrations

up to 100 Hz. Even though the publication suggests that this can be a beneficial effect for the healing of various tissues, previous studies [31, 14, 50, 51] have linked IH with initial macrophage proliferation.

In conclusion, it seems that there are contradictory findings between clinical studies, for which the presence of bruits and thrills is considered beneficial [11, 7, 29], and experimental studies that link turbulent and unsteady flows to IH formation [46, 47, 36, 48].

A possible explanation of why AVF which do not present thrills and bruits during the first days are more likely to fail in clinical studies [11, 7, 29] is that these are AVF having low blood flow since surgery, either because of lesions derived directly from the surgical procedure [14, 12] or from the presence of other pathologies [20, 19, 14, 12, 30] that increase the vascular resistance of the anastomosis and/or result in impaired dilation of the AVF. The hypothesis proposed in this thesis is that there are also non-bruit, high-flow AVF, with a possible more favorable outcome.

2.3.4 Hypoxia and Intimal Hyperplasia

In 1944, Heuper [52] hypothesed for the first time a link between hypoxia and atherosclerosis. Since then, several in vitro and in vivo studies have linked hypoxia and atherosclerosis [53, 54]. However, the possible link between IH and hypoxia has been investigated only for the last two decades. In 1993 and 1995 Barker *et al.* linked hypoxia with arterial intimal hyperplasia formation [55, 51] through experiments on pigs and rabbits in which the *vasa vasorum* (vessel that provides oxygen to the vessels layers) were removed. In 2000, an experiment by Lee *et al* [56] linked the possible role of hypoxia with intimal lesions in rabbit aortic grafts. In 2008, in the paper of Misra *at al.* [57], higher levels of a hypoxia marker were found in patients with PTFE grafts, presenting vessel lesions, but not in AVF patients with the same kind of injury (however, only 17 patients

were analysed). Finally, in the 2013 work of Lata *et al.* [58] the exposure to an oxygenated environment was associated with the inhibition of IH after AVF creation in a group of rabbits.

2.4 Computational Fluid Dynamics

2.4.1 Computational Fluid Dynamics in Anastomotic Connections

The relationship between geometric features and blood flow has been widely investigated in the last decades, either via Computational Fluid Dynamics (CFD) studies of idealised geometries, or via reconstructed vascular connections with particular geometries (imposed by surgeons). More specifically, different studies have focused on AVF, AVG for vascular access, and bypass grafts (a surgical procedure which bypasses an occluded arterial segment either with an autologous vessels, or with artificial tissue).

Idealised models have been widely used to investigate the effect of geometrical features on blood flow in vascular connections. In the publication of Sherwin *et al* [59] and of Papaharilaou *et al.* [60], the influence of out-of plane geometry in idealised bypass grafts was modeled via CFD simulations. Their results were compared with phase-contrast MRI measurements. The main findings were that non-planar geometries seemed to profoundly affect the flow field, and therefore the possible graft outcome. They discovered also that imposing pulsatile boundary conditions was linked with a greater separation zone and unsteady flow in the grafts, compared to the steady models, but that the general flow features seemed similar. Coppola and Caro [61, 62] studied the blood flow and oxygen mass transfer in a helical vessel, showing that the swirling introduced by the helical shape can lead to more favourable outcomes in stented arteries [62]. In 2012 and 2013 Remuzzi and Ene-Iordache [63, 64] simulated pulsatile blood flow in idealised

end-to-end and side-to-end AVF configurations with various anastomotic angles. According to their results, an AVF formed by connecting a planar straight vein to a planar straight artery with an angle of 30 degrees is optimal because it should reduce unsteady flow and stagnation areas. The publication is of great interest because it represents the first attempt to evaluate the effect of the anastomosis angle in planar AVF. However, [63, 64] did not present a grid independence study, and both the temporal and spatial resolution employed in [63, 64] appear to be somewhat less than that required for accurate resolution of unsteady flow features. Moreover, the idealised model in [63, 64] analysed only planar configurations of AVF obtained connecting two straight tubes, not taking into account that arteries and veins exhibit variable curvature and torsion. In Iori, Grechy *et. al* [1] the effect of arterial curvature was investigated in idealised planar geometries with steady boundary conditions. The results showed that connecting the vein either on the outer or inner part of an arterial bend can dramatically change the flow and oxygen transport in the resulting AVF. Specifically, if one subscribes to the hypothesis that unsteady flow causes IH within AVF, then results suggested that AVF should be formed connecting the vein to the outer-curvature of a curved artery. On the other hand, if one subscribes to the hypothesis that low wall shear stress and/or low lumen-to-wall oxygen flux (LWNOF) cause IH within AVF, then results suggested that in order to avoid IH, AVF should be formed via a vein graft onto a straight artery, or the inner-curvature of a curved artery. This publication represented, to our knowledge, the first attempt to study the effect of in-plane arterial curvature using accurate flow simulations in AVF. However, it has several limitations, e.g. the inflow studied was steady, the vein was treated as a straight pipe, and all the geometries were planar.

The effect of geometric features on blood flow was also studied in *in vivo* models. The publications of Krishnamoorthy *et al.* [65] in 2008 and Rajabi-Jagahrgh *et al.* [66] in 2013 studied *in vivo* data from pigs with numerical simulations,

to analyse the relationship between AVF maturation and vein curvature. Their findings showed that either the lowest or the highest WSS values are inside the straight vein, which presented eccentric intimal-media thickening [65], and therefore the curved configuration was associated with a more favourable remodeling for AVF maturation [66].

All the aforementioned studies attempted to understand how geometric features can affect the flow. Other numerical studies focused instead in analysing the unsteady nature of the flow in both AVF and AVG. In 2002 the paper of Loth *et al.* [36] studied blood flow simualtions in an idealised graft, and transitional flow patterns were observed. Even though the flow analysis in this publication is purely qualitative, this paper is of great interest since it shows that with well-resolved CFD simulations it is possible to capture unsteady coherent structures in AVGs, and links them with the intimal thickening observed in the experiments. In 2015 Bozzetto *et al.* published a study of pulsatile flow in 4 patient-specific AVF [67] (2 BCF and 2 RCF) 6 weeks after creation. The authors found high frequency unsteady flow in the vein and disturbed flow in the proximal part of the distal artery. Their results were in line with the idealised study of Iori, Grechy *et. al* [1], since all the 4 geometries seemed to have either quasi-straight arteries, or an inner configuration. Botti *et al.* [68] published a study in 2013 about the Reynolds number effect in a patient-specific simulations under pulsatile and steady boundary conditions, with the main purpose of estimating the AVF resistance and validating the model with an experimental setup. Similarly, Browne *et al.* [69, 70] matched the pressure drop measured in patient-specific AVFs with a numerical idealised model and in *in vitro* experiments. Both the analyses were interesting because they concluded that the characteristic pressure drop measured in AVF is due to high-frequency flow instability in the vein.

Another fundamental point that needs to be investigated to have a better understanding of AVF maturation/failure is how the flow inside AVF in the first

days after surgery can affect the vascular remodeling. During the last years few publications have attempted to create mathematical models for plaque formation and endothelial remodeling [71, 72]. However these models have not been tried on realistic geometries yet. Gambaruto *et al.* [73], Lee *et al.* [74], and Sigovan *et al.* [75] tried instead to understand the vascular remodeling through CFD simulations of blood flow inside different vascular connections at different times. In particular [75] used computational simulations and MRI scan data to investigate how AVFs from three different patients evolved over a period of ten months. Their objective was to identify haemodynamic factors that contribute to AVF failure. The authors found that regions of the vein subjected to flow instability or recirculation were more prone to remodeling. However, all the reported studies had a small number of patients analysed, which makes the interpretation of results difficult.

Finally, McGah *et al.* [76, 77] simulated blood flow in four mature AVF, with a compliant wall model [77]. They hypothesised that the remodeling process in mature AVF, after 2 year of creation, do not completely restore the initial elevated values of TAWSS. The results in [77] suggest that modeling the distensibility of the arterial and venous walls may change the absolute value of TAWSS, but not the flow patterns. These results were in line with previous studies on the blood flow in the aorta [78].

The present work tries to address some of the problems here underlined. In chapter 3, the pulsatile effect on AVF blood flow on non-planar realistic arteries is analysed, focusing on the presence of high-frequency flow instabilities. Chapter 4 focuses on reducing high-frequency unsteady flow in idealised AVF, via an optimisation framework, and a novel vascular device is introduced in chapter 5, together with results from a first proof-of-concept experiment in a porcine model. Finally, a preliminary study on 60 patient-specific AVF at day 0 after surgery is presented in chapter 6, which investigates the link between blood flow

unsteadiness, geometrical features at day 0 and AVF maturation, and analyses also the remodeling of geometries from 20 between 1 or 2 weeks after surgery.

2.4.2 Flow Unsteadiness Measurements through Computational Fluid Dynamics

As introduced in Sec. 2.3.2, OSI, WSS-RRT and trans-WSS are all metrics that were introduced to measure disturbed flow in vascular sections [39, 40, 42]. More specifically OSI is defined as [39]:

$$\mathrm{OSI} = \frac{1}{2}\left(1 - \frac{\left|\int_T \boldsymbol{\tau}\mathrm{d}t\right|}{\int_T |\boldsymbol{\tau}|\,\mathrm{d}t}\right), \tag{2.1}$$

WSS-RRT is defined as [40]:

$$\text{WSS-RRT} \sim \frac{1}{\int_T |\boldsymbol{\tau}|\,\mathrm{d}t\ \ (1 - 2\mathrm{OSI})}, \tag{2.2}$$

and trans-WSS is defined as [42]:

$$\text{trans-}WSS = \frac{1}{T}\int_T \left|\boldsymbol{\tau} \cdot \left(\mathbf{n} \times \frac{\int_T \boldsymbol{\tau}\mathrm{d}t}{\left|\int_T \boldsymbol{\tau}\mathrm{d}t\right|}\right)\right| \mathrm{d}t, \tag{2.3}$$

where $\boldsymbol{\tau}$ is the space-time WSS vector field, T the pulse period, $\mathbf{n}$ the normal versor to the wall surface, and the operator $|.|$ represents the vector magnitude. The OSI identifies the areas where the flow changes direction, and it will give similar answers both in the case of uniaxial flow with reverse flow during the pulse, and in the case of multi-directional disturbed flow [42]. Similarly, the WSS-RRT identifies wall areas subject to high OSI and low TA-WSS. Finally, trans-WSS was introduced to overcome the OSI limitation and find areas purely affected by multi-directional flow [42]. However, all these metrics, by definition, extract only

time-averaged information, and do not investigate the characteristic frequencies of the disturbed flow. This thesis will focus on the study and suppression of high-frequency unsteadiness in AVF, therefore different metrics will be needed to study the characteristic frequencies of the flow.

In 2006 Himburg *et al.* [79] introduced the map of the vascular dominant harmonic as a new possible metric for flow unsteadiness under pulsatile boundary conditions. This represents an interesting first attempt to study the frequencies to which the EC may be subjected, however, under pulsatile conditions the pulse waveform, which can be decomposed in high intensity harmonics between 0-30Hz [78, 62, 80], can be modulated by high-frequency waveforms that may locally affect the EC, and that would be ignored by the metric in [79].

Continuous Proper Orthogonal Decomposition (POD) was introduced in the field of hydrodynamics by Lumley *et al.* in 1967 [81] for the identification of coherent structures of the velocity field in turbulent flows. POD decomposes a scalar or a vector field into a set of optimal orthogonal basis functions in space with corresponding temporal modes. In 1987 Sirovich [82] introduced the snapshot-POD that allowed the application of POD to large datasets. In [1] the spectra of the first three POD temporal modes were analysed to extract the characteristic frequencies of WSS in idealised AVF under steady boundary conditions. Previous to [1], in 2009, Grinberg *et al.* used POD to analyse the velocity field in a stenosed carotid artery under pulsatile boundary conditions [83]. It was found the first temporal modes mainly contained information on the pulse waveform, while high-order temporal modes contained information on the transitional flow.

In 2010 Schmid [84] introduced the Dynamic Mode Decomposition (DMD). DMD decomposes a scalar or a vector field into spatial basis each of which is associated with a fixed oscillation frequency and intensity. DMD is generally computationally more expensive compared than snapshot-POD and does not generate a series of optimal orthogonal basis, however, it allows an immediate characterisa-

tion of the flow frequencies. DMD will be used in this thesis to analyse the blood flow in different models of AVF under pulsatile boundary conditions. A detailed description of the DMD implementation will be given in the Appendix A.

2.4.3 Oxygen Transport and Computational Fluid Dynamics

In 1997 Moore and Ethier [85] simulated oxygen transport in a 2D model of a stenotic artery. They modeled the vessel layers, and tested the effect of different simplifying assumptions i.e. they modeled oxygen as both being bound to haemoglobin, under different haemoglobin formulation, and as a free solute, with different values for oxygen diffusivity. They showed that the axial distribution of the Sherwood number (dimensionless wall normal oxygen gradient) had similar qualitative behaviors either considering oxygen being bound to haemoglobin or modeling the oxygen as a free solute. However, local values of the Sherwood number were at least 2.5 times higher when the haemoglobin effect was included.

Subsequently, Qiu and Tarbell [86] proposed a simplified model to study the mass transfer problem in blood vessels, modeling oxygen as a free solute, and published a computational study of oxygen transfer in a compliant curved coronary artery [87]. Their study showed that wall normal oxygen gradient is up to 25 times lower on the inner part of the curved artery than the outer, which is consistent with the higher rate of atherosclerotic plaques in curved coronaries. Their simplified model of oxygen transport has been widely used since then; it was applied for studying oxygen transport in bypass grafts [88], models of stenotic arteries [89], in compliant and rigid carotid bifurcations [90], and a helical stent [61, 62]. In 2010 Tada [91] computed the mass transfer in a carotid bifurcation, coupling the CFD solver with a diffusion/consumption oxygen model inside the wall. Their results slightly differed from previous experiments, suggesting the need for a model of the wall oxygen transport which overcomes some of the cur-

rent approximations. During the same year, Liu *et al.* [92] modeled oxygen in a realistic aorta with both oxygen bound to haemoglobin, and oxygen considered a free solute. Their results showed that both modeling approaches lead to similar outcomes, but with a scale factor of two between free oxygen and haemoglobin model. The simplified model of Tarbell [86] was adopted in this project to compute the wall oxygen transport within the AVF models of chapter 3.

Chapter 3

The Effect of Arterial Curvature on Blood Flow in Arterio-Venous Fistulae: Realistic Geometries and Pulsatile Flow

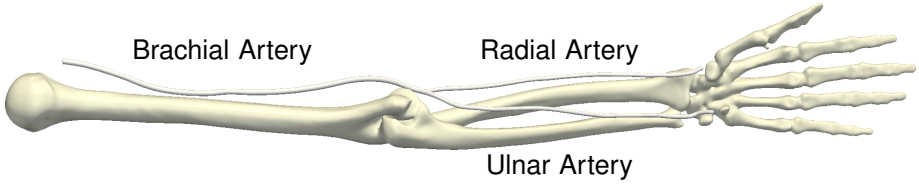
3.1 Introduction

In [1], it was predicted that forming an AVF by connecting a vein onto the outer curvature of a planar arterial bend would suppress potentially pathological high-frequency flow unsteadiness. However, it was also predicted that forming an AVF by connecting a vein onto the inner curvature of a planar arterial bend would suppress potentially pathological low WSS and low Lumen-to-Wall Oxygen Flux (LWNOF). The present chapter aims to extend this work taking into account the pulsatile nature of the flow in more realistic non-planar AVF configurations.

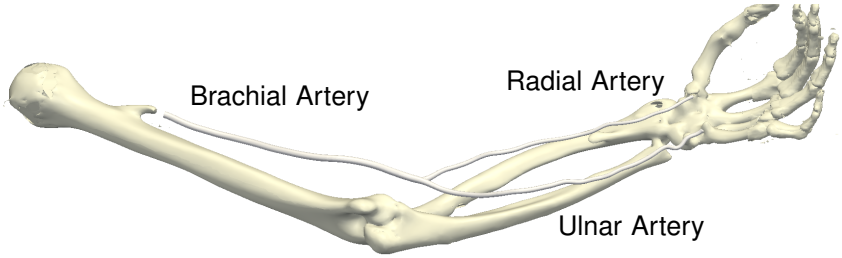
3.2 Methods

3.2.1 Geometries

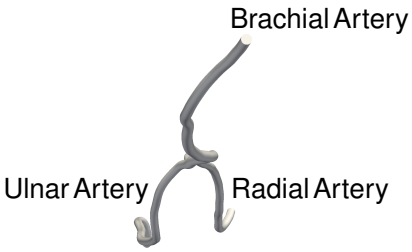
3.2.1.1 Native Vessels



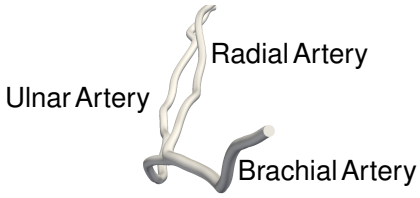
(a) P1



(b) P2



(c) P1



(d) P2

Figure 3.1: Frontal (a) and transversal (c) views of reconstructed native arterial geometries for P1 and frontal (b) and transversal (d) views for P2. Reconstructions of bones in the arm and hand are included as a reference in (a) and (b).

Native arterial geometries from two 'patients', henceforth referred to as P1 and P2, were reconstructed using anonymised CT scans of two adult subjects who

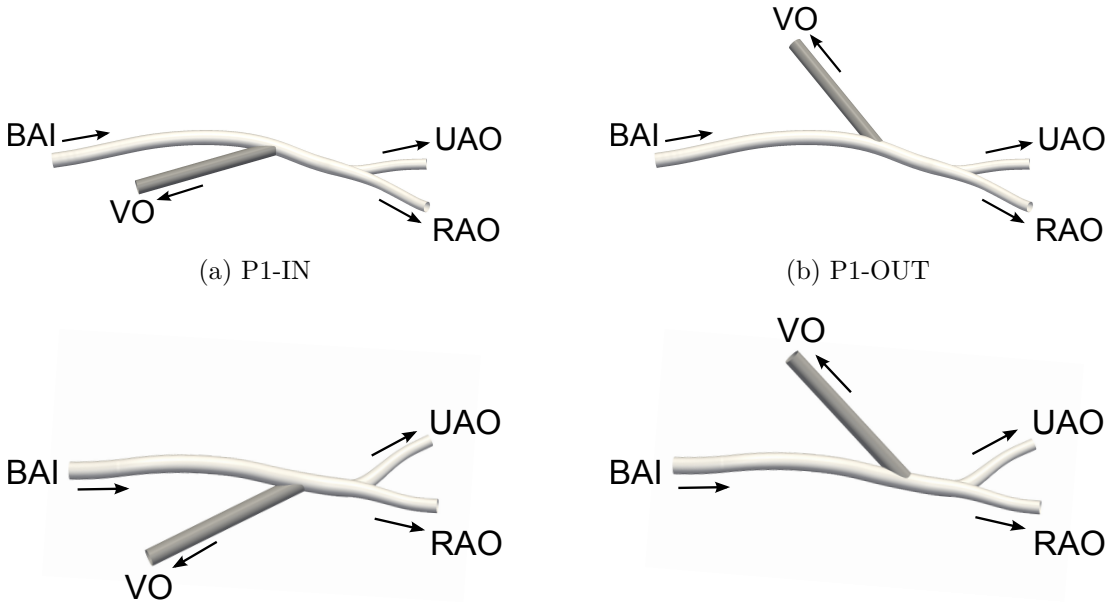
had undergone clinically-indicated upper-body CT angiography in the setting of major trauma and were found to have normal vasculature. The data collection had local research governance approval.

The geometries reconstruction and manipulation was performed before the beginning of the PhD, for an UROP project [93]. ITK Snap 2.4.0 [94] was used to segment the CT datasets. Specifically, a semi-automatic approach was used for reconstructing the brachial artery and the proximal sections of the radial and ulnar arteries, and manual segmentation for reconstructing the distal sections of the radial and ulnar arteries.

Vessel surfaces were then smoothed in VMTK [95], from which vessel centrelines and their maximum inscribed sphere radii MISR were extracted. Variations of MISR were calculated and averaged in five equisized sections of centreline.

Finally, PTC-Creo Parametric was used to sweep circular sections along each centreline to form the final geometries, where the circle radius was varied smoothly between the averaged maximum inscribed sphere radii in each section of the centreline. Images of the resulting arterial geometries for P1 and P2 are shown in Fig. 3.1 and Fig. 3.1. Reconstructions of bones in the arm and hand are included for reference in Fig. 3.1.

3.2.1.2 Forming an Arterio-Venous Fistulae



(a) P1-IN (b) P1-OUT

(c) P2-IN (d) P2-OUT

Figure 3.2: AVF configurations formed by connecting a straight vein, shaded in grey, onto arterial sections of P1 and P2. Specifically, P1-IN (a) is formed by connecting a vein onto the inner curvature of an arterial bend in P1, P1-OUT (b) is formed by connecting a vein onto the outer curvature of an arterial bend in P1, P2-IN (c) is formed by connecting a vein onto the inner curvature of an arterial bend in P2, and P2-OUT (d) is formed by connecting a vein onto the outer curvature of an arterial bend in P2. The Brachial Artery Inlet (BAI), Radial Artery Outlet (RAO), Ulnar Artery Outlet (UAO), and the Venous Outlet (VO) are labelled.

Straight veins were digitally anastomosed onto the inner/outer curvature of an arterial bend in P1/P2 using the CAD software PTC Creo Parametric to create brachiocephalic fistulae. Specifically, following Iori *et al.* [1], inner configurations were designed such that the anastomosis was located on the opposite side of the artery to the bulk of any skewed arterial flow (verified to be the case *a posteriori*), and outer configurations were designed such that the anastomosis was located on the same side of the artery as the bulk of any skewed arterial flow (also verified to be the case *a posteriori*). In all cases the vein had a diameter equal to that

of the BAI, and was connected at an angle of 35° to the local centre-line of the native artery, in line with Iori *et al.* [1]. Whilst in reality vein-to-artery diameter ratio and anastomosis angle will vary between patients, such a configuration is within the bounds described by various authors [69, 96, 63, 97], and is assumed here to be representative. In all cases the native arterial geometry was cropped approximately 6×10^{-2}m upstream and downstream of the anastomosis. The resulting brachiocephalic AVF configurations for P1 and P2 are shown in Fig. 3.2

3.2.2 Governing Equations

3.2.2.1 Blood Flow

For all configurations blood was treated as an incompressible Newtonian fluid. Specifically, blood flow was modelled using the time-dependent incompressible 3D Navier-Stokes equations for a fluid with constant viscosity, which can be written as

$$\boldsymbol{\nabla} \cdot \mathbf{u} = 0, \tag{3.1}$$

$$\rho \frac{\partial \mathbf{u}}{\partial t} + \rho \mathbf{u} \cdot \boldsymbol{\nabla} \mathbf{u} + \boldsymbol{\nabla} p = \mu \boldsymbol{\nabla}^2 \mathbf{u}, \tag{3.2}$$

where μ is the viscosity of human blood, ρ is the density of human blood, $\mathbf{u}$ is the three-dimensional blood velocity (vector) field, and p is the pressure. Values of $\mu = 3.5 \times 10^{-3}\text{Pa} \cdot \text{s}$ and $\rho = 1060\text{kg} \cdot \text{m}^{-3}$ [98] were employed.

The assumption of Newtonian rheology ignores the well known 'shear-thinning' property of blood, which begins to occur at shear rates below $50 - 100\text{s}^{-1}$ [99, 100, 101] and is particularly significant below shear rates of 10s^{-1} [100]. An *a posteriori* analysis of results from P1-OUT revealed at most 0.18% of the total blood volume was exposed to a shear rate below 10s^{-1} at a given time instant, and an analogous figure of 0.55% was obtained for P2-OUT. Hence the assump-

tion is considered reasonable. This assumption has been widely used in previous studies of blood flow in AVF and vascular grafts [1, 69, 77, 68, 75, 102, 50].

3.2.2.2 Oxygen Transport

Oxygen was treated as a passive scalar dissolved in blood plasma, adopting the model described in [86] and previously used in [1]. The time-dependent 3D advection-diffusion equation for a solute with constant diffusivity in an incompressible fluid is:

$$\frac{\partial c}{\partial t} = K\boldsymbol{\nabla}^2 c - \mathbf{u} \cdot \boldsymbol{\nabla} c, \tag{3.3}$$

where K is the diffusivity of oxygen in human plasma, $\mathbf{u}$ is the three-dimensional blood velocity (vector) field, and c is the oxygen concentration. A value of $K = 1.2 \times 10^{-9}\mathrm{m}^2 \cdot \mathrm{s}^{-1}$ [62] was used in this study.

Oxygen is transported in blood bound to haemoglobin, and modeling oxygen as a free solute ignores this bond. However, previous studies suggest that augmenting the oxygen transport patterns by a spatially constant factor of approximately two [92], gives results similar to the ones obtained modeling the effect of haemoglobin, and it can be accounted for *a posteriori* when the results are analysed (see section 3.3.2.1).

3.2.2.3 Non-Dimensional Quantities

Various salient non-dimensional quantities are associated with the physics modeled in this work. These include:

- The Reynods number, defined as

$$Re = \frac{\rho D \overline{u}}{\mu}, \tag{3.4}$$

  where D is the section diameter, and $\overline{u}$ the section average velocity magnitude. The Reynolds number measures the ratio between inertial forces and

viscous forces in the flow.

- The Womersley number

$$Wo = D\left(\frac{\omega\rho}{\mu}\right)^{\frac{1}{2}}, \tag{3.5}$$

where ω is the angular frequency of the pulse period. The Womersley number gives a measure of the ratio between the unsteady inertial forces and viscous forces.

- The Dean number

$$De = Re\sqrt{\kappa D/2}, \tag{3.6}$$

where κ is the local vascular curvature. The Dean number takes into account the contribution of the centripetal forces to the flow mechanics.

- The Schmidt number

$$Sc = \frac{\mu}{\rho K}. \tag{3.7}$$

It measures the ratio between momentum diffusivity and mass diffusivity.

- The Peclet Number

$$Pe = ReSc. \tag{3.8}$$

It measures the ratio between the advective transport rate and the diffusive transport rate.

3.2.3 Boundary Conditions

3.2.3.1 Blood Flow

A no-slip boundary condition was applied at the AVF wall. A space-time varying velocity boundary condition was imposed at the BAI of each AVF configuration. The inflow rate waveform, which had a period of 1s, was taken from Sigovan *et*

al. [75]. Specifically the first 15 Fourier modes were extracted, and the signal was scaled such that the peak Reynolds number at the BAI was 1300, in agreement with [75]. The resulting time-averaged Reynolds number at the BAI, Re_{BAI}, was $\sim$ 750, similar to the time-constant inflow Reynolds number used in [1]. The corresponding Womersley number at BAI was $Wo_{BAI} = 6.1$ for P1, and $Wo_{BAI} = 7.1$ for P2. All flow was prescribed normal to the BAI inflow plane, and following previous studies [77, 102, 83], a Womersley profile was imposed in space. The inflow rate waveforms at the BAI Q_{BAI} for P1 and P2 are shown in Fig. 3.4.

A RCR Windkessel model was applied at the RAO, UAO and VO. Specifically

$$P_{RAO} = Q_{RAO}(R_{1RAO} + R_{2RAO}) - R_{2RAO}C_{RAO}\frac{\mathrm{d}}{\mathrm{d}t}(P_{RAO} - R_{1RAO}Q_{RAO}), \quad (3.9)$$

$$P_{UAO} = Q_{UAO}(R_{1UAO} + R_{2UAO}) - R_{2UAO}C_{UAO}\frac{\mathrm{d}}{\mathrm{d}t}(P_{UAO} - R_{1UAO}Q_{UAO}), \quad (3.10)$$

$$P_{VO} = Q_{VO}(R_{1VO} + R_{2VO}) - R_{2VO}C_{VO}\frac{\mathrm{d}}{\mathrm{d}t}(P_{VO} - R_{1VO}Q_{VO}), \quad (3.11)$$

where P_{RAO}, P_{UAO} and P_{VO} are the spatially averaged pressure waveforms at the RAO, UAO, and VO respectively, Q_{RAO}, Q_{UAO} and Q_{VO} are the outflow rate waveforms at the RAO, UAO, and VO respectively, and R_{1RAO}, R_{2RAO}, C_{RAO}, R_{1UAO}, R_{2UAO}, C_{UAO}, R_{1VO}, R_{2VO}, C_{VO} are relevant Windkessel parameters.

Values for the Windkessel parameters were selected using an approach similar to Pant *et al.* [103]. Specifically, they were obtained for P1-IN and P2-IN

configurations using an iterative approach, that aimed to minimise

$$\Phi = \left(\frac{\max(P_{BAI}) - P_{RS}}{P_{RS}}\right)^2 + \left(\frac{\min(P_{BAI}) - P_{RD}}{P_{RD}}\right)^2 + \left(\frac{\int |Q_{VO} - Q_R| \, \mathrm{d}t}{\int |Q_R| \, \mathrm{d}t}\right)^2, \tag{3.12}$$

where P_{BAI} is the pressure waveform at the BAI, $P_{RS} = 130$mmHg and $P_{RD} = 80$mmHg are reference systolic and diastolic pressures, respectively, at the BAI taken from Sigovan *et al.* [75], Q_R is a reference outflow rate waveform at the VO taken from Sigovan *et al.* [75], and the integrals are taken to be over a single pulse cycle, when the solution has become period independent.

The iterative process itself employed a 0D lumped parameter model, detailed in Fig. 3.3, combined with a low-resolution time-dependent 3D model of flow in each configuration. The 0D model represented the low-resolution 3D model in terms of three inductors, with inductances L_{1A}, L_{2A}, and L_{1V} as per Fig. 3.3 as well as three quadratically non-linear resistors with resistances R_{1A}, R_{2A}, and R_{1V} as per Fig. 3.3. The 3D model solved the governing flow equations as per section 3.2.2.1 using StarCCM+ v9.06.9 as per section 3.2.4, but with $\sim 1/11$ of the spatial resolution and 1/5 of the temporal resolution. It was assumed that the UAO and RAO has the same peripheral behaviour *i.e.* $R_{1UAO} = R_{1RAO}$, $R_{2UAO} = R_{2RAO}$ and $C_{UAO} = C_{RAO}$. Hence, both outlets were merged in the $0D$ model as per Fig. 3.3, and were parameterised in terms of R_{1UAO}, R_{2UAO} and C_{UAO} alone.

To begin the iterative process, L_{1A}, L_{2A}, L_{1V}, R_{1A}, R_{2A}, and R_{1V} were estimated, and the 0D model was used to identify values of the Windkessel parameters that minimised Φ. These parameters were then used to define boundary conditions for the low-resolution $3D$ model, which was run until the solution became period independent, and from which improved estimates for L_{1A}, L_{2A}, L_{1V}, R_{1A}, R_{2A}, and R_{1V} were then extracted. These were fed back into the $0D$ model, and the process was repeated until the Windkessel parameters were seen to converge.

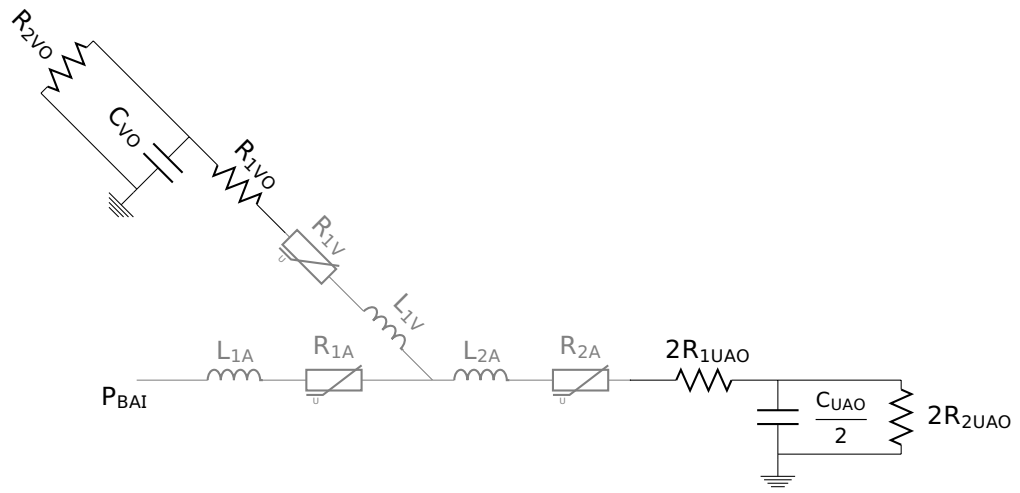


Figure 3.3: Schematic illustration of the 0D model used in the Windkessel parameter estimation process. Grey components were used to represent the low-resolution 3D model.

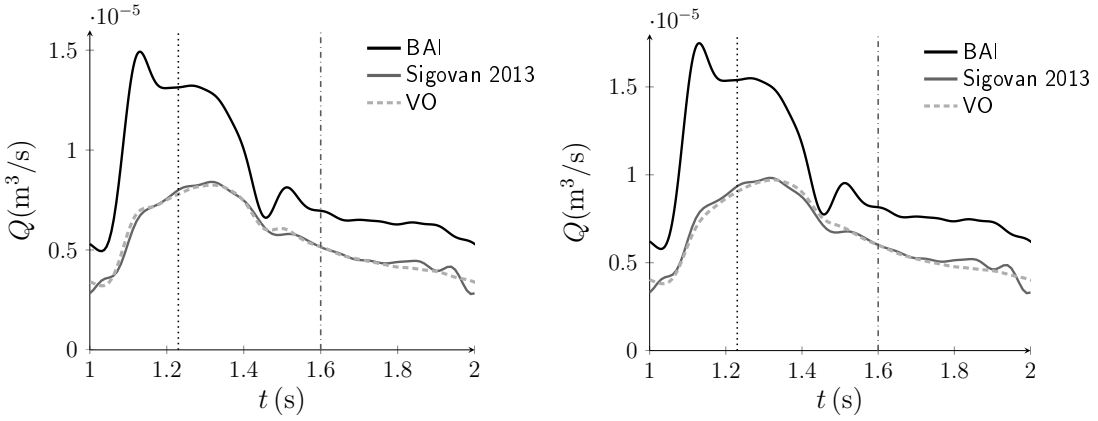
Values of the Windkessel parameters obtained for the P1-IN and P2-IN simulations are shown in Table 3.1. The parameters used for P1-IN and P2-IN simulations were also used for P1-OUT and P2-OUT simulations, respectively.

	P1-IN	P2-IN
R_{1RAO} $(\mathrm{mmHg\,ml^{-1}s})$	6.88	3.20
R_{2RAO} $(\mathrm{mmHg\,ml^{-1}s})$	59.80	53.20
C_{RAO} $(\mathrm{ml\,(mmHg)^{-1}})$	0.010	0.009
R_{1UAO} $(\mathrm{mmHg\,ml^{-1}s})$	6.88	3.20
R_{2UAO} $(\mathrm{mmHg\,ml^{-1}s})$	59.80	53.20
C_{UAO} $(\mathrm{ml\,(mmHg)^{-1}})$	0.010	0.009
R_{1VO} $(\mathrm{mmHg\,ml^{-1}s})$	7.00	7.00
R_{2VO} $(\mathrm{mmHg\,ml^{-1}s})$	10.30	7.50
C_{VO} $(\mathrm{ml\,(mmHg)^{-1}})$	10.50	5.25

Table 3.1: Windkessel parameters obtained for the P1-IN and P2-IN simulations. The parameters used for P1-IN and P2-IN simulations were also used for P1-OUT and P2-OUT simulations, respectively.

The resulting average flow splits between the VO and the distal arteries in a temporal window spanning the full pulse period (henceforth referred to as WT),

systole from 1.1s to 1.4s (henceforth referred to as WS), and part of diastole from 1.4s to 1.7s (henceforth referred to as WD), were ∼66 : 34, ∼60 : 40, and ∼78 : 22 respectively. The resulting venous outflow is shown in Fig. 3.4, compared with the reference outflow rate waveform at the VO taken from Sigovan *et al.* [75].



(a) P1 (b) P2

Figure 3.4: Q_{BAI} and resulting Q_{VO} for P1 (a) and P2 (b). Q_{VO} is compared the reference outflow rate waveform at the VO taken from Sigovan *et al.* [75]. The dotted and dash-dotted vertical lines indicate time points referenced from Fig. 3.12.

It can be noted that the arterial Dean number De defined as $De = Re_{BAI}\sqrt{\kappa_A D_A/2}$, where κ_A and D_A are the local arterial curvature and arterial diameter respectively at a given point in the artery, never exceeds 320 anywhere in the proximal arterial section of any configuration *i.e.* it is always well below the critical Dean number of ~ 900, at which multiple unsteady vortices develop in a planar curved tube [104].

3.2.3.2 Oxygen Transport

Following Iori *et al.* [1], a steady-state spatially-constant oxygen concentration of $c_{BAI} = 1.305 \times 10^{-1}\text{mol} \cdot \text{m}^{-3}$ was applied at the BAI (based on an oxygen partial pressure of 75 mmHg [53] and a Henry's law constant of $1.74 \times 10^{-3}\text{mol} \cdot \text{m}^{-3} \cdot \text{mmHg}^{-1}$ [105]). Zero boundary-normal oxygen concentration

gradients were applied at the VO, RAO, and UAO. Also, for all configurations a steady-state spatially-constant oxygen concentration of $c_W = 1.044 \times 10^{-1}\text{mol} \cdot \text{m}^{-3}$ was applied at the arterial and venous walls (based on an oxygen partial pressure of 60 mmHg [53] and a Henry's law constant of $1.74 \times 10^{-3}\text{mol} \cdot \text{m}^{-3} \cdot \text{mmHg}^{-1}$ [105]).

The imposition of a spatially-constant oxygen concentration at the proximal arterial inlet is based on the assumption that oxygen is 'well mixed' upstream of the domain. The imposition of a spatially-constant oxygen concentration at the arterial and venous walls is based on the assumption that the walls act as an oxygen sink, readily consuming oxygen [86].

The Schmidt number for these simulations was $Sc = 2700$, the corresponding Peclet at systole was $Pe = 3.510 \times 10^6$, with an average $Pe = 2.025 \times 10^6$

3.2.4 Computational Method

Polyhedral unstructured volume meshes, with prismatic boundary layer meshes adjacent to the arterial wall, were generated in Star-CCM+ v9.06.9 for each configuration. The meshes were refined near the anastomosis. Specifically, elements near the anastomosis had an average size of $\sim 6 \times 10^{-5}$m, expanding progressively to $\sim 1.5 \times 10^{-4}$m beyond a distance of $\sim$0.045m from the anastomosis. The prismatic boundary layer meshes were 25 elements thick, with the first element having a thickness of less than 3×10^{-6}m; in line with the mesh resolution employed in [62]. Each mesh had $\sim 11 \times 10^6$ elements in total. Results of a mesh independence study are presented in Sec. 3.2.4.1.

Solutions for the blood velocity field and the oxygen concentration were obtained using Star-CCM+ v9.06.9 via the following procedure:

- Each simulation was initialised with zero velocity, zero oxygen concentration, and a pressure of 78mmHg, and run with the coupled steady solver until every momentum and mass continuity residual fell below 10^{-10}.

- Each steady-state solution was then used as the initial condition for the coupled implicit unsteady solver, which advanced solutions 1s in time (1 pulse period). For all simulations a timestep of 1×10^{-4}s was used.
- Each simulation was then advanced a further 1s (1 pulse period) using the coupled implicit unsteady solver, during which time data were exported for analysis. Results of a period independence study are presented in 3.2.4.2. For all simulations a timestep of 1×10^{-4}s was used.

Each simulation was carried out on 64 cores of a Dell AMD Opteron 64-core server with 512 GB RAM, and required approximately 4 weeks to complete.

3.2.4.1 Mesh Independence

Polyhedral Unstructured Volume Mesh

Grid convergence of the polyhedral unstructured volume mesh was assessed by running simulations on seven successively finer discretisations of the P1-IN configuration using Star-CCM+ v9.06.9. All discretisations had a fixed prismatic boundary layer mesh that was 25 elements thick, with the first element having a thickness of $\sim 2.6 \times 10^{-6}$m; in line with the boundary layer mesh resolution employed in [1]. For each mesh, the element size near the anastomosis Δ, and the overall number of mesh elements N_e, are given in Table 3.2.

Each simulation had steady inflow boundary conditions. Specifically, the inflow Reynolds number at the BAI was fixed at $1,300$, the flow split between the VO and the distal arteries was $45:55$, and the flow split between the UAO and the RAO was $50:50$. These conditions correspond to peak inflow in the associated pulsatile simulation. The oxygen boundary conditions were the same as those used for the pulsatile simulation. Each simulation was initialised by converging to a steady-state solution such that all the residuals had an absolute value smaller than 1×10^{-9}. Each steady-state solution was then used as the initial condition for the coupled implicit unsteady solver, which advanced solutions 0.2s,

and then a further 0.07s over which data was extracted for analysis. All unsteady simulation used a time step of 2.2×10^{-4}s.

Time-averaged WSS magnitude $\overline{\tau}_t$ and time-averaged Lumen-to-Wall Normal Oxygen Flux (LWNOF) $\overline{q}_t$ were extracted from each simulation. Distributions of $\overline{\tau}_t$ and $\overline{q}_t$ are shown in Figs. 3.5 and 3.6 respectively. Space-time-averaged WSS magnitude $\overline{\tau}_{ts}$ and space-time-averaged LWNOF $\overline{q}_{ts}$ were also calculated for each simulation, and used to obtain percentage errors E_τ and E_q defined as

$$E_\tau = \frac{|\overline{\tau}_{6ts} - \overline{\tau}_{ts}|}{\overline{\tau}_{6ts}} \times 100, \tag{3.13}$$

and

$$E_q = \frac{|\overline{q}_{6ts} - \overline{q}_{tS}|}{\overline{q}_{6ts}} \times 100, \tag{3.14}$$

where $\overline{\tau}_{6ts}$ and $\overline{q}_{6ts}$ are values of $\overline{\tau}_{ts}$ and $\overline{q}_{ts}$ respectively from mesh M6 (the finest discretisation). Plots showing how E_τ and E_q vary with N_e are shown in Fig. 3.7.

	Δ (m)	$\mathrm{N_e}$
Mesh 0	3.00×10^{-4}	$728,037$
Mesh 1	1.50×10^{-4}	$1,534,415$
Mesh 2	1.20×10^{-4}	$2,579,029$
Mesh 3	9.60×10^{-5}	$4,107,567$
Mesh 4	7.70×10^{-5}	$6,719,031$
Mesh 5	6.16×10^{-5}	$11,751,352$
Mesh 6	5.00×10^{-5}	$19,988,816$

Table 3.2: Δ and N_e for each mesh.

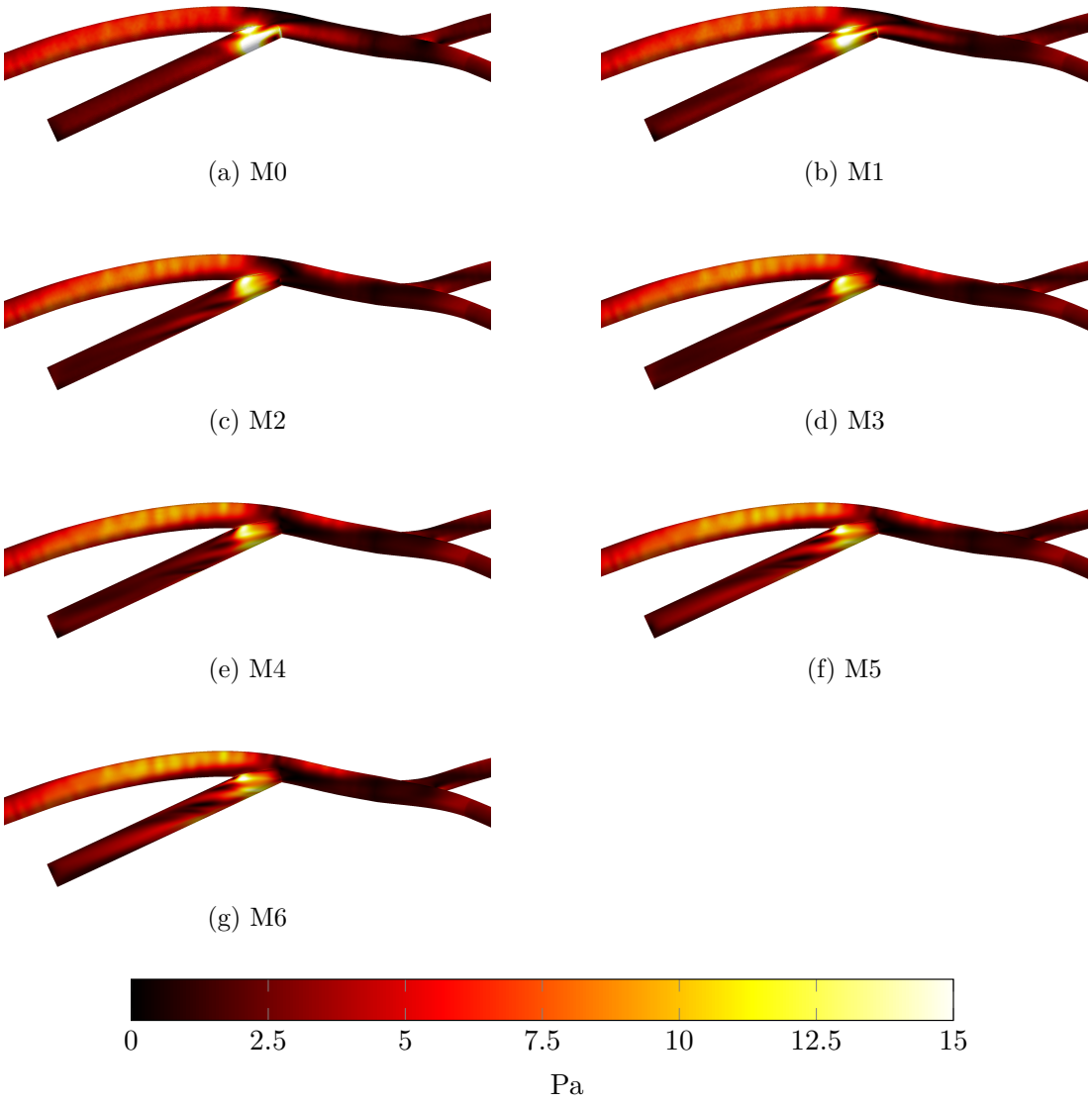


Figure 3.5: Distributions of $\overline{\tau}_t$ in P1-IN for meshes M0, M1, M2, M3, M4, M5, and M6.

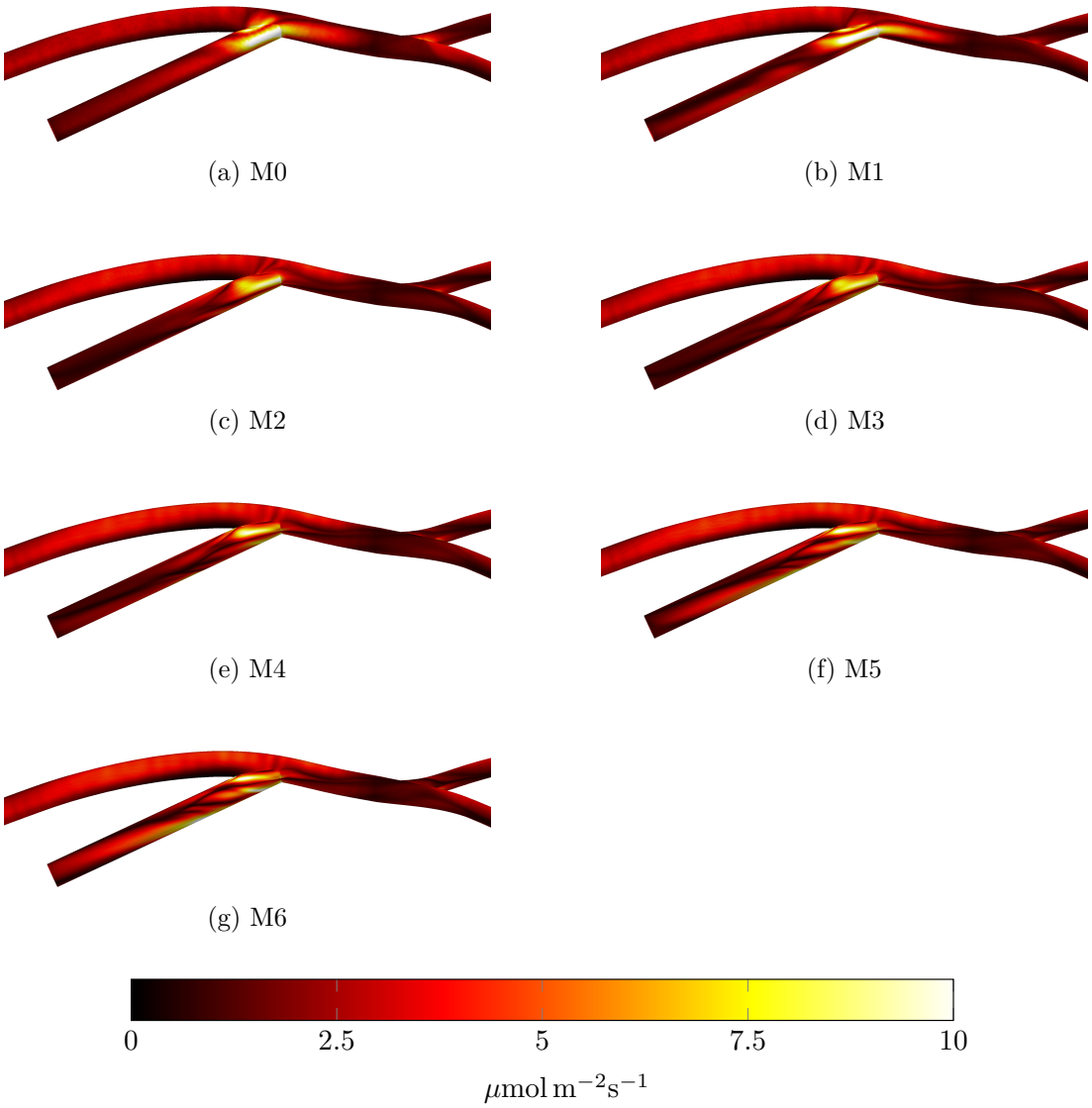


Figure 3.6: Distributions of $\overline{q}_t$ in P1-IN for meshes M0, M1, M2, M3, M4, M5, and M6.

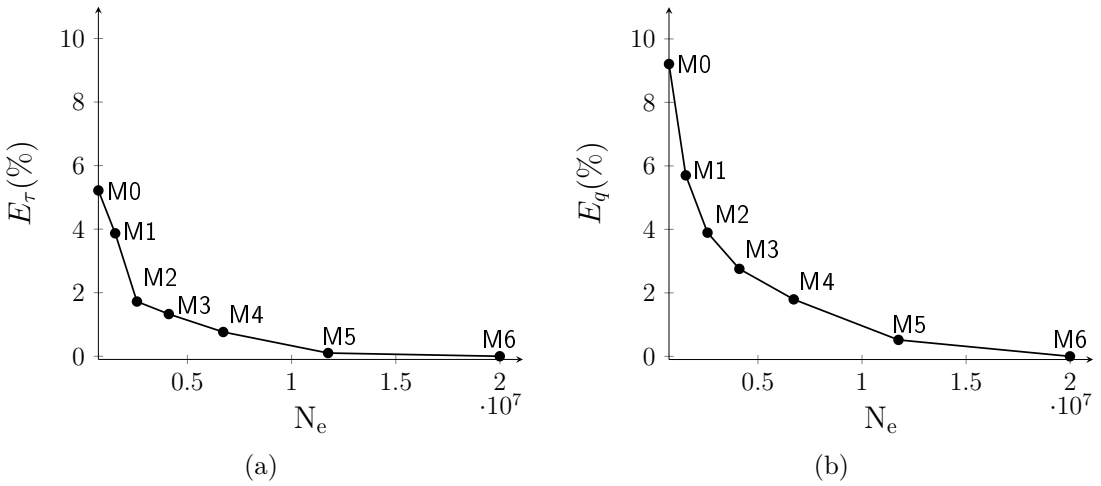


Figure 3.7: Plots of E_τ (a) and E_q (b) against N_e.

Prismatic Boundary Layer Mesh

Grid convergence of the prismatic boundary layer mesh was assessed by running simulations on versions of Mesh 5 with either increased or decreased boundary layer resolution. Specifically two meshes, henceforth referred to as Mesh 5+ and Mesh 5-, were made. Each mesh had the same overall boundary layer mesh thickness as Mesh 5, but a different number of boundary layer mesh elements N_l in the wall normal direction (see Table 3.3). Plots showing how E_τ and E_q vary with N_l are shown in Fig 3.8.

	N_l	N_e
Mesh 5-	15	9,456,231
Mesh 5	25	11,751,352
Mesh 5+	35	13,482,563

Table 3.3: N_l and N_e for each mesh.

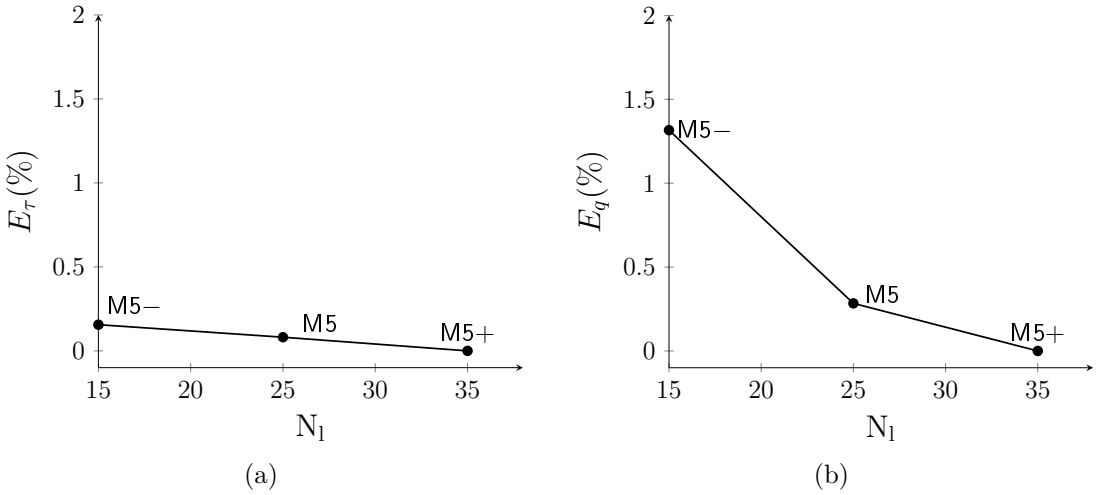


Figure 3.8: Plots of E_τ (a) and E_q (b) against N_l.

Based on the results presented, mesh M5 was used for the simulation in P1-IN, and meshes with similar resolutions were used for simulations in P1-OUT, P2-IN, and P2-OUT.

3.2.4.2 Period Independence

The P1-IN simulation was started from a steady-state solution as per section 3.2.4 and advanced 3s in time (3 pulse periods) using the coupled implicit unsteady solver and a timestep of 1×10^{-4}s. Period convergence was assessed by comparing solution data from $t \in [1, 2]$s, hence forth referred to as $T1$, with solution data from $t \in [2, 3]$s, hence forth referred to as $T2$.

Distributions of $\overline{\tau}_t$ over T1 and T2 are shown in Fig. 3.9. Visually the distributions appear very similar. Quantitatively, spatial averages of $\overline{\tau}_t$ over T1 and T2 were found to be within 0.08%. Distributions of $\overline{q}_t$ over T1 and T2 are shown in Fig. 3.9. Once again, visually the distributions appear very similar. Quantitatively, spatial averages of $\overline{q}_t$ over T1 and T2 were found to be within 0.03%.

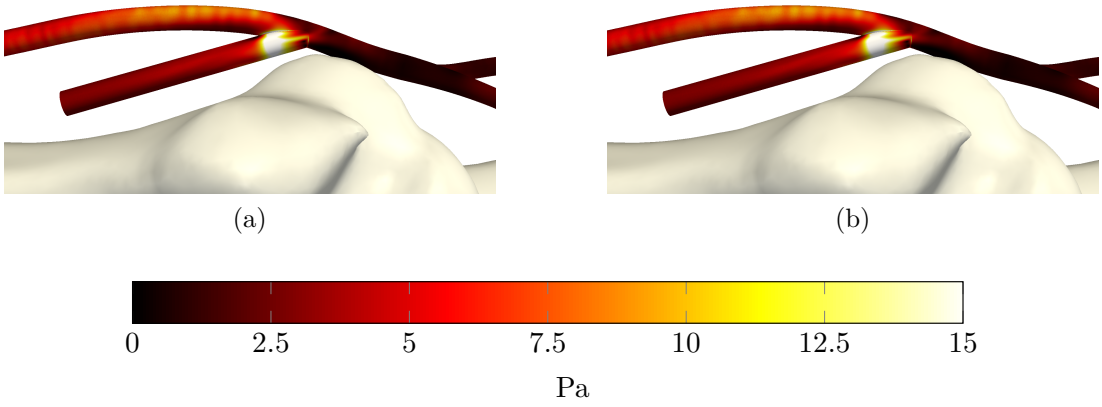


Figure 3.9: Distributions of $\overline{\tau}_t$ in P1-IN over T1 (a) and T2 (b).

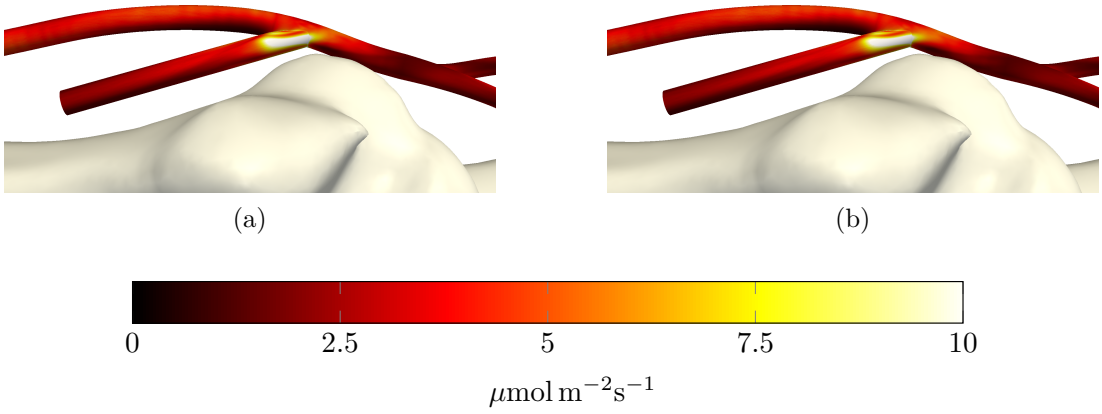


Figure 3.10: Distributions of $\overline{q}_t$ in P1-IN over T1 (a) and T2 (b).

Unsteady content was compared between T1 and T2 with extracting the Dynamic Mode Decomposition (DMD) [84] intensity of $\boldsymbol{\tau} - \overline{\boldsymbol{\tau}}_t$, where $\boldsymbol{\tau}$ space-time WSS vector field in in the whole vessel and $\overline{\boldsymbol{\tau}}_t$ is the temporal average of the space-time WSS vector field. Specifically, 1250 temporal snapshots with a uniform spacing of 0.0008s were used from each of T1 and T2. Plots of the DMD intensity γ were extracted from T1 and T2, are shown in 3.11. Visually the DMD

intensity appears very similar.

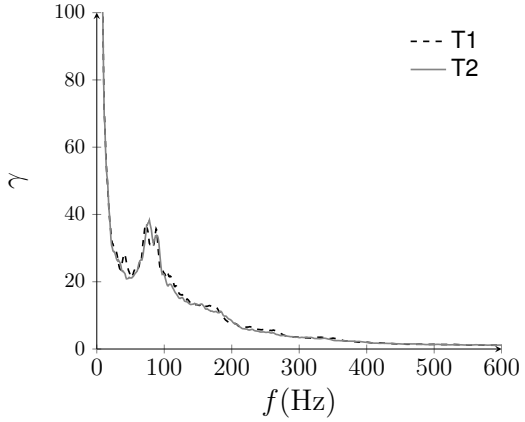


Figure 3.11: DMD intensity γ of $\boldsymbol{\tau} - \overline{\boldsymbol{\tau}}_t$ for T1 and T2.

Based on the results presented above, data from $t \in [1, 2]$s were exported for analysis from simulations in P1-IN, P1-OUT, P2-IN, and P2-OUT.

3.3 Results

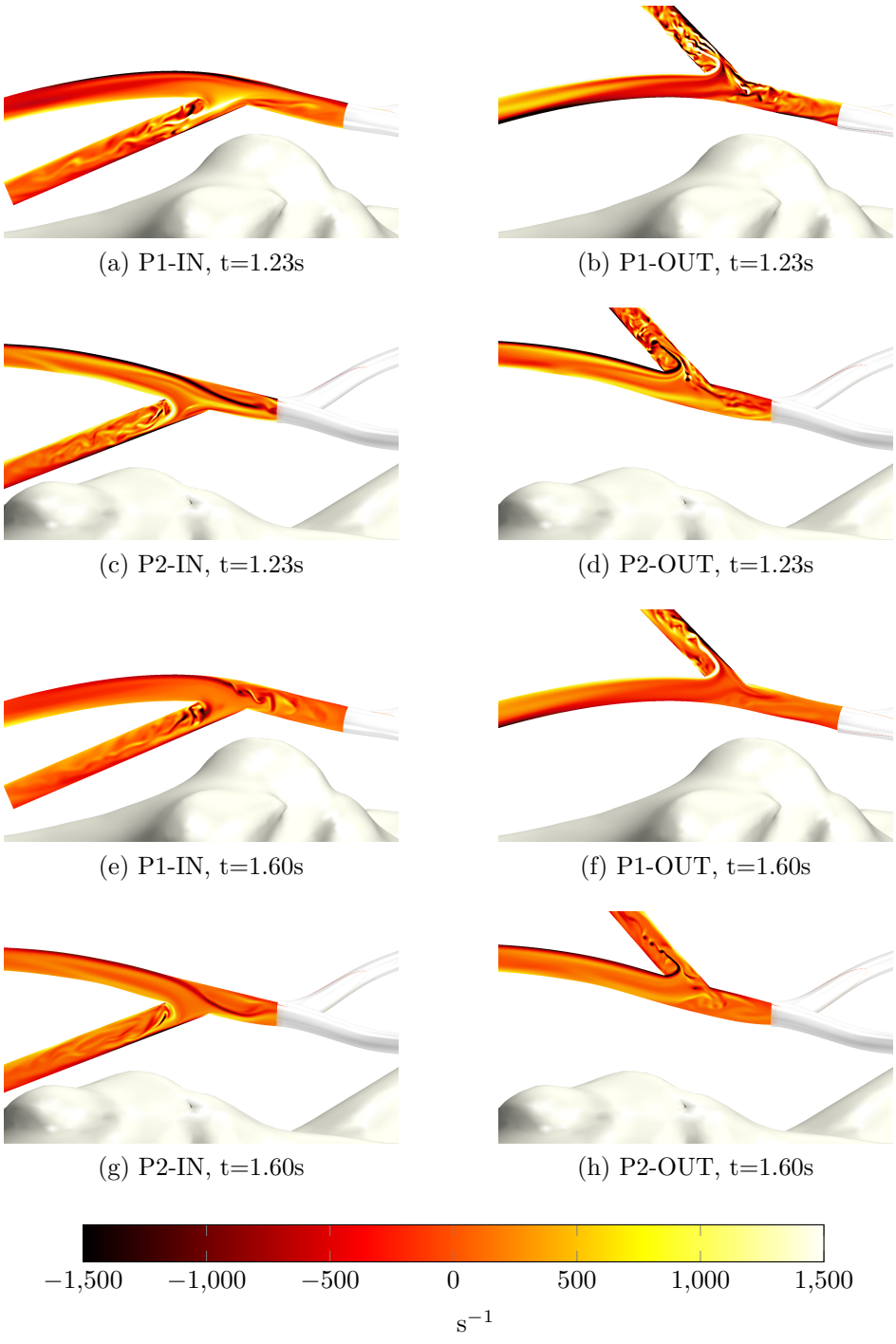
3.3.1 Unsteady Analysis

3.3.1.1 Qualitative Insight

Fig. 3.12 show shapshots of plane-normal vorticity on planes within each AVF configuration during systole and diastole.

Unsteady flow can be observed in the venous section of all configurations at almost all points in the pulse cycle. This result is inline with the idealised model of Iori [1], which predicted unsteady venous flow when the diameter of the artery and vein were the same. However, converse to the idealised model of Iori [1], unsteady vortex shedding is also present in arterial sections when the vein is connected to the outer curvature of the arterial bend (P1-OUT and P2-OUT). In particular, within WS during systole, flow in the arterial sections of P1-OUT and P2-OUT appear to be more unstable than flow in the arterial sections of P1-IN and P2-IN.

However, within WD during diastole, the picture is less clear. Converse to the results from WS, it appears that P1-IN is relatively more unsteady than P1-OUT. However, results from P2-IN and P2-OUT are similar.



(a) P1-IN, t=1.23s

(b) P1-OUT, t=1.23s

(c) P2-IN, t=1.23s

(d) P2-OUT, t=1.23s

(e) P1-IN, t=1.60s

(f) P1-OUT, t=1.60s

(g) P2-IN, t=1.60s

(h) P2-OUT, t=1.60s

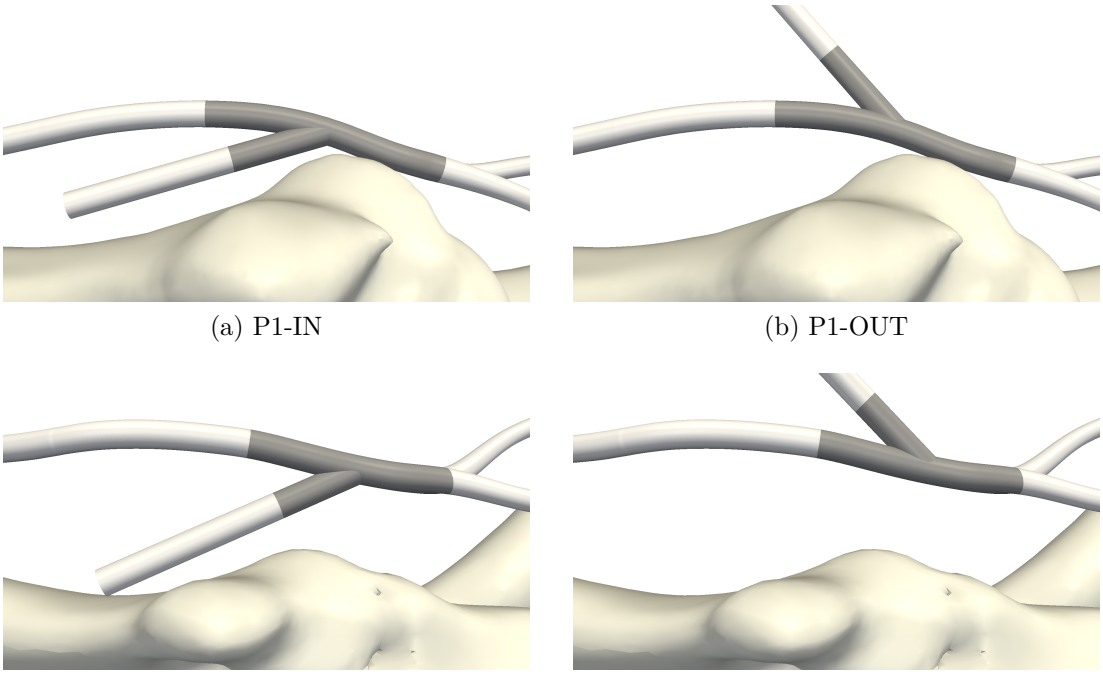
Figure 3.12: Snapshots of plane-normal vorticity on planes within each AVF configuration at 1.23s, which is during systole (marked with vertical dotted lines in Fig. 3.4), and at 1.60s, which is during diastole (marked with vertical dashed-dotted lines in Fig. 3.4).

3.3.1.2 Quantitative Insight

DMD was employed to compute the intensity γ for $\boldsymbol{\tau} - \overline{\boldsymbol{\tau}}_t$, where $\boldsymbol{\tau}$ is the space-time WSS vector field and $\overline{\boldsymbol{\tau}}_t$ is the temporal average of the space-time WSS vector field respectively in an arterial section of each AVF configuration near the anastomosis (see Fig. 3.13) and in the vein. Specifically, DMD was undertaken in WS, WD and WT for the arterial region, and only in WT for the venous region. For WT, 1250 temporal snapshots with a uniform spacing of 0.0008s were used. For WS and WD, 750 temporal snapshots with a uniform spacing of 0.0004s were used. Results are shown in Fig. 3.14.

It is clear that the WSS in arterial sections of all AVF configurations exhibit high-frequency fluctuations. This unsteadiness appears to be irrespective of whether the venous section of the AVF is connected to the inner or outer curvature of an arterial bend; converse to the idealised model of Iori [1] which predicted that connecting the venous section of the AVF to the outer curvature of an arterial bend would suppress unsteadiness in the artery. Further observations can also be made. Firstly, within WS during systole, P1-OUT and P2-OUT appear to have relatively more energy in higher frequency modes than P1-IN and P2-IN respectively, while both P1-IN and P2-IN exhibit a characteristic frequency close to 100Hz similar to the one found in [1]. These results are in line with the qualitative observations of section 3.3.1.1. However, within window WD during diastole, the picture is less clear. Converse to the results from WS, it appears that P1-IN has relatively more energy in higher frequency modes than P1-OUT, while for P2-IN and P2-OUT the differences are less distinct.

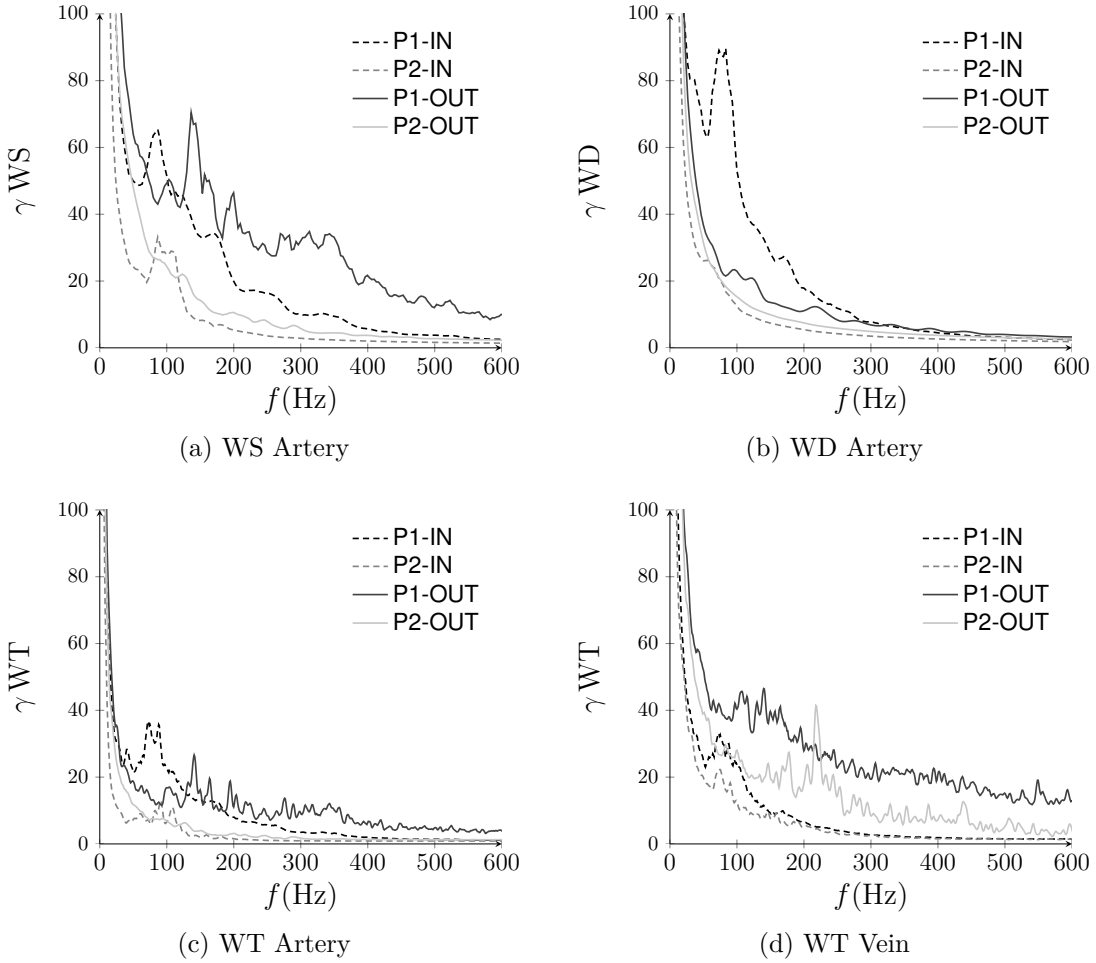
Finally, it is clear that all the venous sections of all AVF configurations exhibit high-frequency fluctuations. This results is in line with the qualitative observations of section 3.3.1.1, however it is also clear that the flow in the vein of P1-OUT and P2-OUT presents higher unsteadiness than the venous flow of P1-IN and P2-IN.



(a) P1-IN (b) P1-OUT

(c) P2-IN (d) P2-OUT

Figure 3.13: Regions of arterial and venous sections from which $\boldsymbol{\tau} - \overline{\boldsymbol{\tau}}_t$ were extracted for the DMD analysis are shaded in grey.



(a) WS Artery

(b) WD Artery

(c) WT Artery

(d) WT Vein

Figure 3.14: Intensity γ from the DMD of $\boldsymbol{\tau} - \overline{\boldsymbol{\tau}}_t$ from (a) WS in the arterial section (b) WD in the arterial section (c) WT in the arterial section (d) WT in the vein.

3.3.1.3 Summary

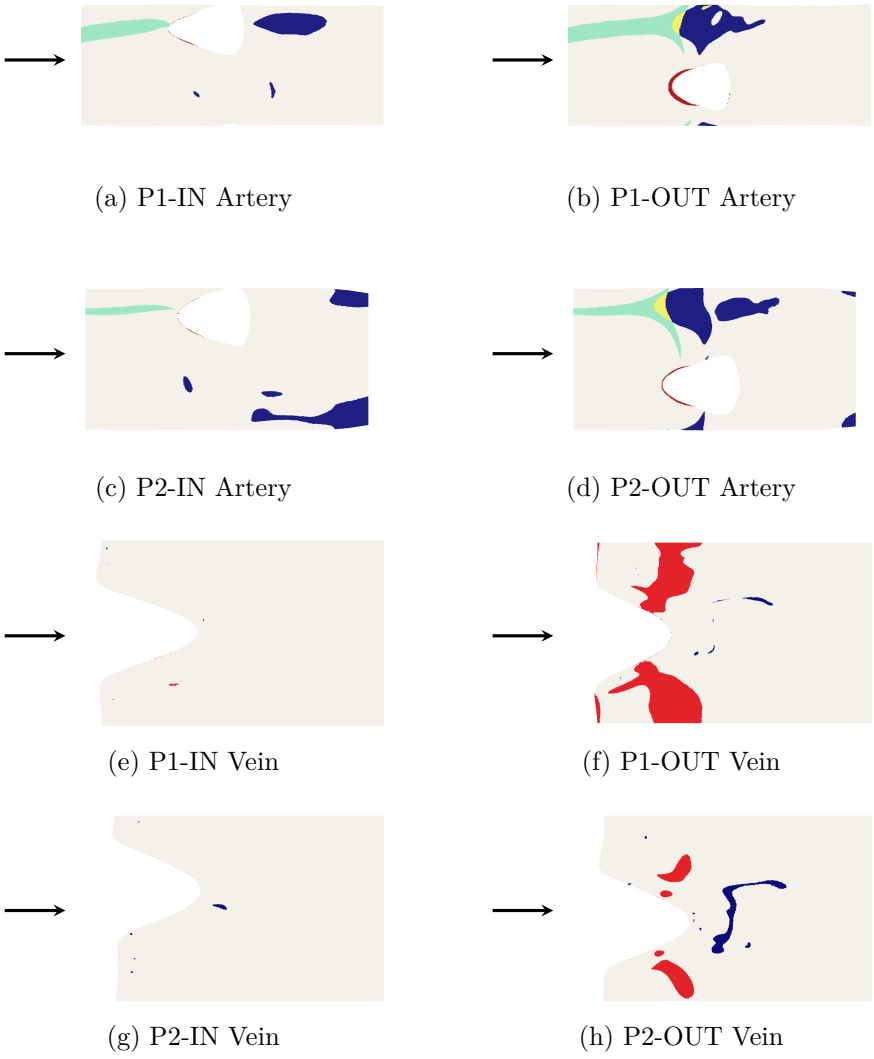
The main finding of the above unsteady analysis is that, converse to results from previous more idealised studies [1], forming an AVF by connecting a vein onto the outer curvature of an arterial bend does not, necessarily, suppress high-frequency unsteady flow in the artery. Specifically, during systole, outer configurations are actually more unstable than inner configurations, and whilst this appears somewhat reversed in diastole, the situation is less clear, and all configurations

exhibit a degree of unsteadiness.

During WS, in systole, the average flow split between the vein and the distal arteries is $\sim 60 : 40$. This is significantly more even than the fixed flow split of $80 : 20$ prescribed by Iori *et al.* [1]. It can be speculated that this more even flow split during WS causes the outer configurations to become unstable; noting in particular from Fig. 3.12 that during WS the outer configurations become unstable in arterial sections distal to the anastomosis, when/where the current simulations exhibit a relatively higher flow rate *cf.* Iori *et al.* [1]. This assertion is further supported by the fact that during WD, in diastole, the average flow split between the vein and the distal arteries is $\sim 78 : 22$, and the outer configurations recover a degree of stability — although not enough to overcome the unsteadiness induced during WS.

3.3.2 Time-Averaged Analysis

3.3.2.1 Wall Shear Stress and Wall Normal Oxygen Flux



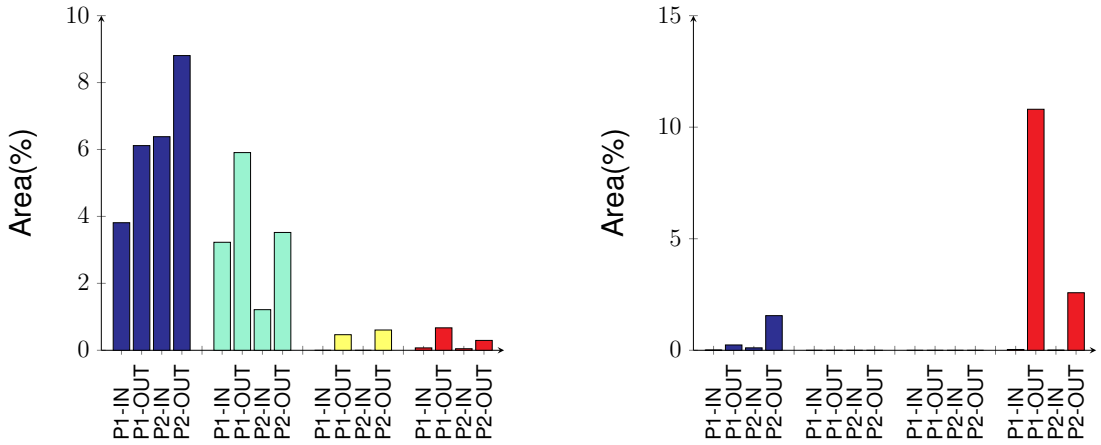
(a) P1-IN Artery (b) P1-OUT Artery

(c) P2-IN Artery (d) P2-OUT Artery

(e) P1-IN Vein (f) P1-OUT Vein

(g) P2-IN Vein (h) P2-OUT Vein

Figure 3.15: Quad-color maps of WSS^- (blue), WSS^+ (red), $LWNOF^-$ (green), and the intersection between regions of WSS^- and $LWNOF^-$ (yellow) in excised and flattened arterial sections of Fig. 3.13 of P1-IN (a), P1-OUT (b), P2-IN (c), P2-OUT (d) and in excised and flattened venous sections of Fig. 3.13 of P1-IN (e), P1-OUT (f), P2-IN (g), P2-OUT (h). Arrow indicates direction of blood flow. The white holes mark the location of the venous anastomoses.



(a) Artery (b) Vein

Figure 3.16: Bar chart showing the percentage area of WSS^- (blue), WSS^+ (red), $LWNOF^-$ (green), and the intersection between regions of WSS^- and $LWNOF^-$ (yellow), in excised and flattened arterial sections of each configuration (a) and in excised and flattened venous sections of each configuration (b).

Quad-color maps on the excised and flattened arterial and venous sections from each AVF of WSS^- ('pathologically low' time-averaged WSS magnitude < 0.5Pa), WSS^+ ('pathologically high' WSS magnitude > 30Pa), $LWNOF^-$ ('pathologically low' time-averaged LWNOF $< 4.275 \times 10^{-7}\text{mol}\,\text{m}^{-2}\text{s}^{-1}$), and the intersection between regions of WSS^- and $LWNOF^-$ are shown in Fig. 3.15. Bar charts showing the percentage area of WSS^-, WSS^+, $LWNOF^-$, and the intersection between regions of WSS^- and $LWNOF^-$ in the excised and flattened arterial and venous sections of each configuration are shown in Fig. 3.16. Note that LWNOF is defined here as $-2\kappa\mathbf{n}\cdot\boldsymbol{\nabla}c$, where $\mathbf{n}$ is the outward facing wall normal and the factor of two accounts for the role of haemoglobin [92].

Following Iori *et al.* [1], the pathologically low WSS threshold of 0.5Pa was chosen to be at the lower-bound of estimates made by various authors, including Masuda *et al.* [106] and Sho *et al.* [107, 108] who suggest 0.5Pa (in rabbits), Dolan *et al.* [44] who suggest 1Pa, and Irace *et al.* [109] who suggest 1.8Pa. The pathologically high WSS threshold of 30Pa was chosen to be at the upper-bound of

estimates made by various authors, including Dolan *et al.* [44] who suggest 10Pa, and Dolan *et al.* [38] who suggest up to 30Pa. The pathologically low LWNOF threshold was obtained by assuming that the innermost region of the vascular wall (*i.e.* the intima and media) receive oxygen solely from luminal blood [110][53] and not from the adventitial vasa vasorum. With the further assumptions that this innermost region requires oxygen at a rate of at least $8.55 \times 10^{-3}\text{mol} \cdot \text{m}^{-3} \cdot \text{s}^{-1}$ in order to avoid hypoxia (based on measurements of oxygen consumption in smooth muscle cells of dog femoral arteries [111]), and that it has a thickness of $5 \times 10^{-5}\text{m}$ (based on measurements in dog femoral arteries [112]), one obtains the threshold of $4.275 \times 10^{-7}\text{mol} \cdot \text{m}^{-2} \cdot \text{s}^{-1}$.

It can be seen that for the P1-OUT and P2-OUT configurations the artery is exposed to significantly more WSS^- than for the P1-IN and P2-IN configurations. Also, for the P1-OUT and P2-OUT configurations, a triangular shaped region of LWNOF^- is present in the artery opposite the anastomosis, where stenosis in AVF have previously been observed [97], as is a region of overlap between WSS^- and LWNOF^-. Neither of these features are present for the P1-IN and P2-IN configurations. These findings are in agreement with results of previous more idealised studies [1], and add further support to the assertion that connecting a vein to the outer curvature of an arterial bend may suppress IH *if* it is caused by low WSS and/or low LNWOF (leading to wall hypoxia). Finally, for the P1-OUT and P2-OUT configurations the vein is exposed to significantly more WSS^+ than for the P1-IN and P2-IN configurations. Previous more idealised studies, where the vein and artery had the same diameter [1], exhibited the same trend. However, the difference in this study between inner and outer curvature configurations was far more marked.

3.3.2.2 Summary

The main finding of the above time-averaged analysis is that, in agreement with results from previous more idealised studies, forming an AVF by connecting a vein onto the inner curvature of an arterial bend will suppress exposure to regions of low wall shear stress and hypoxia in the artery. Results also show that forming an AVF by connecting a vein onto the inner curvature of an arterial bend will significantly reduce exposure to high WSS in the vein.

3.4 Conclusions

The previous work by Iori [1], which investigated the effect of planar arterial curvature on flow and oxygen transport patterns in idealised AVF with non-pulsatile inflow conditions, has been extended to more realistic non-planar brachiocephalic AVF configurations with pulsatile inflow conditions. Results from these more realistic simulations show that forming an AVF by connecting a vein onto the outer curvature of an arterial bend does not, necessarily, suppress unsteady flow in the artery. Specifically, during systole, outer configurations are actually more unstable than inner configurations, and whilst this is somewhat reversed in diastole, the situation is less clear, and all configurations exhibit a degree of unsteadiness. This finding is converse to results from previous more idealised studies [1]. However, results also show that forming an AVF by connecting a vein onto the inner curvature of an arterial bend will suppress exposure to regions of low wall shear stress and hypoxia in the artery. This finding is in agreement with results from previous more idealised studies [1]. Finally, results show that forming an AVF by connecting a vein onto the inner curvature of an arterial bend will significantly reduce exposure to high WSS in the vein. Reducing exposure to excessively low/high levels of WSS and regions of hypoxia may reduce rates of IH and hence AVF failure.

Chapter 4

Optimisation of Arterio-Venous Fistulae for Suppressing Unsteady Flow

4.1 Introduction

The previous chapter showed that under realistic arterial geometries and pulsatile boundary conditions the flow presented high frequency unsteadiness both in outer and in inner configurations. The finding is converse to results from previous more idealised studies [1]. However, flow within the venous section, where pathology is also known to develop, typically exhibited significant unsteadiness also in [1]. The present chapter is divided in two main parts. In Sec. 4.2 a Mesh Adaptive Direct Search (MADS) optimisation framework, CFD simulations in steady conditions, and a new cost function, are employed to design an AVF configuration that possibly suppresses high-frequency flow unsteadiness throughout the AVF, in both arterial and venous sections. Subsequently, in Sec. 4.3, performance of the optimal configuration is assessed with a fully pulsatile simulation. The aim of

this work is to understand both if cheaper simulations with steady boundary conditions are still a viable option to suppress high-frequency unsteady flows in AVF, and to find which geometric parameters are more important to obtain steady flow in AVF, eventually to guide the surgical procedure for upper arm AVF.

4.2 Optimisation

4.2.1 Overview

The optimisation approach used in this work is based on the MADS method proposed by Audet and Dennis [113, 114], and uses simple Kriging [115, 116] as a surrogate model to predict values of the objective function. A detailed description of the Kriging surrogate model is given in the appendix A. Similar approaches have recently been used to design various medical devices and surgical procedures [117, 118, 119, 120], including Y-shaped grafts used in the Fontan procedure [118, 119], and cardiovascular stents [120, 121].

4.2.2 Parameterisation

The artery was constructed by sweeping a circular section with diameter $D_A = 5 \times 10^{-3}$m along a plane-arc centreline $\mathbf{x}_A$ defined as

$$\mathbf{x}_A = [20D_A \sin(q), 20D_A \cos(q) - 20D_A, 0], \tag{4.1}$$

with $q \in [-30, 30]$, which runs from the Proximal Arterial Inlet (PAI) to the Distal Arterial Outlet (DAO). *A priori* description of a curved arterial section is based on the recent findings of Iori *et al.* [1], who showed that arterial curvature can have an significant impact on unsteadiness in AVF. The vein was constructed by sweeping a circular section with diameter D_A along a two-piece cubic hermitian

spline $\mathbf{x}_V$ defined as

$$\mathbf{x}_V = \sum_{i=0}^{1}(2q^3-3q^2+1)\mathbf{p}_i+q(q^2-2q+1)\mathbf{m}_i+q^2(-2q+3)\mathbf{p}_{i+1}+q^2(q-1)\mathbf{m}_{i+1}, \quad (4.2)$$

where $q \in [0,1]$,

$$\mathbf{p}_0 = [0,0,0] \quad (4.3)$$

is where the arterial and venous centrelines intersect,

$$\mathbf{p}_1 = [x_{p1}, y_{p1}, z_{p1}] \quad (4.4)$$

is a mid-point on the venous centreline,

$$\mathbf{p}_2 = [-10D_A, 5D_A\cos(\xi), 5D_A\sin(\xi)] \quad (4.5)$$

is the location of the Distal Venous Outlet (DVO),

$$\mathbf{m}_0 = [10D_A\cos(\theta)\sin(\phi), 10D_A\sin(\theta)\sin(\phi), 10D_A\cos(\phi)] \quad (4.6)$$

is a tangent where the arterial and venous centrelines intersect,

$$\mathbf{m}_2 = [-10D_A, 0, 0] \quad (4.7)$$

is a tangent at the DVO, and finally

$$\mathbf{m}_1 = 0.75(\mathbf{p}_2 - \mathbf{p}_0) - 0.25(\mathbf{m}_2 + \mathbf{m}_0) \quad (4.8)$$

is a tangent at a mid-point on the venous centreline, defined such that the venous centreline is $C2$ continuous.

$\mathbf{p}_0$, the intersection point between the artery and the vein, for construction, coincides with the origin of the reference system $\mathbf{O}$. The resulting AVF configura-

tion is parameterised by a set of six parameters x_{p1}, y_{p1}, z_{p1}, θ, ϕ, ξ, which are constrained such that $x_{p_1} \in [-7D_A, 7D_A]$, $y_{p_1} \in [-7D_A, 7D_A]$, $z_{p_1} \in [-7D_A, 7D_A]$, $\theta \in [180, 360]$, $\phi \in [90, 270]$, and $\xi \in [0, 360]$. Additionally, the variables were constrained such that the configuration was not self-intersecting, the maximum venous curvature was less than $1.8/D_A$, the venous length was less than $20D_A$, the whole AVF configuration fitted within an infinitely long cylinder, aligned with the x-axis, and centred on the origin, with a radius of $7.5D_A$. These parameters were chosen to ensure that the resulting geometry had clinical/anatomical relevance. A schematic illustration of the arterial and venous centrelines is shown in Fig. 4.1.

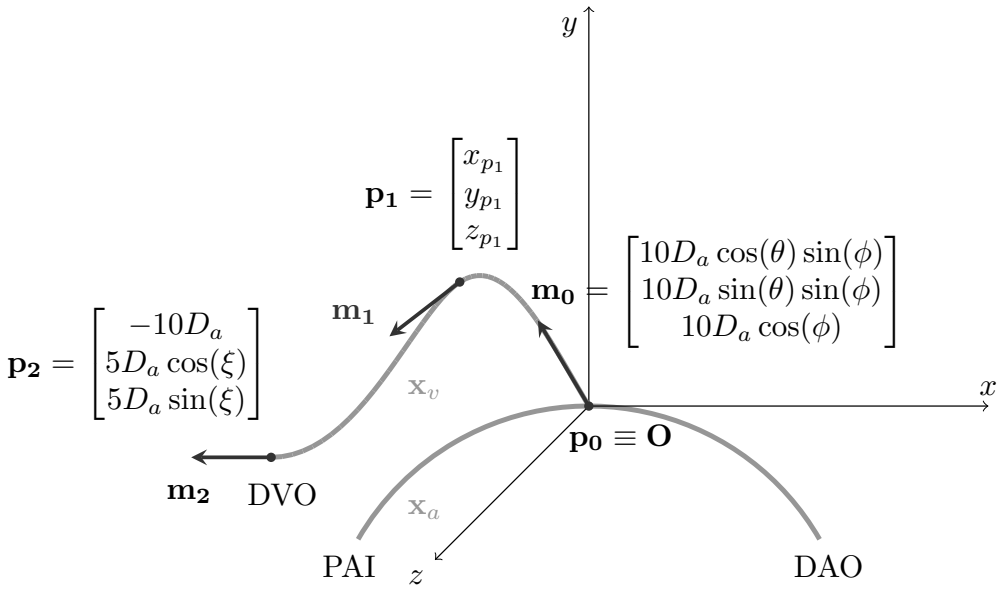


Figure 4.1: Schematic illustration of arterial and venous centrelines, along with associated parameterisation.

4.2.3 Cost Function

4.2.3.1 Definition

A new cost function that indicates whether a particular AVF configuration is likely to induce unsteady flow patterns is introduced. To evaluate the cost function for a particular configuration first is found a steady-state solution to the continuity equation 3.1, and the steady-state incompressible Navier-Stokes equations for a Newtonian fluid

$$\rho \mathbf{u} \cdot \boldsymbol{\nabla} \mathbf{u} + \boldsymbol{\nabla} p = \mu \boldsymbol{\nabla}^2 \mathbf{u}, \tag{4.9}$$

where μ is the viscosity of human blood, ρ is the density of human blood, $\mathbf{u}$ is the three-dimensional blood velocity (vector) field, and p is the pressure. For all configurations, values of $\mu = 3.5{\times}10^{-3}\mathrm{Pa} \cdot \mathrm{s}$ and $\rho = 1060\mathrm{kg} \cdot \mathrm{m}^{-3}$ were employed. Also, for all configurations, steady-state parabolic velocity profiles were applied at the PAI and DAO, with average velocities of $\overline{u_{PAI}} = 0.528\mathrm{m} \cdot \mathrm{s}^{-1}$ into the configuration and $\overline{u_{DAO}} = 0.106\mathrm{m} \cdot \mathrm{s}^{-1}$ out of the configuration respectively. This resulted in a Reynolds number of 800 at the PAI, and an 80:20 flow split between the DVO and DAO for each configuration [122, 123]. The resulting Dean number was $De = 126$ for the arterial section, and could vary locally between a minimum $De = 0$ to a maximum $De \simeq 600$ in the venous sections. Finally, a constant (and arbitrary) pressure was applied at the DVO of each configuration, and a zero-velocity no-slip condition was applied at the arterial and venous walls, which were assumed to be rigid.

The resulting steady-state solution is then used as the initial condition for Eq. 3.1 and the unsteady incompressible Navier-Stokes equations 3.2 with the same parameter values and boundary conditions employed for the steady-state problem. Any subsequent divergence of the solution from the steady-state initial condition can be used as a proxy for unsteadiness in the particular configuration.

Specifically, the cost function Ψ is defined as the maximum percentage surface area of the configuration that has at least a 10% deviation in WSS magnitude from the steady-state solution during the interval $5t_c \leq t \leq 10t_c$, where t_c is the characteristic time $t_c = D_{PAI}/\overline{u_{PAI}}$, thus

$$\Psi = \max_{5t_c \leq t \leq 10t_c} \left(\frac{1}{\Gamma} \int_{\Gamma} \psi(\mathbf{x}, t) \, \mathrm{d}\mathbf{x} \right) \times 100, \tag{4.10}$$

where Γ is the surface area of the given configuration and

$$\psi(\mathbf{x}, t) = \begin{cases} 1 : \tau_D(\mathbf{x}, t) > 10 \\ 0 : \text{elsewhere} \end{cases}, \tag{4.11}$$

where

$$\tau_D(\mathbf{x}, t) = \frac{|\tau_S(\mathbf{x}) - \tau_U(\mathbf{x}, t)|}{\tau_S(\mathbf{x})} \times 100, \tag{4.12}$$

$\tau_S(\mathbf{x})$ is the WSS magnitude from the steady-state solution, and $\tau_U(\mathbf{x}, t)$ is the WSS magnitude from the unsteady solution.

4.2.3.2 Computational Method

Star-CCM+ v9.06.9 (CD-Adapco, Melville, NY USA) was used to solve Eq. 3.1 with either Eq. 4.9 or Eq. 3.2. to obtain Ψ for a given AVF configuration. Specifically, 1000 iterations of the segregated steady-state solver were used to solve Eq. 3.1 with Eq. 4.9, and the segregated implicit unsteady solver with a time-step $dt = t_c/20$, resulting in $dt = 4.735 \times 10^{-4}$s was used to solve Eq. 3.1 with Eq. 3.2. Polyhedral unstructured volume meshes, with prismatic boundary layer meshes adjacent to the wall, were constructed for each configuration. The meshes were refined near the anastomosis. Specifically, elements near the anastomosis had an average size of 1.5×10^{-4}m, expanding progressively to 3×10^{-4}m beyond a distance of $\sim 2.5 \times 10^{-2}$m from the anastomosis. The prismatic boundary layer meshes were 10 elements thick, with the first element having a thickness of

3.23×10^{-5}m. Each mesh had $\sim 1 \times 10^6$ elements in total. The author notes that this mesh resolution is lower than that employed by Iori *et al.*. However, it is similar to that employed in other studies of unsteady flow in AVF [69, 68]. Moreover, performance of the optimal configuration will be assessed with a higher-resolution simulation in section 4.3.

4.2.4 Optimisation Framework

4.2.4.1 Initial Seeding

The Kriging-based surrogate model of Ψ was initially seeded with data at a Latin Hypercube Sampling (LHS) of the six-dimensional parameter space [115, 116]. Specifically, 600 initial configurations that satisfied $x_{p_1} \in [-7D_A, 7D_A]$, $y_{p_1} \in [-7D_A, 7D_A]$, $z_{p_1} \in [-7D_A, 7D_A]$, $\theta \in [180, 360]$, $\phi \in [90, 270]$, and $\xi \in [0, 360]$ were identified via LHS. Of these 600 configurations, 509 were rejected because they violated the constraints on maximum venous curvature, venous length, and overall AVF size or led to unfeasible simulations. Values of x_{p1}, y_{p1}, z_{p1}, θ, ϕ, and ξ for the remaining 91 valid AVF configurations, along with calculated values of Ψ, are shown in Fig. 4.2. A sample of the 91 valid AVF configurations are shown in Fig. 4.3, where the surfaces are coloured by $\overline{\psi}_t(\mathbf{x})$, defined as

$$\overline{\psi}_t(\mathbf{x}) = \begin{cases} 1 : \overline{\tau}_D(\mathbf{x}) > 10 \\ 0 : \text{elsewhere} \end{cases}, \tag{4.13}$$

where $\overline{\tau}_D(\mathbf{x})$ is the time-averaged $\tau_D(\mathbf{x}, t)$ over the period $5t_c - 10t_c$. The richness of the parameter space is apparent. The initial Kriging-based surrogate model of Ψ was calculated using the Matlab Dace toolbox [124].

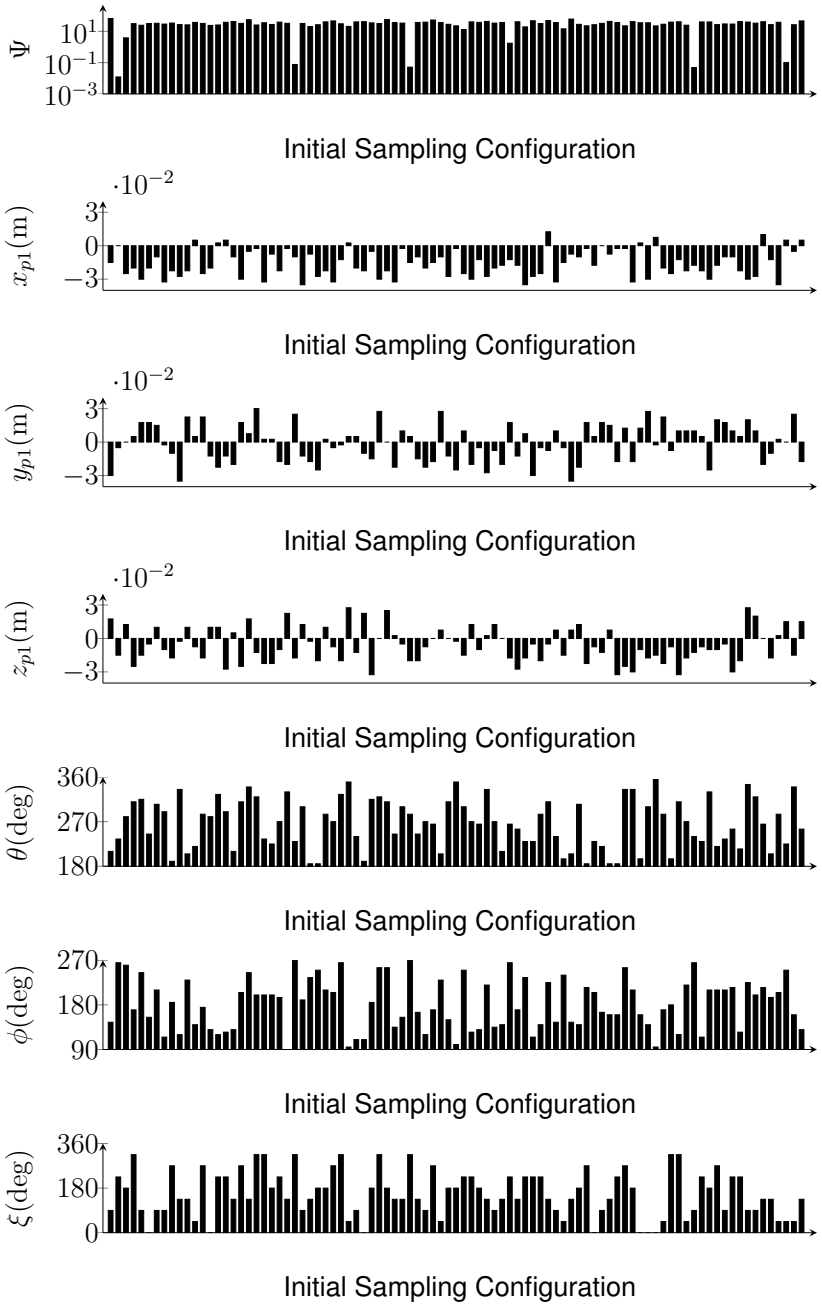


Figure 4.2: Values of x_{p1}, y_{p1}, z_{p1}, θ, ϕ, ξ, and Ψ for the 91 AVF configurations used to seed the Kriging-based surrogate model of Ψ.



Figure 4.3: A sample of the 91 valid AVF configurations used to resemble the Kriging-based surrogate model of Ψ. The surfaces are coloured by $\overline{\psi}_t(\mathbf{x})$, black for $\overline{\psi}_t(\mathbf{x}) = 1$, white otherwise. The richness of the parameter space is apparent.

4.2.4.2 Mesh Adaptive Direct Search Method

Having initialised the Kriging-based surrogate model Ψ_e of Ψ, the Mesh Adaptive Direct Search (MADS) [113] method was used to search for the set of parameters $\mathbf{s}^*$ such that

$$\Psi(\mathbf{s}^*) \leq \Psi(\mathbf{s}) \ \ \forall \ \ \mathbf{s} \in \mathbf{S} \tag{4.14}$$

where $\mathbf{S}$ is the set of all feasible configurations.

The MADS method is an iterative derivative-free approach introduced by Audet and Dennis [113, 114]. A flow diagram explaining how iterations proceed through so-called SEARCH and POLL steps is shown in Fig 4.4.

During the SEARCH step, the Kriging-based surrogate model of the function Ψ will be used to compute Ψ_e, the estimate of Ψ on a finite subset of trial points. The set $\widetilde{\mathbf{S}}_k$ defines the set of parameters tried during the optimisation framework that led to feasible geometries, with $\widetilde{\mathbf{S}}_0$ defining the set of parameters in the initial LHS that led to feasible geometries. More specifically,

$$\widetilde{\mathbf{S}}_k = \mathbf{S}_k - W(\mathbf{S}_k), \tag{4.15}$$

where $\mathbf{S}_k$ is the set of all the parameters tried, and $W(\mathbf{S}_k)$ is the subset of parameters in $\mathbf{S}_k$ that led to simulations that could not be solved (e.g. the geometries were self-intersecting) At each iteration k, the surrogate model Ψ_e was built over $\widetilde{S}_k$, and evaluated on points of the mesh $\widetilde{M}_k$,

$$\widetilde{M}_k = M_k - \Gamma(M_k) - \Pi(M_k), \tag{4.16}$$

where $\Gamma(M_k)$ is the set of configurations in M_k that violate constraints on maximum venous curvature, venous length, and overall AVF size, $\Pi(M_k)$ the set of configurations in M_k that have venous centrelines within 1×10^{-3}m of venous

centrelines associated with any configuration in $\mathbf{S}_k$, and

$$M_k = \bigcup_{\mathbf{s} \in \mathbf{S}_k} \{\mathbf{s} + \Delta_k \mathbf{D}\mathbf{z} : \mathbf{z} \in \mathbb{N}^{n_D}\}, \tag{4.17}$$

where n is the number of parameters (6 in this case), n_D is $2n$, D is an $n \times n_D$ positive spanning matrix, z in a vector of integers of length $2n$, Δ_k is the mesh size at iteration k. In this work, it was chosen to use $D = [I_n, -I_n]$ with I_n the identity matrix of dimension n. If the mesh size $\Delta_k \leq 1/4$, Ψ_e was evaluated over the whole $\widetilde{M}_k$, otherwise Ψ_e was evaluated on a subset of $\widetilde{M}_k$ calculated from a LHS of M_k containing 10^4 points, and that will be called $\widetilde{M}_k^{LHS}$.

η_k is defined as the group of 4 parameter sets containing the three configurations in $\widetilde{M}_k$ or $\widetilde{M}_k^{LHS}$ that have the lowest Ψ_e and which have venous centrelines that depart from each other by at least 1×10^{-3}m, and the single configuration with the highest MSE.

The parameter set $\mathbf{s_k}$ represents the point where the objective function Ψ assumes the current minimum value. If Ψ assumes a smaller value than the current optimum on one of the newly tested set η_k, $\mathbf{s_k}$ is updated, $\Delta_{k+1}^m = \min(4\Delta_k, 1)$, $k = k + 1$, and the SEARCH step is repeated calculating Ψ_e over the updated $\widetilde{\mathbf{S}_k}$, otherwise, if no trial point improves the objective function, the iteration goes to the POLL step. During the POLL step the real value of objective function Ψ (calculated through CFD simulation) is evaluated on a set P_k, with

$$P_k = \{\mathbf{s_k} + \Delta_k d : d \in D_k\} \subset M_k \tag{4.18}$$

where D_k is a positive spanning set of $n + 1$ dimensions, with $\Delta_k ||d||_\infty \leq \Delta_k^p$, and where Δ_k^p is the poll size parameter calculated. In this work the relationship $\Delta_k^p = n\sqrt{\Delta_k^m}$ was used.

One of the properties of the MADS algorithm is that, when Δ_k^p and Δ_k^m go to zero, the number of candidate site points for poll increase. The generation

of the positive basis D_k follows the rules described in [113]. The new poll set was imposed having to find at least one feasible parameters set, otherwise a new poll set was recomputed. If during the POLL step, an improved mesh point is found, $\mathbf{s}_k$ is updated, $\Delta^m_{k+1} = \min(4\Delta^m_k, 1)$, $k = k + 1$, otherwise $\mathbf{s}_{k+1} = \mathbf{s}_k$, $\Delta^m_{k+1} = \Delta^m_k/4$, $k = k+1$, and the optimisation framework returns to the SEARCH step, and the set P_k is added to $\mathbf{S}_k$. SEARCH and POLL are repeated until the new $\Delta^m_k < \Delta^m_{k\ min}$, with $\Delta^m_{k\ min} = 1/64$.

The optimisation framework calculated 29 sets from the MADS method. Specifically, during the MADS method 39 new sets were tried, 10 of which led to self-intersecting geometries. The optimal geometry was found at the 22nd simulation of the MADS optimisation framework (corresponding to the 16th feasible simulation), and led to $\Psi = 0.0062$. Ref a fig of the MADS variation Fig. 4.5

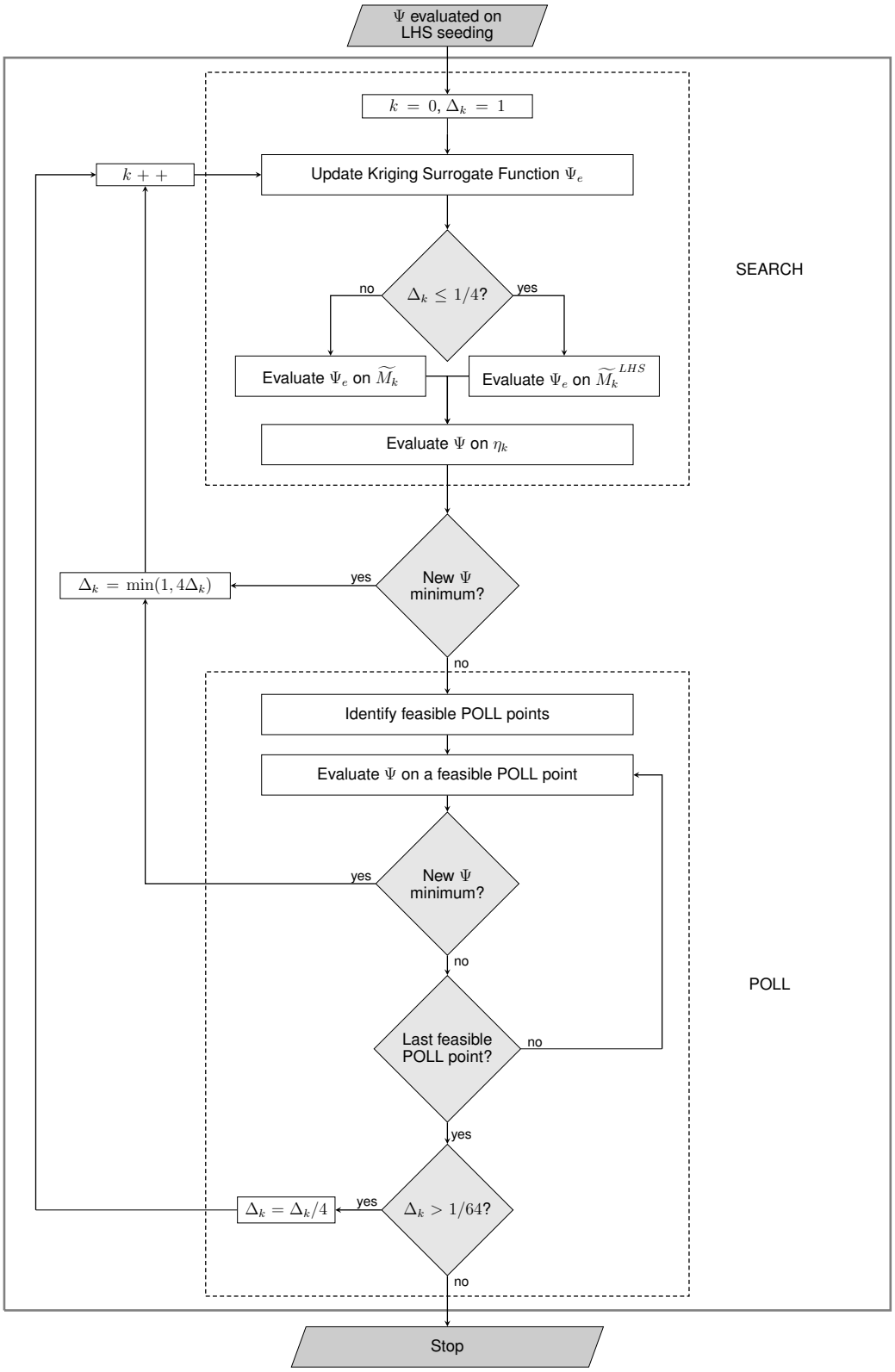


Figure 4.4: MADS flow diagram.

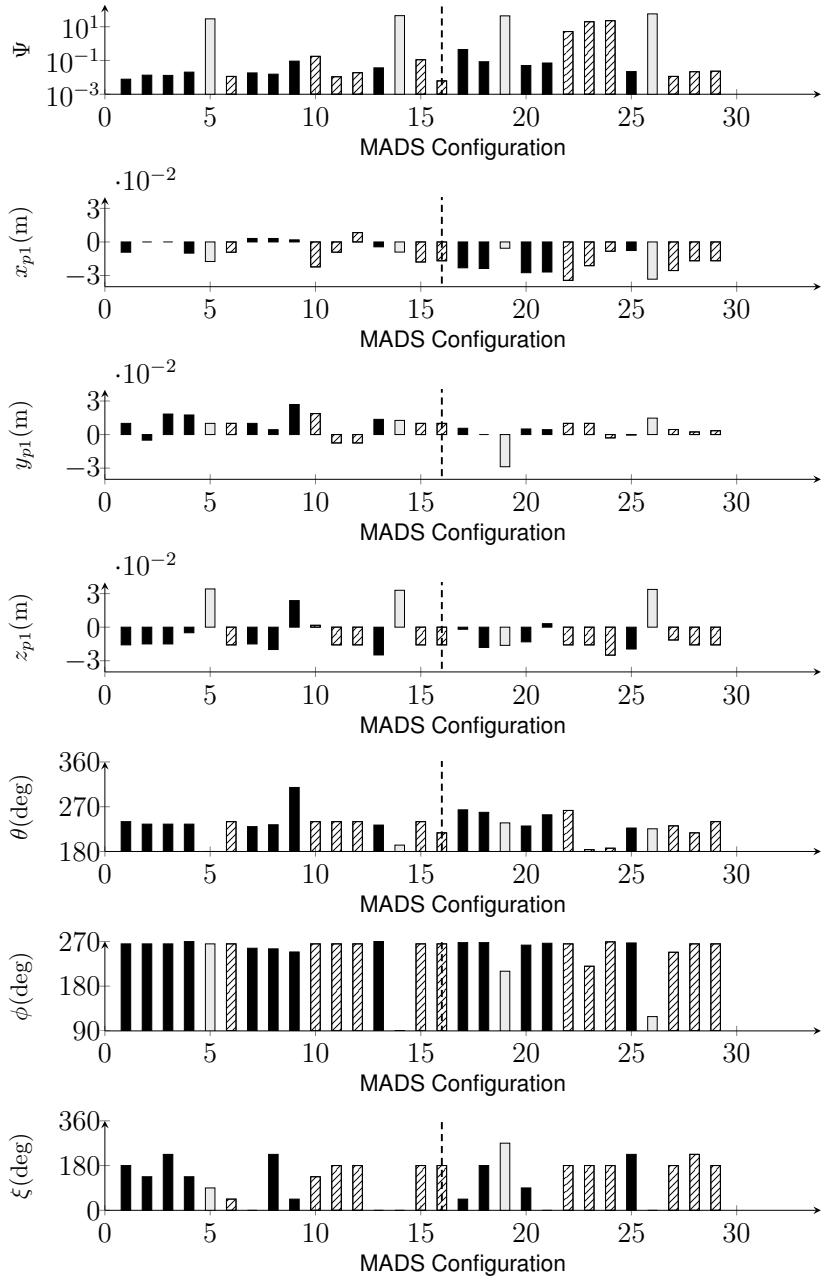


Figure 4.5: The value of the objective function against the number of the feasible simulations during the optimisation process is reported with the corresponding parameters value. The simulations that during the SEARCH step were predicted to give a small value of Ψ are represent with a black bar, the light grey bars represent the simulations run with the Kriging predicted maximal mse value during the SEARCH step, and the bars with diagonal lines represent the feasible simulations run during the POLL step. A dashed line indicates the optimum of Ψ. The optimal geometry was found during a POLL step.

4.2.5 Results and Discussion

The lowest value of Ψ obtained from the optimisation process was 0.0062. The associated parameter values are reported in Table 4.1, and the resulting AVF configuration is shown in Fig 4.6. The optimal configuration features an anastomosis on the outer curvature of the arterial bend, inline with the results of Iori *et al.* [1] who showed that connecting the vein onto the outside of an arterial bend could suppress unsteady flow in the artery. The configuration features also an inherently non-planar looped venous section. Finally it can be noted that, qualitatively, the optimal non-planar configuration bears a resemblance to the 'curved' (as opposed to the 'straight') AVF configuration of Krishnamoorthy *et al.* [65], which increased AVF patency rates in a pig model.

Parameter	Optimal Value
x_{p1}	-1.68×10^{-2}m
y_{p1}	1.00×10^{-2}m
z_{p1}	-1.58×10^{-2}m
θ	217.5°
ϕ	265°
ξ	180°

Table 4.1: Optimal parameter values.

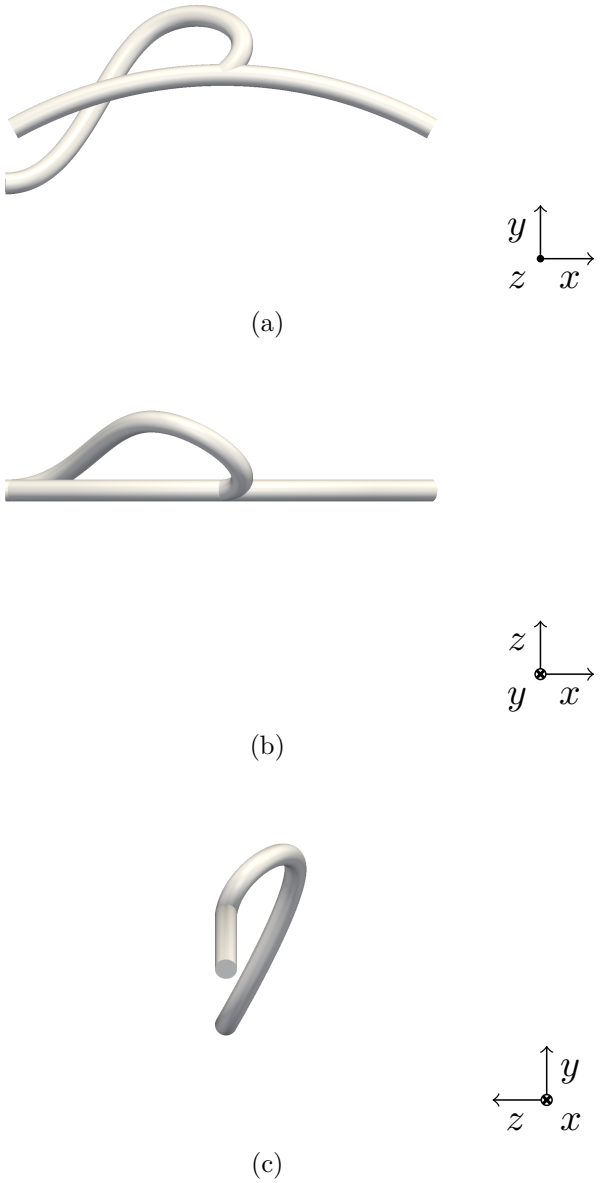


Figure 4.6: Optimal configuration. Salient aspects include an anastomosis on the outer curvature of an arterial bend, and a looped non-planar venous section.

Having identified an optimal configuration, it is useful to assess the sensitivity of Ψ to each of the six geometric parameters. Fig. 4.5 clearly shows that θ and ϕ vary little during the MADS process, suggesting they play an important role, and must remain close to their optimal values. However, ξ varies significantly, indicating it is less critical. Further insight can be gained from Fig. 4.7, which

plots the median, inter-quartile range, and range, of parameters associated with configurations that achieve $\Psi < 0.1$, along with the optimal set of parameter values. Once again, it is clear that θ and ϕ play an important role, and must remain close to their optimal values. However, ξ varies significantly, indicating it is less critical. The plots also suggest that z_{p1} should remain close to its optimal (non-zero) value, signalling the importance of non-planarity. Finally, Fig. 4.8 plots variation of Ψ_e, the Kriging-based surrogate model of Ψ after completion of the MADS process, with x_{p1}, y_{p1}, z_{p1}, θ, ϕ, and ξ, when other parameters are fixed to have values associated with the four most stable configurations; specifically, the optimal configuration with $\Psi = 0.0062$, and three other configurations with $\Psi = 0.0078$, $\Psi = 0.0108$, and $\Psi = 0.0113$. Once again, θ and ϕ appear to be the most important parameters, with ξ in particular having little effect. In summary, the optimal configuration appears particularly sensitive to perturbations of θ and ϕ, which define the angle made between the vein and the curved artery. Non-planarity also appears to be important. However, the location of the distal end of the vein appears to be less important.

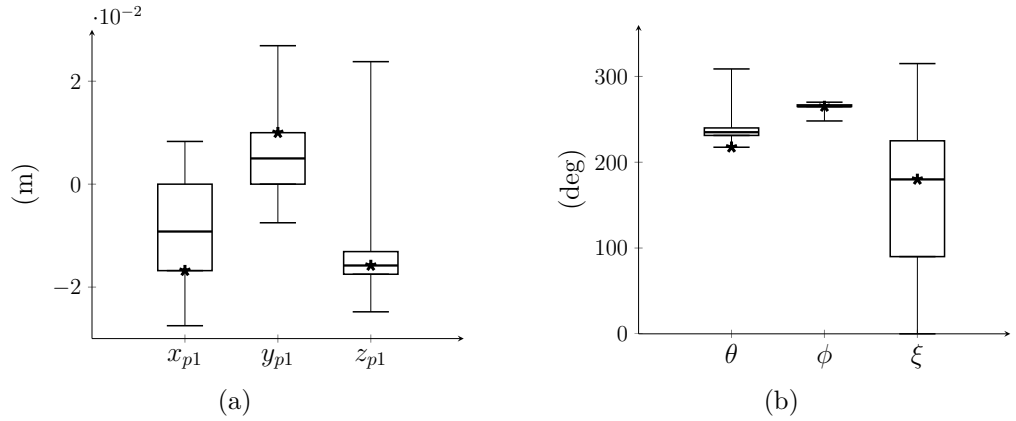


Figure 4.7: Box plots of the median (horizontal black line), inter-quartile range (white box), and range (whiskers), of parameters associated with configurations that achieve $\Psi < 0.1$. Black stars indicate the parameter values of the optimal set. It is clear that θ and ϕ play an important role, and must remain close to their optimal values. However, ξ varies significantly, indicating it is less critical. The plots also suggest that z_{p1} should remain close to its optimal (non-zero) value, signaling the importance of non-planarity.

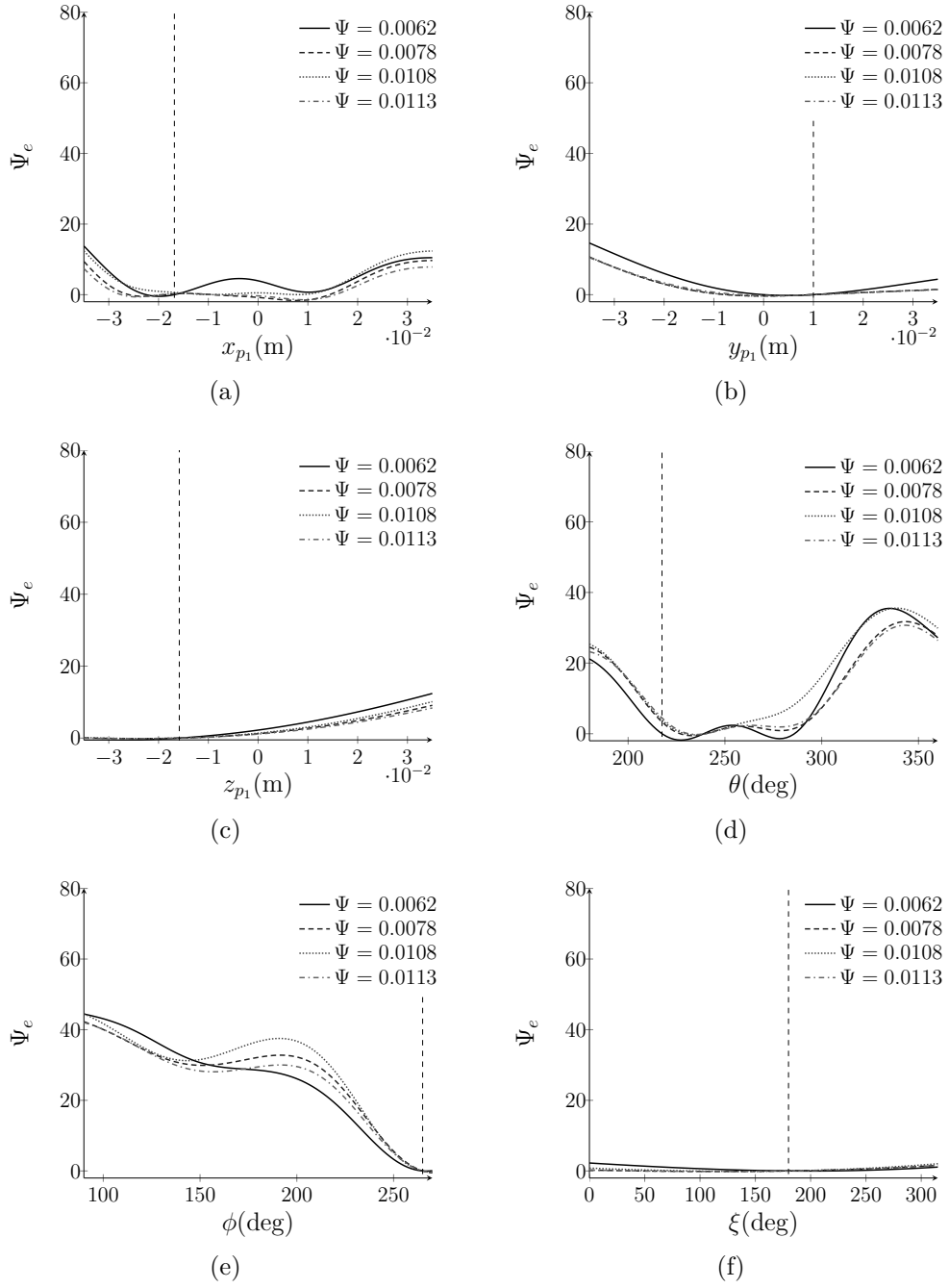


Figure 4.8: Variation of Ψ_e with x_{p1}, y_{p1}, z_{p1}, θ, ϕ, and ξ, when other parameters are fixed to have values associated with the four most stable configurations. Vertical dashed lines denote the optimal parameter values.

4.3 Pulsatile Simulations

4.3.1 Overview

In this section a high-resolution unsteady simulation is undertaken within the optimal AVF configuration to ascertain whether high-frequency unsteadiness remains suppressed when the inflow is pulsatile.

4.3.2 Governing Equations and Boundary Conditions

Blood flow was modelled using Eq. 3.1 and Eq. 3.2, with $\mu = 3.5 \times 10^{-3}\text{Pa} \cdot \text{s}$ and $\rho = 1060\text{kg} \cdot \text{m}^{-3}$.

A space-time varying velocity boundary condition was imposed at the PAI. The inflow waveform was the same used in Sec. 3.2.3.1 and the signal was scaled such that the peak Reynolds number at the PAI was 1300, in agreement with [75]. The resulting time-averaged Reynolds number at the PAI was ~ 750, similar to the time-constant PAI Reynolds number of 800 used during the optimisation process. All flow was prescribed normal to the PAI inflow plane. The PAI inflow rate Q_{PAI} as a function of time is shown in Fig. 4.9.

An RCR Windkessel model was applied at the DAO and DVO. Specifically

$$P_{DAO} = Q_{DAO}(R_{1DAO} + R_{2DAO}) - R_{2DAO}C_{DAO}\frac{\mathrm{d}}{\mathrm{d}t}(P_{DAO} - R_{1DAO}Q_{DAO}), \quad (4.19)$$

and

$$P_{DVO} = Q_{DVO}(R_{1DVO} + R_{2DVO}) - R_{2DVO}C_{DVO}\frac{\mathrm{d}}{\mathrm{d}t}(P_{DVO} - R_{1DVO}Q_{DVO}), \quad (4.20)$$

where P_{DAO} and P_{DVO} are the spatially averaged pressures at the DAO and DVO respectively, Q_{DAO} and Q_{DVO} are the outflow rates at the DAO and DVO respectively, and R_{1DAO}, R_{2DAO}, C_{DAO}, R_{1DVO}, R_{2DVO}, C_{DVO} are relevant Windkessel

parameters. These were selected using the method of Sec. 3.2.3.1. Specifically, values of $R_{1DAO} = 0.78\,\mathrm{mmHg\,ml^{-1}s}$, $R_{2DAO} = 27.0\,\mathrm{mmHg\,ml^{-1}s}$, $C_{DAO} = 0.018\,\mathrm{ml\,mmHg^{-1}}$, $R_{1DVO} = 7.33\,\mathrm{mmHg\,ml^{-1}s}$, $R_{2DVO} = 8.46\,\mathrm{mmHg\,ml^{-1}s}$, $C_{DVO} = 3.48\,\mathrm{ml\,mmHg^{-1}}$ were used. The resulting outflow waveforms Q_{DAO} and Q_{DVO} at the DAO and DVO respectively are shown in Fig. 4.9.

Finally, a no-slip boundary condition was applied at the AVF wall.

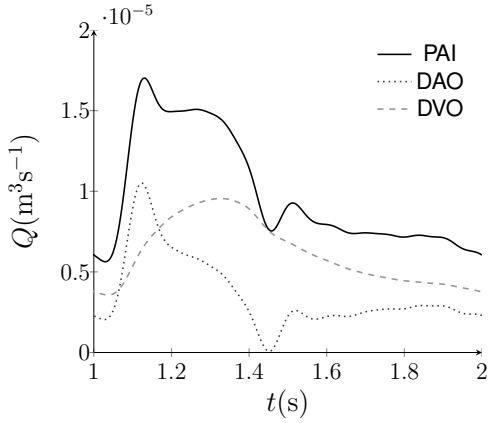


Figure 4.9: Flow waveforms imposed at PAI, and the outflow waveforms at DAO and DVO.

The resulting Womersley number was $Wo = 6.9$, while the maximum Dean number was $De = 204$ in the arterial section, and $De \simeq 390$ in the venous section.

4.3.2.1 Computational Method

Star-CCM+ v9.06.9 (CD-Adapco, Melville, NY USA) was used to solve Eq. 3.1 and Eq. 3.2. in the optimal AVF configuration. The simulation was initialised with zero velocity, a reference pressure of 80mmHg, and run with the coupled steady-state solver until every momentum and mass continuity residual was below 10^{-10}. The resulting steady-state solution was then used as the initial condition for the coupled implicit unsteady solver. This solver was run for 1s (one pulse period) with a time-step of 1×10^{-4}s in order to allow transient 'start-up' phenomena to pass, and then a further 1s (one pulse period) with a time-step of

1×10^{-4}s, during which time data was exported for analysis.

A polyhedral unstructured volume mesh, with a prismatic boundary layer mesh adjacent to the wall, was used for the simulation. The mesh was refined near the anastomosis. Specifically, elements near the anastomosis had an average size of 7×10^{-5}m, expanding progressively to 1.35×10^{-4}m beyond a distance of $\sim 2.5 \times 10^{-2}$m from the anastomosis. The prismatic boundary layer meshes were 25 elements thick, with the first element having a thickness of 2.5×10^{-6}m. The mesh had $\sim 12 \times 10^{6}$ elements in total. This mesh resolution is similar to that used in the previous chapter and in [1].

4.3.3 Results and Discussion

4.3.3.1 Velocity and Vorticity

Fig. 4.10 shows snapshots of velocity magnitude $u(\mathbf{x})$ on the arterial symmetry plane, and on a three-dimensional surface that tracks the venous centreline, at four points in the pulse cycle. Fig. 4.11 shows snapshots of plane-normal vorticity $\omega(\mathbf{x})$ on the arterial symmetry plane, and on a three-dimensional surface that tracks the venous centreline, at four points in the pulse cycle. Fig. 4.12 shows streamlines, originating from the PAI, coloured by velocity magnitude, at four points in the pulse cycle. It is clear that the majority of arterial flow is shifted to the outside of the arterial curvature throughout the pulse cycle, as per Iori *et al.*. It is also apparent that the majority of venous flow is shifted to the outside of the venous curvature throughout the pulse cycle. Finally, it can be observed that a region of re-circulating flow is present adjacent to the inside of the venous curvature, proximal to the anastomosis. The nature of this re-circulating region changes through the pulse cycle. However, fine-scale separated vortical structures, associated with high-frequency flow unsteadiness in previous studies [1, 69, 70, 68], are absent.

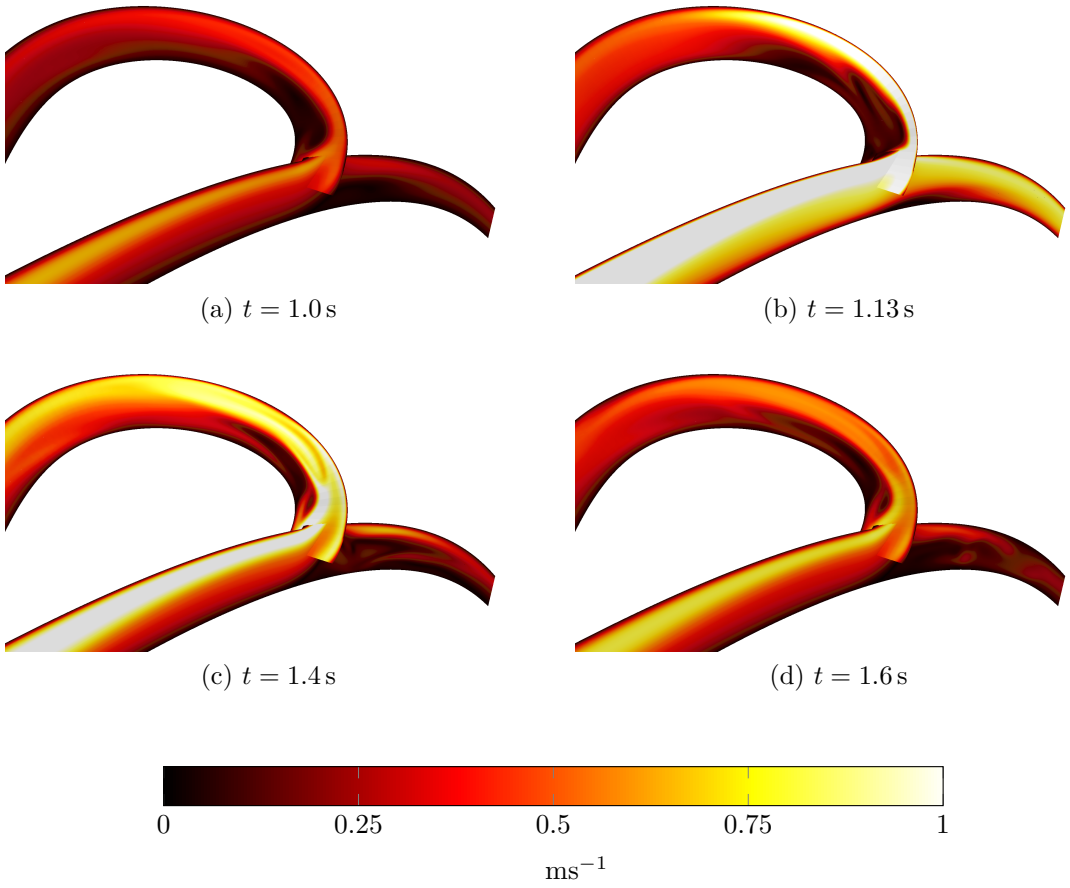


Figure 4.10: Snapshots of $u(\mathbf{x})$ on the arterial symmetry plane, and on a three-dimensional surface that tracks the venous centreline, at four points in the pulse cycle. It is clear that the majority of arterial flow is shifted to the outside of the arterial curvature, and that the majority of venous flow is shifted to the outside of the venous curvature throughout the pulse cycle. A region of re-circulation can also be observed to the inside of the venous curvature, proximal to the anastomosis. The nature of this region of re-circulation changes through the pulse cycle, however, disturbed flow associated with high-frequency flow unsteadiness is absent.

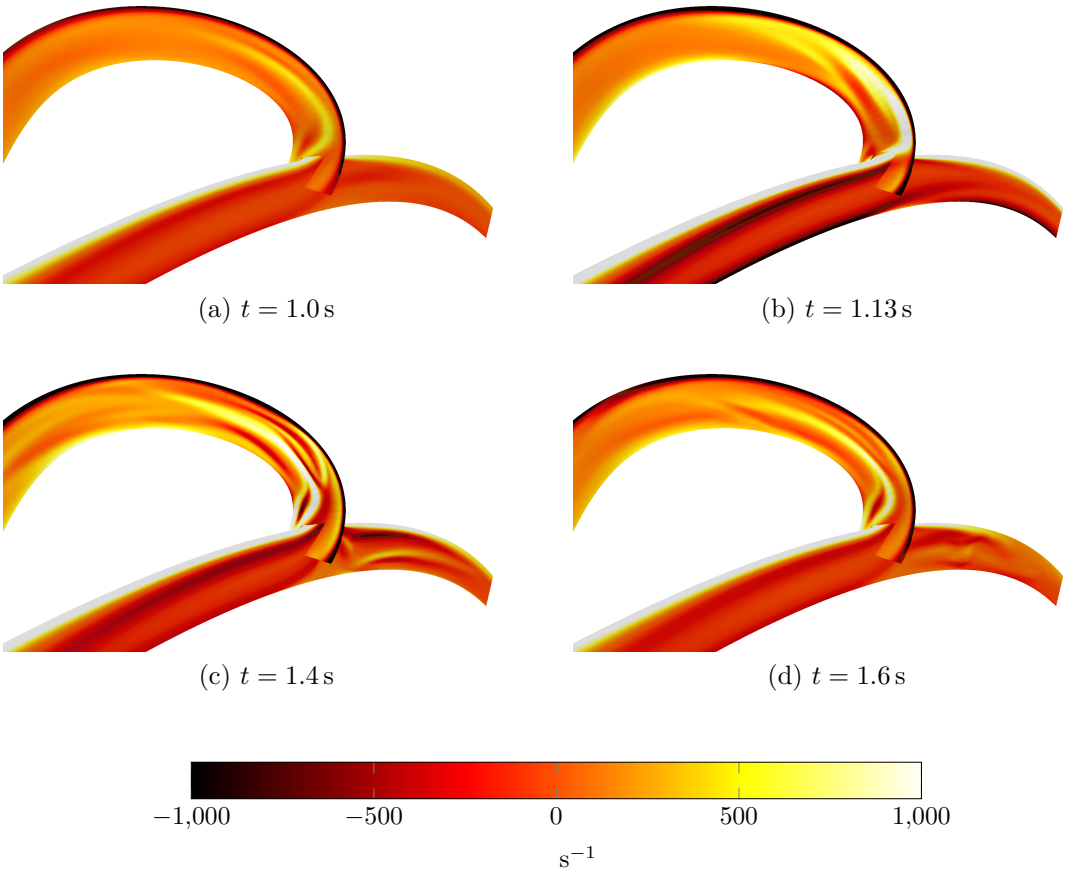


Figure 4.11: Snapshots of $\omega(\mathbf{x})$ on the arterial symmetry plane, and on a three-dimensional surface that tracks the venous centreline, at four points in the pulse cycle. It is clear that the region of re-circulation observed to the inside of the venous curvature, proximal to the anastomosis varies through the pulse cycle, together with the arterial distal flow. However, fine-scale separated vortical structures, associated with high-frequency flow unsteadiness, are absent.

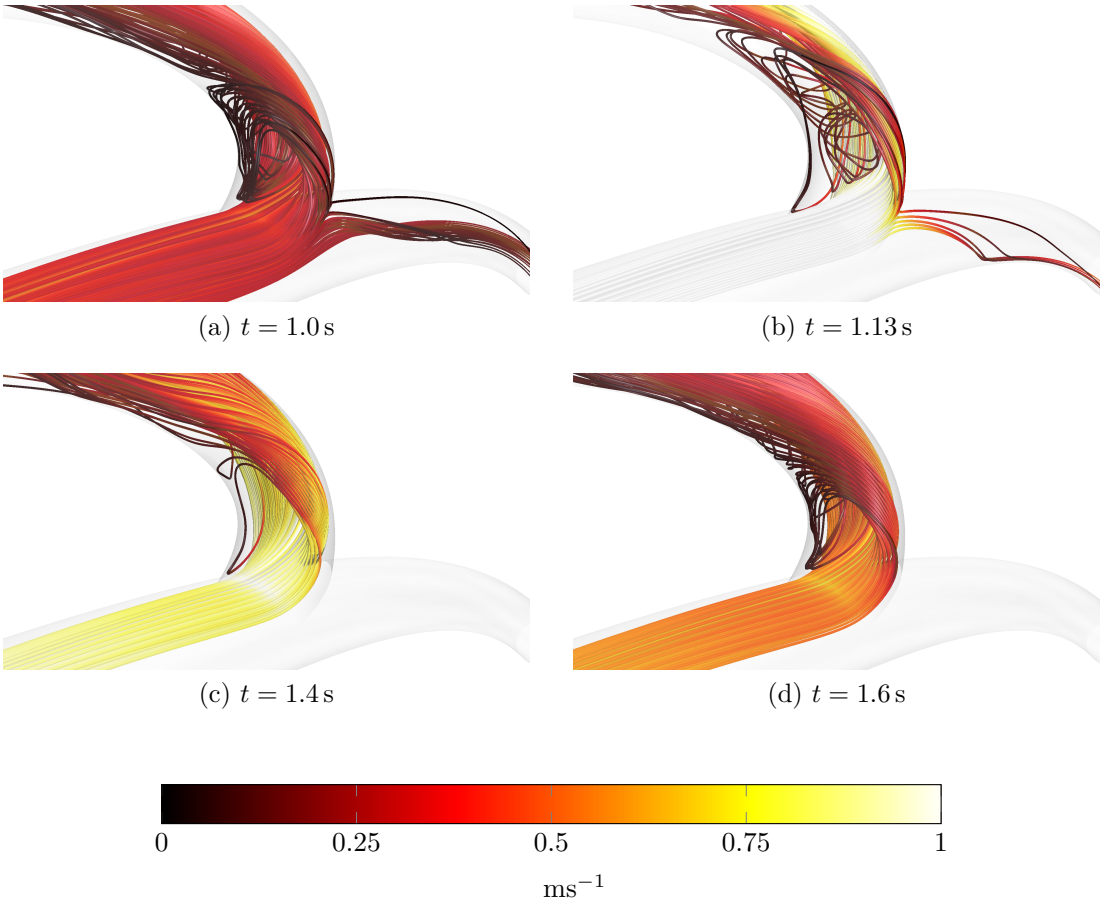


Figure 4.12: Streamlines, originating from the PAI, coloured by $u(\mathbf{x})$, at four points in the pulse cycle.

4.3.3.2 Dynamic Mode Decomposition

A quantitative assessment of unsteadiness was made via Dynamic Mode Decomposition (DMD) [84] of WSS fluctuations for $\boldsymbol{\tau}(\mathbf{x}, t) - \overline{\boldsymbol{\tau}}_t(\mathbf{x})$, where $\boldsymbol{\tau}(\mathbf{x}, t)$ is the space-time WSS vector field, and $\overline{\boldsymbol{\tau}}_t(\mathbf{x})$ is the temporal average of the space-time WSS vector field. Specifically, the DMD was calculated over the whole period respectively in the artery and in the vein, using 1250 temporal snapshots with a uniform spacing of 0.0008s. Fig. 4.13 shows the intensity γ. All significant energy is below 10Hz, and it is reasonable to attribute the majority of this low-frequency content to the pulse waveform. There is certainly no significant energy content

compared to those shown in the previous chapter, or to the results shown in other publications [1, 67, 70]. Additionaly, Fig. 4.14 shows the Power Spectral Density (PSD) of Q_{PAI} for comparison; it is reasonable to attribute the majority of the low-frequency content of Fig. 4.13 to the pulse waveform. Results clearly demonstrate that the optimal configuration suppresses high-frequency and potentially pathological flow unsteadiness in the AVF, as designed.

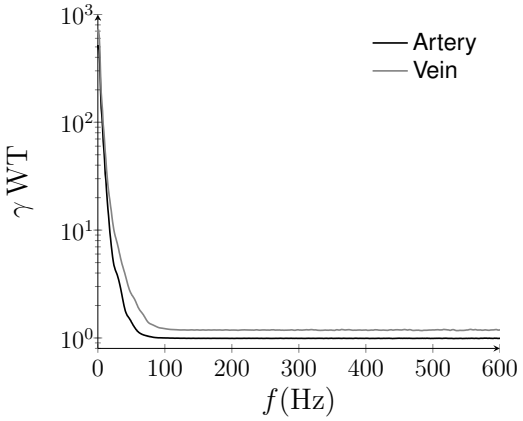


Figure 4.13: γ from DMD of $\boldsymbol{\tau}(\mathbf{x}, t) - \overline{\boldsymbol{\tau}}_t(\mathbf{x})$ in the artery (black line) and in the vein (light grey line).

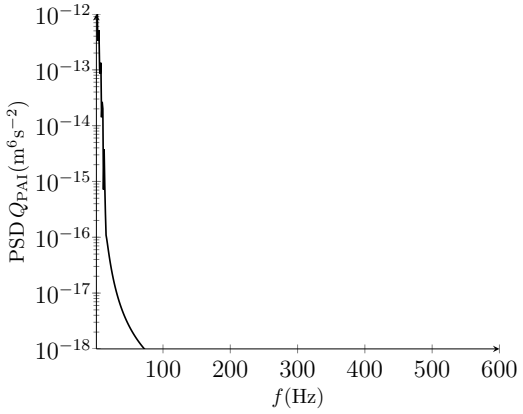


Figure 4.14: PSD of Q_{PAI} on a semi-log scale.

4.4 Conclusions

High-frequency flow unsteadiness has been associated with development of vascular pathology in AVF [36, 47, 48, 46]. In this chapter a MADS optimisation framework was employed with CFD simulations, to design a non-planar AVF configuration that suppresses high-frequency flow unsteadiness. Salient aspects of the proposed configuration include an anastomosis on the outer curvature of an arterial bend, and a looped non-planar venous section. It can also be noted that, qualitatively, the optimal non-planar configuration bears a resemblance to the 'curved' (as opposed to the 'straight') AVF configuration of Krishnamoorthy *et al.* [65], which exhibited increased patency rates in a pig model. Results constitute the first demonstration of how geometric manipulation can be used to suppress potentially pathological high-frequency flow unsteadiness in AVF.

Chapter 5

A Device for Shaping Arterio-Venous Fistulae

5.1 Introduction

The previous chapter presented a method to optimise AVF shape to suppress high-frequency unsteadiness. In this chapter the design and manufacture of a device for maintaining AVF connection in the optimal shape will be detailed, together with the results of a first non-recovery experiment in a pig.

5.2 Methods

5.2.1 Device Design

A device was designed as an extravascular element holding the AVF in the desired shape and which could be introduced by the surgeon after forming the vascular connection. The device was designed to be either right-handed, and hence inserted in the left carotid, or left-handed and hence inserted in the right carotid, mirroring the vein. Going forwards, it is envisaged that the device be fabricated

from a bio-compatible silicone such as Nusil Med-4830, or a bioresorbable hydrogel. However, for this non-recovery proof-of-concept the device was fabricated in Objet TangoBlackPlus FLX980 using a Connex 350 3D printer.

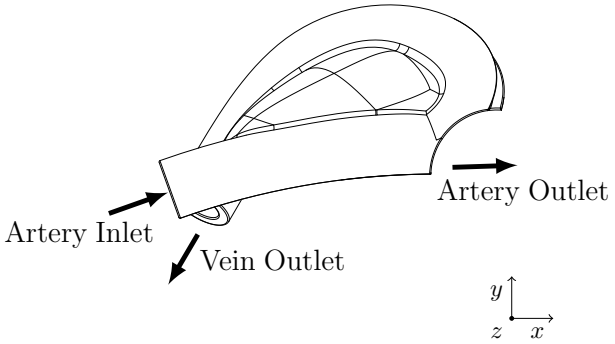
5.2.2 Device Prototyping and Manufacturing

A device was fabricated with a 5×10^{-3}mm internal guttering diameter, along with a counterpart device that was mirror-symmetric in the plane of the arterial curve (see Fig. 5.1)

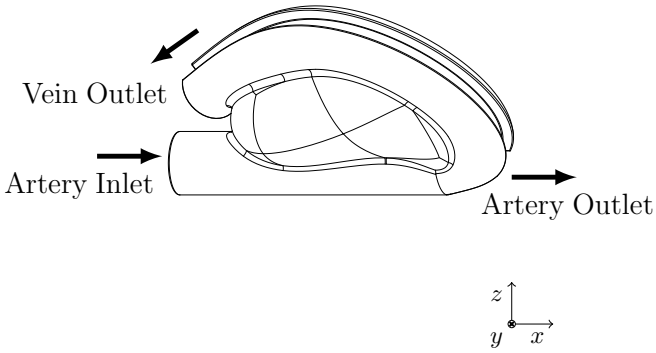
The device was designed in Autodesk Inventor, and had the subsequent characteristics:

- The venous and the arterial sections are semi-open guttering where the vessels could be introduced after the surgery.
- A solid non-planar element was introduced to connect the arterial slot and the venous slot, with the dual purpose of maintaining the device in the desired shape and giving structural reinforcement to the device itself.
- The results shown in the previous chapter suggested that the position of the distal part of the vein did not influence the outcome of the flow, therefore, the part holding the vein was made shorter compared to the optimal centerline of chapter 4, to facilitate the eventual positioning during surgery.

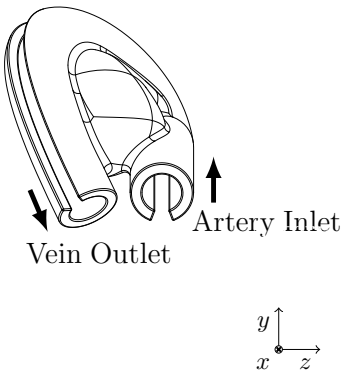
The final model is shown in Fig. 5.1, while the final 3d-printed object is shown in Fig. 5.2.



(a)



(b)



(c)

Figure 5.1: CAD model of a left-handed device for maintaining AVF in the optimal shape of chapter 4 (a) frontal view, (b) sagittal view, (c) transversal view.



(a)



(b)

Figure 5.2: 3d-printed devices for maintaining AVF in the optimal shape of chapter 4 (a) Left-handed device, (b) Right-handed device.

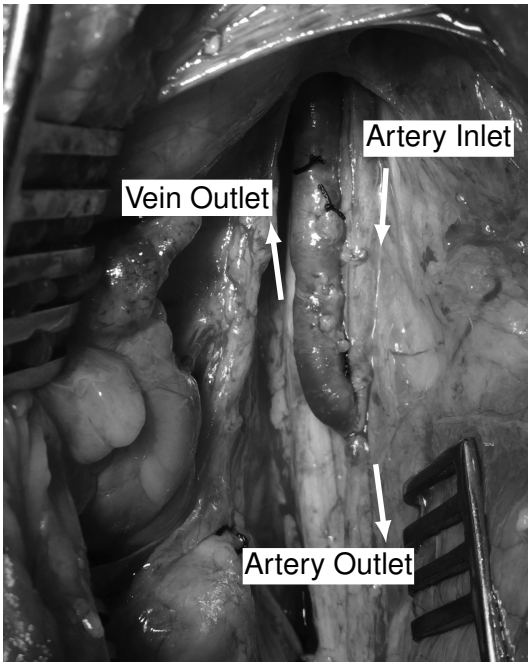
5.2.3 Porcine Model

A first non-recovery experiment was performed in a swine AVF model between the arterial carotid and the jugular vein, and is reported here as a proof of concept. Licences for this study were granted by the United Kingdom Home Office. The experiment took place at the Northwick Park Institute for Medical Research (Harrow, UK), and was performed by a trained surgeon. The author did not take part in the experiment.

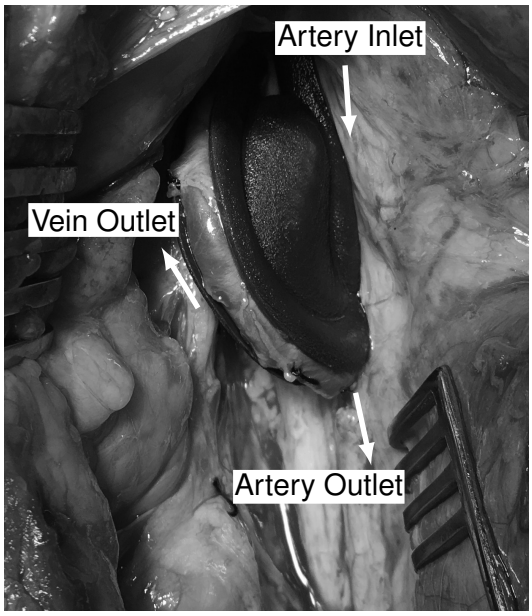
A mid-line incision was made in the neck and the jugular vein and carotid artery were exposed on both the left and right sides of the neck (with left-right

laterality defined in respect to the animal). Bilaterally, the jugular vein was mobilised and an anastomosis was made between the jugular vein and the common carotid artery to create an end-to-side AVF. Following creation of the AVF, the right-handed and left-handed devices were successfully implanted to shape the left-side and right-side AVF, respectively. Given the anatomical limitations of the surgical field a short ($\sim 5 \times 10^{-3}$m) portion of the device in the region of the distal venous outlet had to be trimmed on both sides to permit implantation.

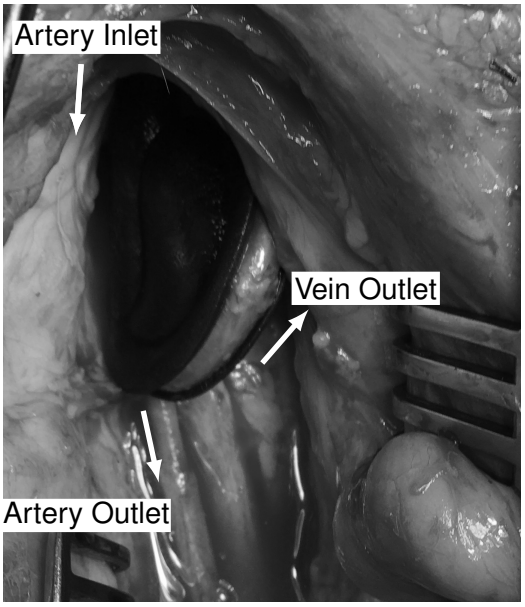
Fig. 5.3 shows the implanted device. In both cases the device held itself in place via the guttering, and visually formed the AVF into the desired configuration.



(a) Left Pre Device



(b) Left Post Device



(c) Right Post Device

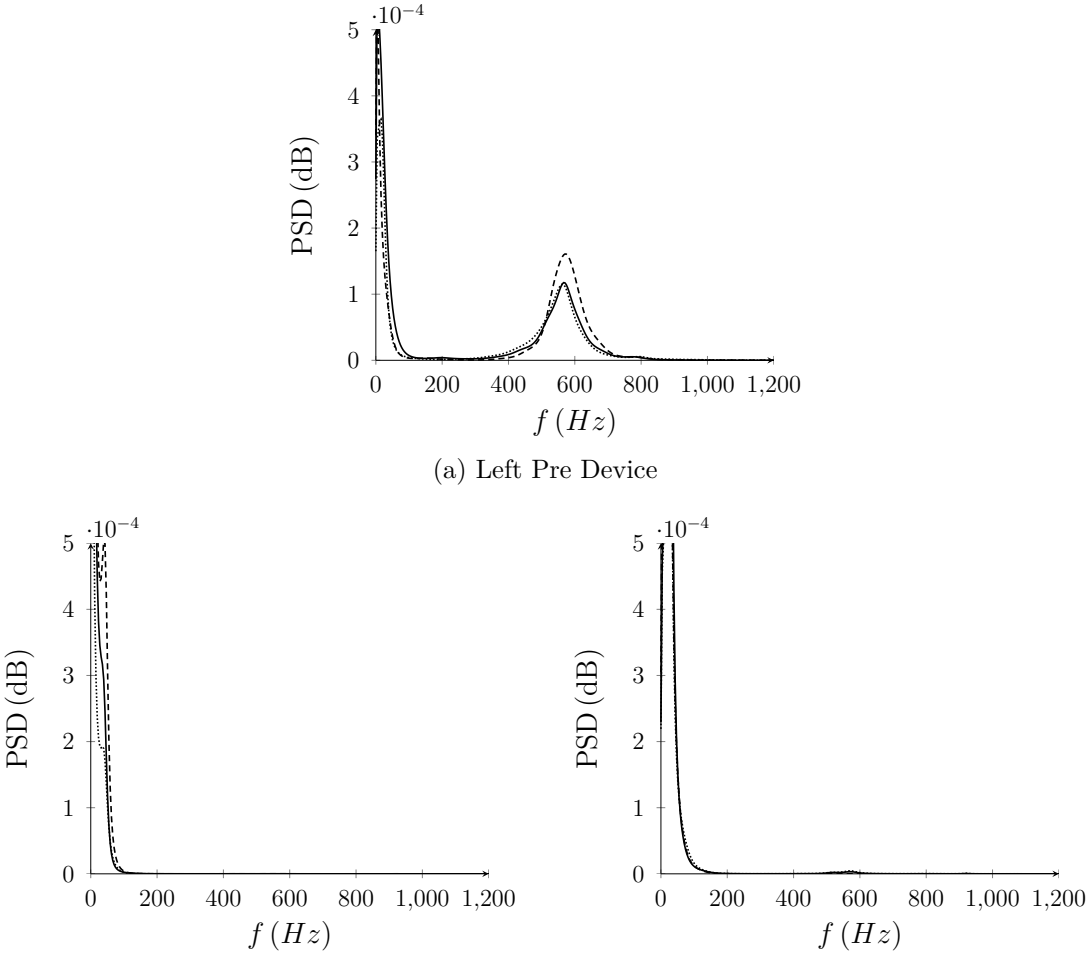
Figure 5.3: (a) Left Carotid-Jugular AVF without the device, (b) Left Carotid-Jugular AVF with device, (c) Right Carotid-Jugular AVF with device.

Ultrasound measurements were not available because the 3d-printed material is ultrasound-opaque. As a proxy for unsteadiness, digital stethoscope recordings

were made directly over the anastomosis both before (left-side AVF only) and after (left-side and right-side AVF) device implantation. Specifically, recordings were made using using an electronic 3M Littmann 3200 series stethoscope for approximately 20s with a sample rate of 4,000 Hz, and three independent recordings were made at each location.

5.3 Results

The stethoscope signal was recorded in the left side of the jugular vein before the implant and both in the left and in the right jugulars after the implant. Each recording was repeated 3 times. Fig. 5.4 show the PSD of the recorded signals (courtesy of Dr. Richard Corbett). The PSD was produced via a Burg Autoregressive Model of the stethoscope recordings from the left-side AVF before implanting the device, the left-side AVF after implanting the device, and the right-side AVF after implanting the device, respectively. All three recordings for the left-side configuration without the device exhibit a clear peak at $\sim$ 600Hz, which is eliminated from all three subsequent recordings after the device is implanted. This indicates that the device is acting to suppress high-frequency unsteady flow in the AVF. Moreover, the PSD spectra for the right-side AVF after implanting a device look visually similar to their left-side counterparts; without a significant peak at $\sim$ 600Hz. However, right-side AVF PSD spectra before implanting a device were not available for direct comparison.



(a) Left Pre Device

(b) Left Post Device

(c) Right Post Device

Figure 5.4: Power spectral density of the stethoscope recording before and after implanting the device, computed with the Burg filter (courtesy of Dr. Richard Corbett). It seems that the device successfully suppresses high frequency elements recorded before implantation.

5.4 Conclusions

In this chapter we have detailed the design and manufacture of a device for maintaining AVF connection in the optimal shape found in Chapter 4. Preliminary results of a first non-recovery experiment were also provided.

The results showed that the proposed device could be successfully implanted on two different locations and that the device held itself in place via the guttering,

and visually formed the AVF into the desired configuration. Results indicated also that the device could suppress high-frequency unsteady flow in an AVF. Future work will focus on manufacturing of the device in a bio-compatible material (e.g. implantable silicone or bioresorbable hydrogels), and to test the effect of the device on IH formation on multiple porcine models.

Chapter 6

Realistic Geometries and Flow Unsteadiness

6.1 Introduction

In the previous chapters the relationship between AVF geometries and high-frequency flow unsteadiness was studied by looking at realistic boundary conditions in semi-idealised AVF (Chapter 3), and studying the effect of venous geometric parameters in fully idealised geometries (Chapter 4).

In this chapter blood flow will be studied in patient-specific AVF. More specifically, geometric parameters will be identified and attempts will be made to associate them with enhancement/suppression of high-frequency unsteadiness. In the publication of Hammer *et al.* [125] it was shown that different segmentation methods can dramatically affect the CFD results in carotids reconstructed from 3D Ultrasound. This study will test the sensitivity of the simulated flow to different geometry reconstruction process. The relationship between AVF failure and flow unsteadiness will also be investigated.

6.2 Methods

6.2.1 Image Acquisition

All the geometries were reconstructed from patients that underwent native vascular access surgery in the upper limb for haemodialysis. The study received ethical approval (NRES 13/LO/0421) and all subjects gave informed consent. 67 patients were formally recruited, 63 of whom underwent MRI scanning on the day of surgery, henceforth referred as t_0. 3 of the obtained MRI scans were inadequate for segmentation. Among the 60 patients that could be segmented, 20 came back for a follow-up MRI scan between day 7 and day 14 after surgery, henceforth referred as t_1. Finally 49 patients received ultrasound measurements of blood flow at t_0.

Fig. 6.1 shows a schematic diagram of the observational cohort study (courtesy of Dr Richard Corbett).

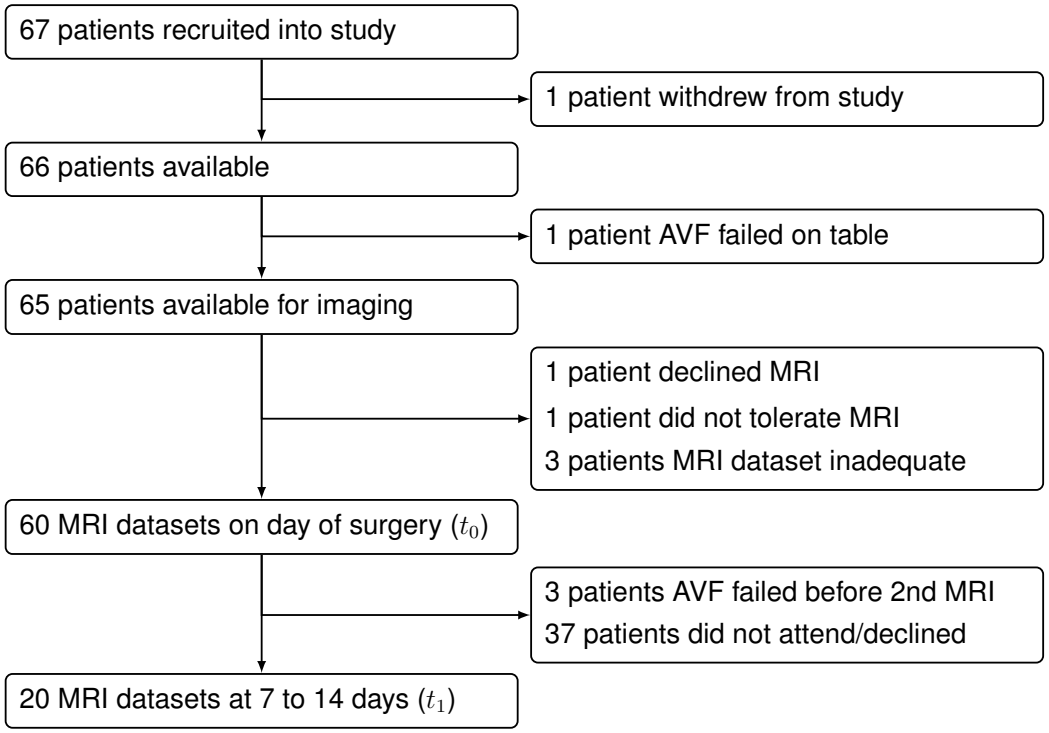


Figure 6.1: Schematic diagram of the observational cohort study (courtesy of Dr Richard Corbett).

During the study, different MRI sequences were used and different scanners. Specifically, the first 3 patients' geometries were reconstructed from an Inhanced Inflow Inversion Recovery (IFIR) sequence obtained on a GE 3T Discovery MR750 machine with echo time TE $= 2.5 \times 10^{-3}s$, repetition time TR $= 5.1 \times 10^{-3}$s and flip angle FA $= 50$ degrees. All the other patients were imaged on a Siemens 3T Verio scanner both with a Velocity Encoding (VENC) and with a Black Blood (BB) sequence. The VENC sequence was set with an encoding velocity of 50m/s, TE $= 5.7 \times 10^{-3}$s, TR $= 18.8 \times 10^{-3}$s and FA $= 20$ degrees, while the BB sequence had TE $= 10.0 \times 10^{-3}$s, TR $= 915 \times 10^{-3}$s and FA $= 180$ degrees.

6.2.2 Image Segmentation and Geometry Reconstruction

All the images obtained from the MRI scan were segmented in ITK Snap 3.4.0 [94], using a semi-automatic approach based on manual seeding of the vascular connections. The resulting surface meshes were then processed with semi-automatic Python scripts based on the VTK [126] and VMTK [95] libraries. Specifically, for each surface mesh, an ensemble of arterial and venous centerlines were first generated from the proximal artery inlet to the distal artery outlet or outlets (in some BCF cases) and from the proximal artery inlet to the distal venous outlet. The centerlines were then smoothed with the moving average filter implemented in VMTK. The moving average filter takes as an input the number of iterations and the smoothing factor. For all the patients the smoothing factor was set to 0.1 and the number of iterations was 100. The smoothed centerlines were re-interpolated such that each point had a fixed distance of 1×10^{-3}m from its neighbours. The centerlines were then divided into an arterial centerline(s) $\mathbf{x}_A$ and a venous centerline $\mathbf{x}_V$. The intersection point between $\mathbf{x}_A$ and $\mathbf{x}_V$ was set as origin $\mathbf{O}$ of the reference system. $\mathbf{O}$ divides the arterial centerline $\mathbf{x}_A$ into a proximal artery PA and distal artery segments DA.

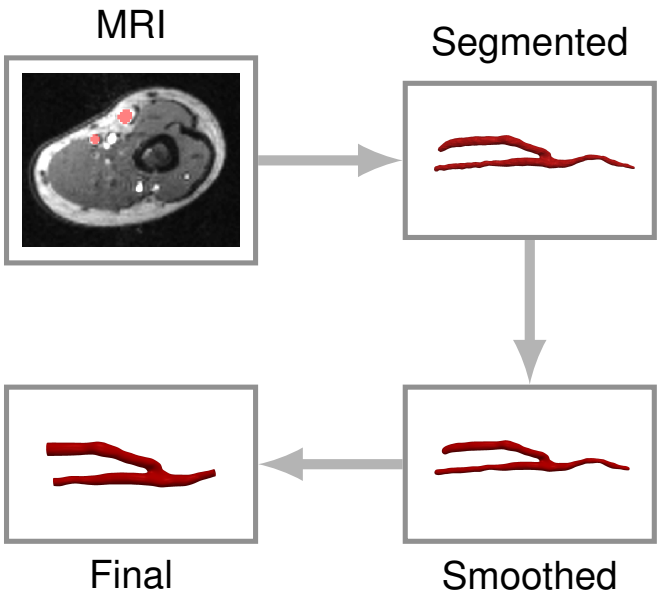
The Voronoi diagram of the lumen surface was used to obtain a smoother version of the segmented surface in a similar way as described in [127]. More specifically, the Voronoi diagram automatically obtained in VMTK was modified in order to reduce the number of points by 25%. The surfaces were then generated from the envelope of the spheres centered in each Voronoi point using the Marching Cubes algorithm.

The straight best-fitting line of PA passing through $\mathbf{O}$ was created for each smoothed geometry, and was aligned to the reference X-axis. The geometries were rotated such that the tangent to the first point of $\mathbf{x}_V$ was contained in the XY plane.

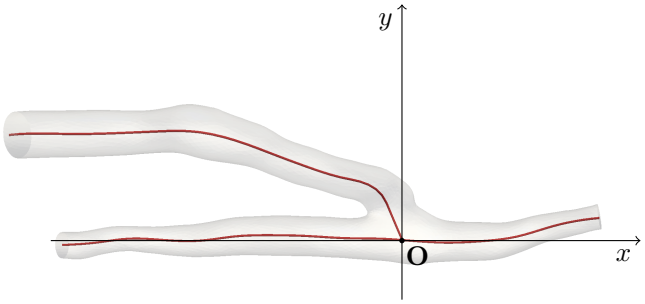
Finally, the proximal arterial diameter, D_{PA}, was defined as the mean di-

ameter of PA, with the diameter calculated from the cross-sectional maximum inscribed sphere radius, henceforth referred as to MISR, and was taken as the reference distance for each AVF. All the reconstructed AVF were cut such that $\mathbf{x}_A$ had a total arc length of $20\,D_{PA}$, ensuring, that PA measured $12\,D_{PA}$, while the vein was cut on the intersection point between $\mathbf{x}_V$ and the plane parallel to XZ centered at $[-12\,D_{PA}, 0, 0]$.

Fig. 6.2 shows a schematic version of the reconstruction process for a RCF.



(a)



(b)

Figure 6.2: (a) Reconstruction pipeline for a RCF. The image is initially segmented in ITK-Snap, smoothed in VMTK and finally aligned and cut. (b) the final reconstructed image with its centerlines in the rotated reference system.

A second geometry was generated for each patient through the lofting of circular sections with varying MISR as a radius over $\mathbf{x}_A$ and $\mathbf{x}_V$. The geometries were generated within the internal CAD of STAR-CCM+. The minimum distance between each section was set to $2D_{PA}$. This new set of geometries represent a smoother approximation of the reconstructed surfaces. These geometries will be

referred as the lofted surfaces $\mathbf{S}_L$, while the geometries reconstructed in VMTK will be referred as the realistic surfaces $\mathbf{S}_R$.

6.2.3 Geometric Characterisation

Each AVF was characterised by its centerlines and its cross-sectional MISR. Specifically, the centerlines were used to calculate:

- δ: the non-dimensional centerline curvature, defined as $\delta = \kappa D_{PA}$, with κ the centerline curvature,
- α: the angle formed between the tangent of $\mathbf{x}_V$ in $\mathbf{O}$ and the straight best fitting line of $\mathbf{x}_A$,
- χ: the centerline planarity index, defined as the mean distance of the centerline(s) points from their best fitting plane.

Taking a generic 3D parametric curve $\mathbf{x}(s)$, with s being the arc length of the curve, the tangent $\mathbf{T}(s)$, the normal $\mathbf{N}(s)$ and the binormal $\mathbf{B}(s)$ of a local Frenet reference system are defined as::

$$\begin{aligned} \mathbf{T}(s) &= \frac{\mathbf{x}'(s)}{||\mathbf{x}'(s)||}, \\ \mathbf{N}(s) &= \frac{\mathbf{x}''(s)}{||\mathbf{x}''(s)||}, \\ \mathbf{B}(s) &= \mathbf{T}(s) \times \mathbf{N}(s). \end{aligned} \tag{6.1}$$

These definitions of $\mathbf{T}(s)$ and $\mathbf{N}(s)$ are valid only where $||\mathbf{x}'(s)|| \neq 0$ and $||\mathbf{x}''(s)|| \neq 0$. The curvature $\kappa(s)$ is defined as the magnitude of the rate of change of $\mathbf{T}(s)$

$$\kappa(s) = \|\mathbf{T}'(\mathbf{s})\|, \tag{6.2}$$

with $\mathbf{N}(s) = \mathbf{T}'(s)/\kappa(s)$. The curvature κ for the generic curve $\mathbf{x}(q)$, with q a generic parametrisation [128], can be rewritten as:

$$\kappa = \frac{\|\mathbf{x}'(q) \times \mathbf{x}''(q)\|}{\|\mathbf{x}'(q)\|^3}. \tag{6.3}$$

The vascular curvature κ will depend on the approximation of the first and the second derivatives of the curve $\mathbf{x}$. However, the extracted centrelines can be affected by noise. κ was therefore estimated with the method proposed by Lewiner *et al.* in [129], in which the centrelines are locally approximated with a third order polynomial calculated through a weighted least square fitting. The weights used for the least square fitting are of the form $w_n = c_1 \exp(-c_2 s_n^{c_3})$, with $c_1 = 1$, $c_2 = 0.05$ and $c_3 = 2$. Fig. 6.3 (a) shows the resulting radius of curvature $1/\kappa$ for one point of the RCF of Fig. 6.2.

The angle α was estimated directly from the normalised tangent of $\mathbf{x}_V$ at $\mathbf{O}$, which can be rewritten in the form $[\cos(\theta_{V0})\sin(\phi_{V0}), \sin(\theta_{V0})\sin(\phi_{V0}), \cos(\phi_{V0})]$. By definition, the first point of the vein is in the semi-positive region of the XY plane, which means $\phi_{V0} = 90^o$, while θ_{V0} is the angle formed between the positive X direction and the venous centerline, and the bifurcation angle α is defined as $\alpha = 180^o - \theta_{V0}$. Fig. 6.3 (b) shows the angle α for the RCF of Fig. 6.2.

Finally, a novel measurement of the vascular planarity χ is introduced. Specifically, the best fitting plane based on the least square method was calculated for $\mathbf{x}_A \cup \mathbf{x}_V$, for $\mathbf{x}_A$ only, and for $\mathbf{x}_V$ only. Any plane having normal $[n_1, n_2, n_3]$ and passing through the generic point $[x_0, y_0, z_0]$ can be identified by the equation

$$n_1 x + n_2 y + n_3 z + d = 0, \tag{6.4}$$

with $d = -n_1 x_0 - n_2 y_0 - n_3 z_0$ The best fit plane of the curve $\mathbf{x}$ is defined as a plane passing through the barycenter of the curve $[x_0, y_0, z_0] = \frac{1}{N}\sum_n \mathbf{p}_n$ where N

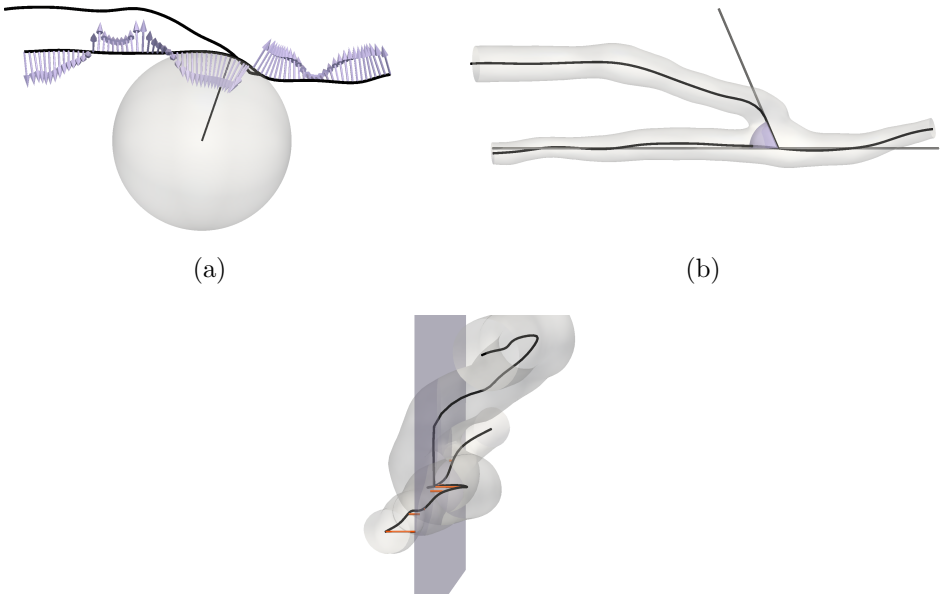
is the total number of points of the curve, and minimising the equation:

$$E_\chi\left(n_1, n_2, n_3\right) = \sum_n \left(n_1 x_{\mathbf{p}_n} + n_2 y_{\mathbf{p}_n} + n_3 z_{\mathbf{p}_n} + d\right)^2 . \tag{6.5}$$

The mean distance from each best fitting plane to the corresponding centerline(s) was then calculated and non-dimensionalised by D_{PA}

$$\chi_{\mathbf{x}} = \frac{1}{N D_{PA}} \sum_n \left| n_1 x_{\mathbf{p}_n} + n_2 y_{\mathbf{p}_n} + n_3 z_{\mathbf{p}_n} + d \right| . \tag{6.6}$$

If a vessel or the whole AVF was planar, then the corresponding value of $\chi_{\mathbf{x}}$ should be close to 0. Fig. 6.3 (c) shows the best fit plane of the arterial centerline for the RCF of Fig. 6.2 and the distance vectors from the points of $\mathbf{x}_A$



(a) (b)

(c)

Figure 6.3: (a) radius of curvature of a generic point in $\mathbf{x}_A$, (b) angle α, (c) best fitting plane (in gray) of $\mathbf{x}_A$ and the distance vectors (in orange) from the points of $\mathbf{x}_A$ (in black). All the figures are based on the centerline of the RCF in Fig. 6.2.

6.2.4 Ultrasound Measurements

Ultrasound (US) flow measurements were available for 49 patients. Each patient-specific waveform was computed in Matlab using a method similar to the one described by Holdsworth *et al.* in [130]. Specifically, the US measured section average velocity and vessel dimensions (maximum and minimum inscribed radius) for each patient for at least 3 cardiac cycles. The section-averaged flow Q was calculated as the product of the section-averaged velocity times the area of an ellipse having as dimensions the two vessel dimensions. Each waveform was manually divided by its period, and a patient-specific waveform was computed averaging the values of 8 fixed time-points: the systolic flow, the minimum flow before systole, two points corresponding to the intercept with the 75% of the systolic amplitude, the point with maximum flow variation in time, and 3 equidistant diastolic points, including the point at the end of the period. The resulting averaged points were finally interpolated with a piecewise cubic hermitian polynomial. The interpolation generated three waveforms for each patient, Q_a, Q_v and Q_d, where Q_a is the average waveform at the proximal artery, Q_v the average waveform inside the vein, and Q_d, the average waveform in the artery. It was assumed that each patient-specific waveform had the maximum flow at systole.

In order to obtain waveforms with sensible flow splits, and to filter the possible error derived by measuring the flow in the three locations at three different times, the final patient-specific waveworms Q_{PA}, Q_{DA}, Q_V were defined as:

$$\begin{aligned} Q_{PA} &= \frac{1}{2}(Q_a + (Q_d + Q_v)), \\ Q_{DA} &= Q_{PA}\frac{Q_d}{Q_d + Q_v}, \\ Q_V &= Q_{PA}\frac{Q_v}{Q_d + Q_v}. \end{aligned} \tag{6.7}$$

6.2.5 Computational Fluid Dynamics Simulations

One of the aims of the chapter is to understand how sensitive the simulated flow is to relatively small differences in the geometry reconstruction process, and if there is a possible correlation between geometry-induced flow instability and geometric parameters.

In chapter 4 the function Ψ was introduced to identify possible steady idealised AVF in an optimisation framework. The main assumption was that, under steady boundary conditions, the steady solver and the unsteady solver converged to the same solution only if the geometry did not induce unsteady flow patterns. Ψ estimates the difference between the two solutions, therefore when Ψ has low values, it can be assumed that the solution is steady. However the interpretation of high values of Ψ is unclear, because it only quantifies how much the two solvers diverge, and not how unsteady the flow is. To identify possibly patient-specific steady geometries, 4 CFD simulations were run for each patient with steady boundary conditions. More specifically, 2 simulations were run in the reconstructed geometries $\mathbf{S}_R$, and 2 in the lofted geometries $\mathbf{S}_L$. A first set of simulations (2 per patient) was run with the measured systolic flow, while a second set of simulations (2 per patient) was run with patient-averaged boundary conditions. The results from the first set were analysed to find an appropriate threshold for the function Ψ which was then used to identify steady geometries. More specifically, the correlation between Ψ and frequencies obtained through DMD analysis was studied to identify a sensible threshold below which a simulation could be considered steady. In the first set of simulations was also studied the sensitivity of the flow to the geometric reconstruction method. The results obtained by both the sets of simulations were finally studied to analyse if there was a possible correlation between flow stability and geometric parameters. Fig. 6.4 shows the flow chart for the proposed simulations analysis.

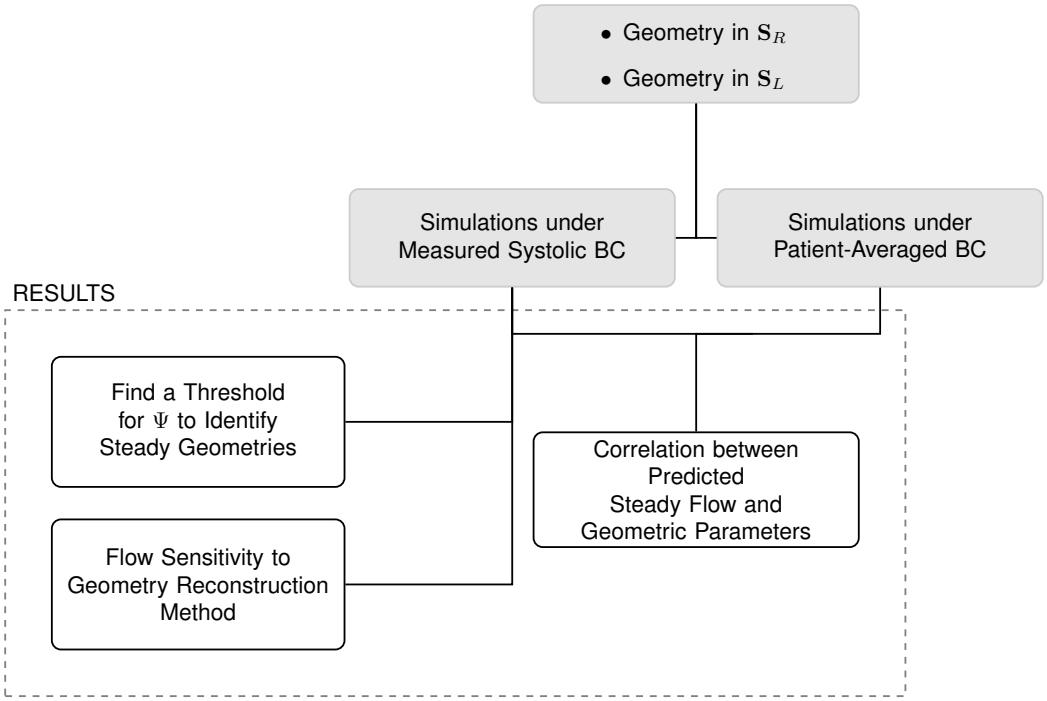


Figure 6.4: Flow Chart summarising the simulations run for each patient and the results analysis.

6.2.5.1 Governing Equations

Following Sec. 4, a steady state solution to Eq. 3.1 and Eq. 4.9 was obtained. For each patient the viscosity μ was measured with the method proposed by Rosenson *et al.* in [131]. The resulting steady-state solution was then used as the initial condition for Eq. 3.1 and the unsteady incompressible Navier-Stokes equations 3.2 with the same parameter values and boundary conditions employed for the steady-state problem.

6.2.5.2 Boundary Conditions

Two simulations were run with different steady boundary conditions for each geometric set $\mathbf{S}_R$ and $\mathbf{S}_L$. More specifically:

- a first set of simulations had as inflow the measured systolic proximal artery flow, henceforth referred to as $\max_t Q_{PA}$, and the measured systolic venous

outflow, henceforth referred to as $\max_t Q_V$, at the venous outlet. When there were no US measurements for the patient, the patient-averaged systolic flows calculated over AVFs having the same location as the AVF under consideration was used.

- a second set of simulations imposed an inflow having a corresponding Reynolds number of 800 for BCF and BBF, and a corresponding Reynolds number of 600 for the RCF. The proximal Reynolds number was calculated using D_{PA} a characteristic diameter, and the measured patient-specific viscosity. For the outflow boundary condition an 80:20 flow split was imposed for all configurations. The average boundary conditions were based on the average of US measurements and were in line with data from the literature [122, 123].

6.2.5.3 Computational Method

Star-CCM+ v9.06.9 (CD-Adapco, Melville, NY USA) was used to solve Eq. 3.1 with either Eq. 4.9 or Eq. 3.2. Specifically, 1500 iterations of the segregated steady-state solver were used to solve Eq. 3.1 with Eq. 4.9, and the segregated implicit unsteady solver with a time-step of $t_S = t_C/50$ was used to solve 3.1 with Eq. 3.2, where t_C indicates the proximal characteristic time $t_C = (\pi D_{PA}^3)/(4\overline{Q}_{PA})$. Polyhedral unstructured volume meshes, with a prismatic boundary layer adjacent to the arterial wall were constructed for each geometry. Specifically, the polyhedral elements had an average size of $0.035D_{PA}$. The prismatic boundary layer was 14 elements thick, with the first element having a thickness of less than $0.031D_{PA}$, and having a growing ratio of 1.08. Each mesh had approximately 2M of elements. Each patient-specific simulation with realistic boundary conditions was run for 15 characteristic times t_C, and the last $10t_C$ were exported for calculating Ψ and the DMD intensity. The second set of simulations, were run for $10t_C$, exporting only the last $5t_C$ for calculating Ψ.

6.3 Results I: Geometries and Clinical Measurements

6.3.1 Geometry Reconstruction

Figs. 6.5, 6.6 and 6.7 show the 60 geometries obtained from scans at t_0 divided into BCF, RCF and BBF. The majority of the segmented images were reconstructed from the VENC sequence. 39 of the obtained AVF were BCF, 18 RCF and 3 BBF. 20 out of the 60 segmented AVF failed to mature at 6 to 8 weeks, resulting in a failure rate of 33.3%, in line with previous studies [21]. More specifically, 8/39 (10.5%) BCF, 12/18 (66.7%) RCF and 0/3 (0%) BBF failed to mature at 6 to 8 weeks. The failed AVF are highlighted in light pink in Figs. 6.5, 6.6 and 6.7.



Figure 6.5: Frontal view of the reconstructed AVF grouped by type (BCF, RCF and BBF). The AVF that did not mature are highlighted in light pink.

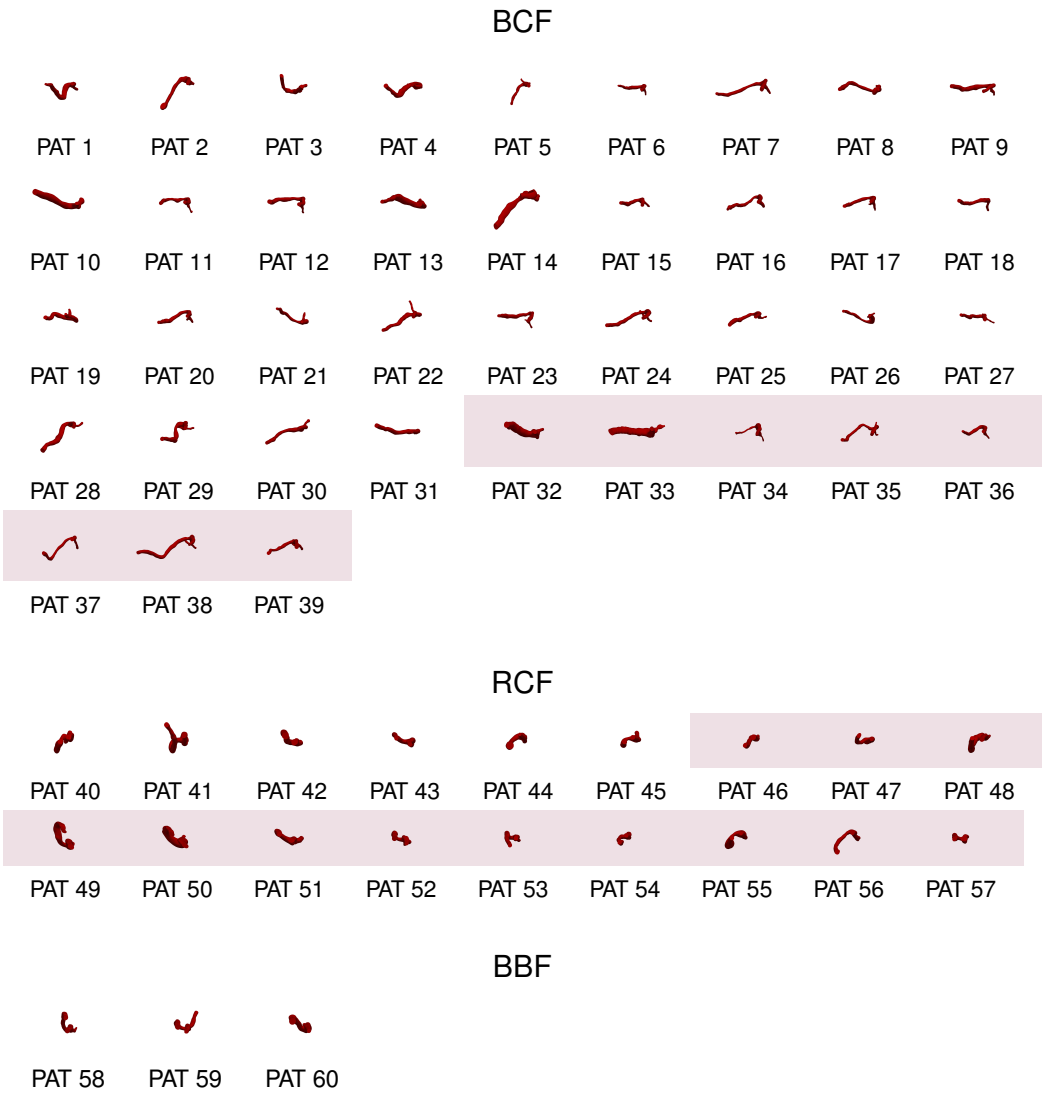


Figure 6.6: Transversal view of the reconstructed AVF grouped by type (BCF, RCF and BBF). The AVF that did not mature are highlighted in light pink.

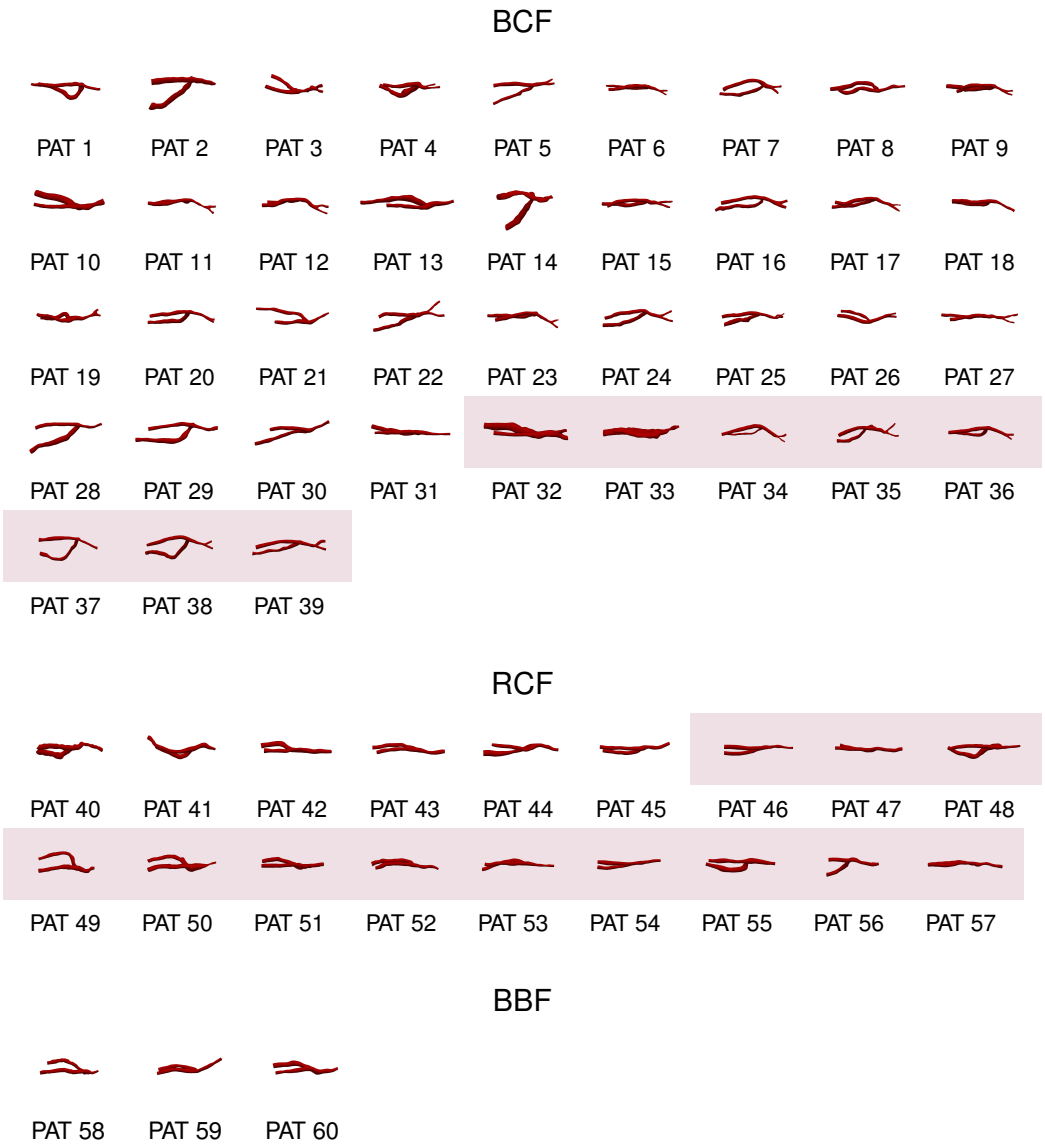


Figure 6.7: Sagittal view of the reconstructed AVF grouped by type (BCF, RCF and BBF). The AVF that did not mature are highlighted in light pink.

6.3.2 Anatomic Variability

Table 6.1 reports the mean values and the standard deviation of the geometric parameters introduced in Section 6.2.3 for the two AVF locations: upper arm AVF, i.e. BCF and BBF together, henceforth referred to as BCF∪BBF, and lower arm AVF i.e. RCF at t_0. The correlation between AVF location and

geometric parameters values has been assessed using the software R [132] with the two sided unpaired t-test, and the resulting 95% confidence interval of the group mean difference with the relative p-value are also reported in Tab. 6.1.

	BCF∪BBF	RCF	95% Δ CI	p-value	
D_{PA}(mm)	5.54 ± 1.19	4.38 ± 0.75	$[\ 0.65, 1.68\ ]$	3.27×10^{-5}	***
D_{DA}(mm)	3.98 ± 0.70	3.83 ± 0.80	$[-0.29, 0.60\ ]$	4.85×10^{-1}	
D_V(mm)	5.57 ± 1.00	4.52 ± 1.02	$[\ 0.47, 1.63\ ]$	8.55×10^{-4}	***
D_V/D_{PA}	1.04 ± 0.25	1.03 ± 0.14	$[-0.09, 0.11\ ]$	8.43×10^{-1}	
α(deg)	77.92 ± 14.56	61.51 ± 14.64	$[\ 8.02, 24.80\ ]$	3.65×10^{-4}	***
$\delta_A(D_{PA}^{-1})$	0.14 ± 0.041	0.11 ± 0.03	$[\ 0.02, 0.06\ ]$	2.39×10^{-4}	***
$\delta_V(D_{PA}^{-1})$	0.16 ± 0.04	0.18 ± 0.05	$[-0.05, 0.01\ ]$	1.05×10^{-1}	
$\chi_A(D_{PA})$	0.23 ± 0.12	0.12 ± 0.04	$[\ 0.07, 0.15\ ]$	1.34×10^{-6}	***
$\chi_V(D_{PA})$	0.17 ± 0.10	0.18 ± 0.12	$[-0.08, 0.06\ ]$	7.34×10^{-1}	
$\chi(D_{PA})$	0.59 ± 0.34	0.34 ± 0.18	$[\ 0.11, 0.38\ ]$	5.20×10^{-4}	***

Table 6.1: Mean value and standard deviation of the geometric parameters value for the AVF in the upper arm (BCF∪BBF) and in the lower arm (RCF). The correlation between AVF location and the geometric parameters has been assessed with the two sided unpaired t-test, and the resulting 95% confidence interval of the group mean difference with the relative p-value are reported. * is for p-value < 0.05,** is for p-value < 0.01,*** is for p-value < 0.001.

The results suggest that there is a strong correlation between AVF location and:

- arterial proximal diameter D_{PA},
- venous diameter D_V,
- anastomosis angle α,
- mean non-dimensional arterial curvature δ_A,
- mean non-dimensional arterial planarity index χ_A,

- mean non-dimensional AVF planarity index χ.

More specifically, it seems that upper arm AVFs have a bigger arterial proximal diameter and venous diameter and a wider anastomosis angle; it seems also that upper arm AVFs have more curved and less planar arterial sections than AVFs formed in the lower arm, and that generally an upper arm AVF is less planar than a RCF. Results also suggest that the diameter ratio between the vein and the proximal artery is very close to 1 for all the types of AVFs.

The findings on D_{PA}, D_V and their diameter ratio are in line with previous studies [122, 97]. Smaller anastomotic angles have been observed in RCFs compared to BCFs by Sadaghianloo *et al.* in [133]. However, in [133] the anastomotic angle was measured only intra-operatively.

The relationship between AVF maturation and geometric parameters at t_0 has also been studied. The results suggested that there is a correlation between AVF maturation and:

- D_V (p-value 8.8×10^{-3}),
- α (p-value 1.16×10^{-2}),
- δ_A (p-value 4.9×10^{-4}),
- χ_A (p-value 3.75×10^{-3}).

The parameters values and their box plots are shown in Fig. 6.8. It is important to notice that there is a greater number of RCFs that did not mature compared to upper arm AVFs, and this could have affected the results.

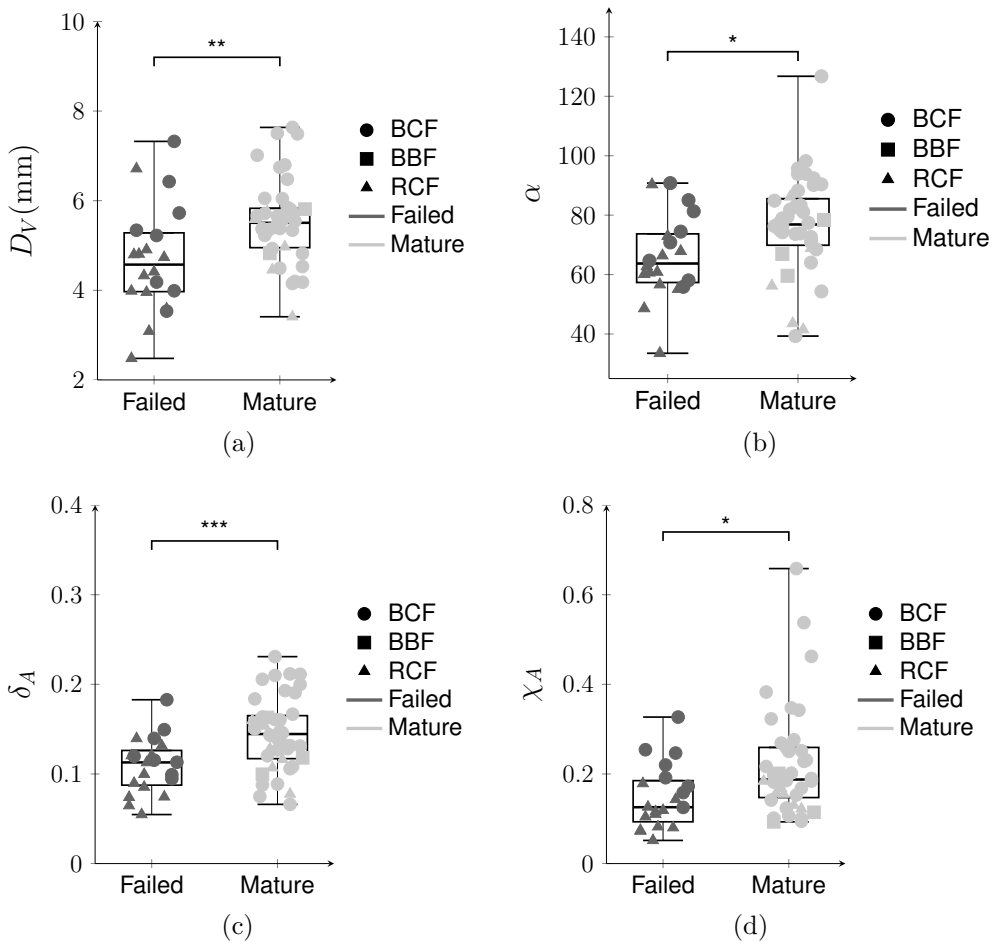


Figure 6.8: (a) venous diameter D_V (b) anastomosis angle α (c) mean non-dimensional arterial curvature δ_A (d) mean non-dimensional arterial planarity index χ_A seems all to be correlated with AVF failure. It is important to notice, however, that there is a greater number of RCFs that did not mature compared to upper arm AVFs, and it could have affected the results. * is for p-value < 0.05,** is for p-value < 0.01,*** is for p-value < 0.001.

6.3.2.1 Anatomic Variability and Arterio-Venous Fistulae Maturation

Fig. 6.9 shows the 20 reconstructed MRI at t_1 compared to the images reconstructed at t_0. The images at t_1 were co-registered to their equivalent at t_0 in VMTK, after being processed with the same method. From Fig. 6.9 it is clear that during maturation most AVFs kept the main features they had at t_0. How-

ever, small local changes are present in each geometry. There are no evident differences between mature AVFs and non-mature AVF at t_1.

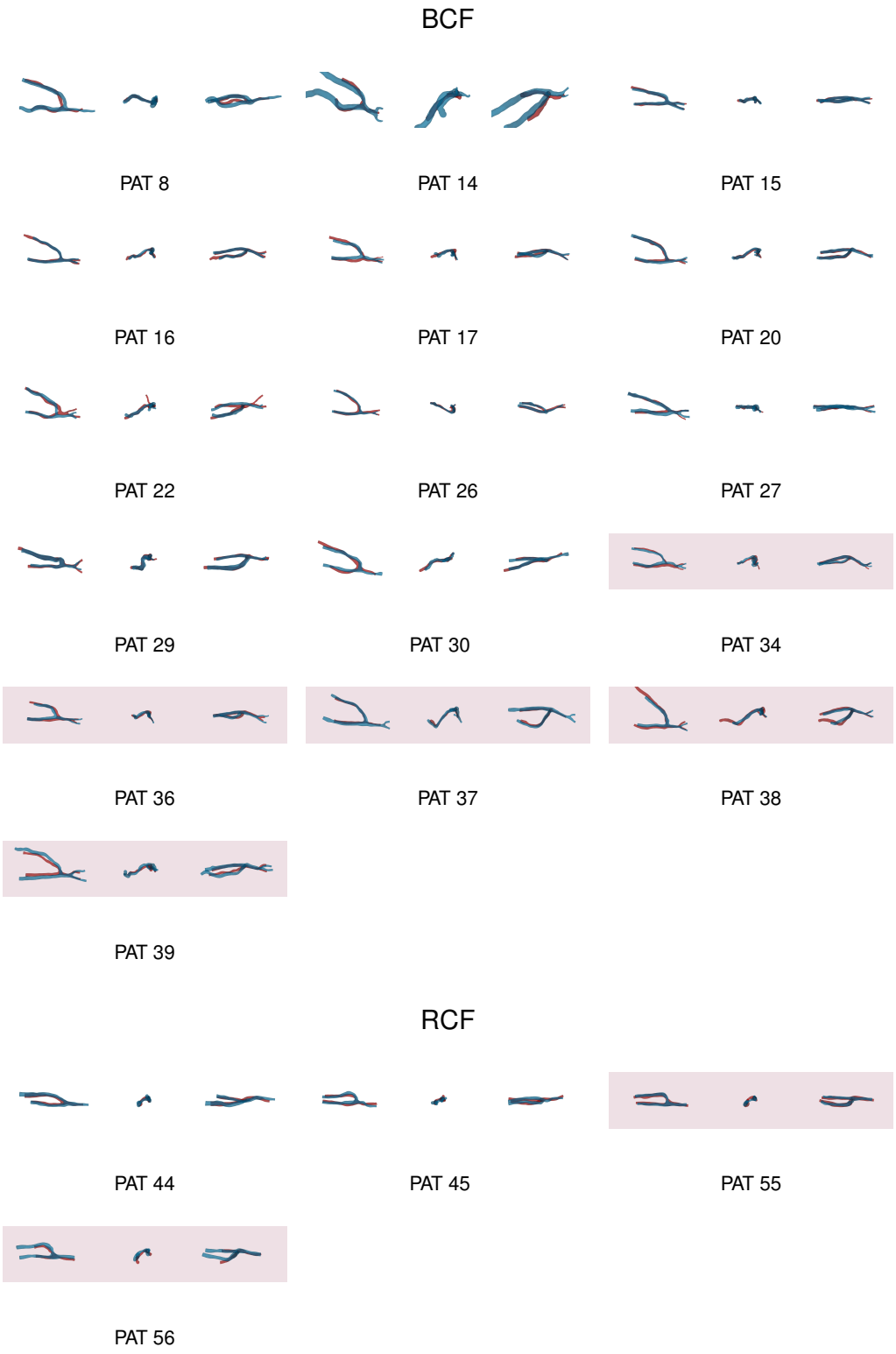


Figure 6.9: Frontal, Transversal and Sagittal views of the patients that underwent the second MRI, at t_1 (in blue) and at t_0 (in red). The images have been co-registered in VMTK. The AVF that did not mature are underlined in light pink. Most of the AVF seem to preserve their main geometric features during the first weeks since creation.

The differences between geometries at t_0 and t_1 were quantified by comparing the geometric parameters. The percentage differences of these quantities are shown in Tab. 6.2. The statistical significance of the parameters difference between t_0 and t_1 was tested with the two sided paired t-test implemented in R [132], and the resulting 95% confidence interval of the group mean difference with the relative p-value are also reported in Tab. 6.2.

	t_0	t_1	Δ	95% Δ CI	p-value	
D_{PA}	5.25 ± 1.09	5.76 ± 1.19	0.50 ± 1.13	$[-0.03, 1.03]$	6.45×10^{-2}	
D_{DA}	4.00 ± 0.81	4.26 ± 0.63	0.26 ± 0.86	$[-0.14, 0.66]$	1.88×10^{-1}	
D_V	4.96 ± 0.85	5.67 ± 0.98	0.72 ± 0.88	$[\ 0.31, 1.13]$	1.58×10^{-3}	**
α	77.82 ± 17.23	80.37 ± 14.30	2.55 ± 15.45	$[-4.67, 9.79]$	4.68×10^{-1}	
δ_A	0.10 ± 0.05	0.09 ± 0.07	0.00 ± 0.04	$[-0.02, 0.01]$	5.78×10^{-1}	
δ_V	0.16 ± 0.03	0.18 ± 0.04	0.02 ± 0.04	$[\ 0.00, 0.05]$	2.19×10^{-2}	*
χ_A	0.20 ± 0.09	0.21 ± 0.12	0.01 ± 0.09	$[-0.04, 0.05]$	7.71×10^{-1}	
χ_V	0.15 ± 0.07	0.20 ± 0.11	0.05 ± 0.12	$[-0.26, -0.08]$	9.11×10^{-2}	
χ	0.67 ± 0.39	0.61 ± 0.37	-0.062 ± 0.15	$[-0.13, 0.04]$	7.67×10^{-2}	

Table 6.2: Mean value and standard deviation of the parameters at t_0 and t_1 and their difference Δ for the patients that have a second MRI. The correlation between the parameters at t_0 and at t_1 has been assessed with the two sided paired t-test, and the resulting 95% confidence interval of the group mean difference with the relative p-value are also reported. * is for p-value < 0.05,** is for p-value < 0.01.

As expected from 6.9 the changes between t_0 and t_1 are more dependent on the single patient and, apart the venous diameter, there is not a statistically significant difference between the two groups.

The percentage increase of D_V has an inter-quartile range between 2.6% and 26%. Previous publications [20, 122] have found an increment in the vein lumen up to 180% in the first 12 weeks of maturation.

Finally, it is worth to notice that some patients have high variations in one

or more parameters between t_0 and t_1. It is difficult to assess whether some of these variations reflect effective geometrical differences during AVF maturation, or result from uncertainty in the acquisition/reconstruction method.

6.3.3 Ultrasound Measurements

Values for the US interpolated proximal flows Q_{PA}, the resulting flow splits, and proximal diameters D_{PA-US} are reported in Tab. 6.3

	BCF∪BBF	RCF
TA-Q_{PA} (ml/min)	352.0 ± 230.2	169.4 ± 52.7
$\max_t Q_{PA}$ (ml/min)	528.3 ± 279.8	227.7 ± 70.9
$\min_t Q_{PA}$ (ml/min)	263.2 ± 179.0	95.8 ± 42.6
TA-(Q_V/Q_{PA})	0.84 ± 0.13	0.84 ± 0.08
$\max_t Q_V / \max_t Q_{PA}$	0.69 ± 0.19	0.80 ± 0.07
$D_{PA\text{-}US}$(mm)	4.8 ± 0.9	3.0 ± 0.6

Table 6.3: US measurements at t_0, with median and standard deviation for the time-averaged proximal artery flow TA-Q_{PA}, the maximum proximal artery flow $\max_t Q_{PA}$, the minimum proximal artery flow $\min_t Q_{PA}$, the time-averaged flow split between the vein and the proximal artery TA-(Q_V/QPA), the flow-split at systole $\max_t Q_V / \max_t Q_{PA}$, and the US measured arterial proximal diameter $D_{PA\text{-}US}$.

Tab. 6.3 shows that there is high inter-patient flow variation. It also shows that the arterial proximal diameter measured with US is smaller than the diameter resulting from MRI reconstruction, especially in RCF. This is in line with previous findings [134]. However, it is unclear if the difference is mainly because the MRI tends to overestimate the vessel lumen, including the wall thickness, or if it is because the US measurements tend to under-estimate the vessel lumen, possibly affecting the estimated flows. Furthermore, it is worth noticing that in 9/18 RCF Q_v seemed greater than Q_a at t_0, suggesting the presence of retrograde flow. On the other hand, positive flow was also registered for Q_d, suggesting that the total

flow changed between the 3 different measurements and the final averaged flows Q_{PA}, Q_{DA} and Q_V do not present retrograde flow for any patient. No retrograde flow was seen in any measurement for BCFs.

6.4 Results II: Computational Fluid Dynamics Simulations

6.4.1 Blood Flow under Patient-Specific Boundary Conditions

6.4.1.1 Blood Flow Unsteadiness

DMD intensity γ was calculated for the WSS field for each simulation under systolic boundary conditions in $\mathbf{S}_R$ and in $\mathbf{S}_L$. The intensity γ was rescaled by the space-time averaged WSS $\overline{\boldsymbol{\tau}}_{tS}$, $\widetilde{\gamma} = \gamma/\overline{\boldsymbol{\tau}}_{tS}$. The maximum WSS oscillation frequency f_M was defined as the maximum frequency having $\widetilde{\gamma} > 1$ averaged between the two simulations (in $\mathbf{S}_R$ and in $\mathbf{S}_L$ respectively). Fig. 6.10 shows f_M against Ψ averaged between $\mathbf{S}_R$ and in $\mathbf{S}_L$.

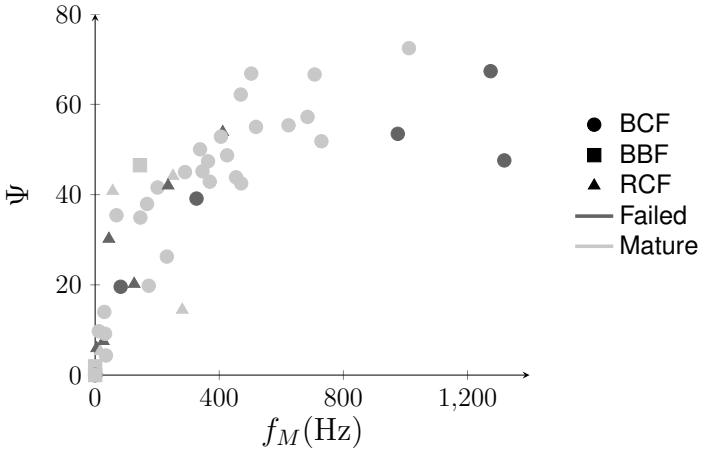


Figure 6.10: f_M calculated from the DMD intensity against Ψ. The values are obtained by averaging the results from $\mathbf{S}_R$ and $\mathbf{S}_L$.

From Fig. 6.10 it is clear that:

- There is a good agreement between low values of Ψ and f_M, with all the geometries with $\Psi \leq 3$ having the lowest values of f_M.
- The failed AVF seem to be equally distributed in all the frequency ranges, however, 3 out of the 4 geometries predicted to have the greatest instabilities did not mature.

In total, 23 geometries were predicted to have $f_M \leq 35$Hz, with 17 geometries having $f_M < 10$Hz, and 15 geometries with $f_M = 0$Hz. The corresponding mean value of Ψ for the 15 steady geometries was 0.14, with Ψ always smaller than 2, while the mean value of Ψ in the other geometries was 38.3 (p-value $< 2.2 \times 10^{-16}$). The average value of Ψ for the geometries having $f_M \leq 35$Hz was 2.6, while the mean value of Ψ for the geometries having $f_M > 35$Hz was 45 (p-value $< 2.2 \times 10^{-16}$). The minimum value of Ψ in the simulations with $f_M > 35$Hz was 14.5.

7/15 simulations (4 RCF and 3 BCF) with $f_M = 0$Hz and 10/23 (6 RCF and 4 BCF) geometries $f_M \leq 35$Hz did not mature, resulting in a failure rate of 47% and 44% respectively, however all the geometries that were predicted to be steady and failed had an inflow lower than 400ml/min, and a resulting average proximal Reynolds number lower than 500. Only one geometry with $f_M \leq 35$Hz had an inflow greater than 400ml/min, and a resulting proximal Reynolds number equal to 761, and it did not fail. The Fisher significance test was performed in R [132] to assess if there was a statistically significant difference between the failure rate of the predicted steady geometries and the rest of the AVF, and it resulted in a non statistically significant difference (p-value 0.17).

7 AVF had a predicted average frequency between the $\mathbf{S}_R$ and $\mathbf{S}_L$ greater than 700Hz, and 4/7 AVF in this group did not mature, with a failure rate of 57%. However, the Fisher significance test resulted in a non statistically significant

difference between the geometries presenting greater unsteadiness and the other AVFs (p-value 0.21).

6.4.1.2 Blood Flow Sensitivity to Geometry Reconstruction

To understand flow sensitivity to the reconstruction method used to obtain geometries in $\mathbf{S}_R$ and in $\mathbf{S}_L$, the perimeters P of different transversal sections in the artery and the vein were compared between the two reconstructed geometries for each patient. If the two geometries were similar, the perimeters rate should be close to 1. The deviation of the perimeters rate from 1 was called $d_P = \sqrt{\sum_i \left(P_R^i/P_L^i - 1\right)^2/N}$, where P_R is the perimeter calculated for the sections of the realistic geometry and P_L the perimeter calculated for the sections of the lofted geometry both in the artery and in the vein. The simulations in $\mathbf{S}_R$ and $\mathbf{S}_L$ were considered to give similar results if both the predicted maximum frequency f_M and the space-time averaged WSS $\boldsymbol{\tau}_{tS}$ gave similar results. More specifically, CFD simulations were considered to be similar if the percentage difference of f_M was lower than 15% and the percentage difference of $\boldsymbol{\tau}_{tS}$ was lower than 10%. In total, 25 geometries had similar results between lofted and reconstructed simulations. Fig. 6.11 show the boxplot for d_P in two groups of simulations: the one leading to similar results and the one leading to different results in the simulated flow.

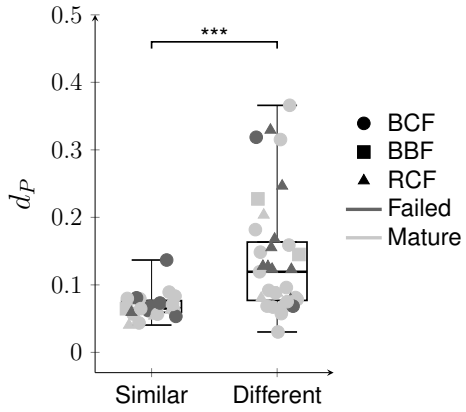


Figure 6.11: Perimeter rate deviation d_P in geometries leading to similar results (Similar) and in geometries leading to different results in the simulated flow (Different). *** indicates a p-value < 0.001.

The average of d_P for the simulations leading to similar results is 0.07, while the average value of d_P for geometries leading to different results is 0.14. The p-value for the difference was calculated in R with a two-sided unpaired t-test and resulted in p-value 4.15×10^{-5}. Results suggest that if $d_P > 0.1$, then the two reconstruction methods would lead to different results. However, 17/35 geometries with high variability on the flow results have $d_P < 0.1$, suggesting that some geometries are more sensitive than others to relatively small variations, and that the relation between reconstruction inaccuracy and flow sensitivity may depend on multiple factors. These results underline the importance of quantifying and studying the geometry uncertainty for each patient specific simulation.

6.4.2 Blood Flow under Average Boundary Conditions

6.4.2.1 Blood Flow Unsteadiness

As explained in Sec. 6.2.5.2, a second set of patient-specific simulations were run with similar boundary conditions (the same average proximal Reynolds number and flow split) to assess the relationship between geometric parameters and blood flow in upper arm AVF (BCF $\cup$ BBF), and in lower arm AVF (RCF). Each

simulation was run for $10\,t_c$, and only Ψ was calculated. Previous results in Sec. 6.4.1.1 suggested that if the value of Ψ averaged between the results in $\mathbf{S}_R$ and $\mathbf{S}_L$ is smaller than 3, then the simulations are steady.

6 simulations were predicted to have averaged $\Psi \leq 3$. Among these, 5/6 simulations were also predicted to have steady flow ($f_M < 35$Hz) in the previous set of simulations. Fig. 6.12 shows the predicted steady geometries coloured by $\overline{\psi}_t(\mathbf{x})$ in S_R and in S_L

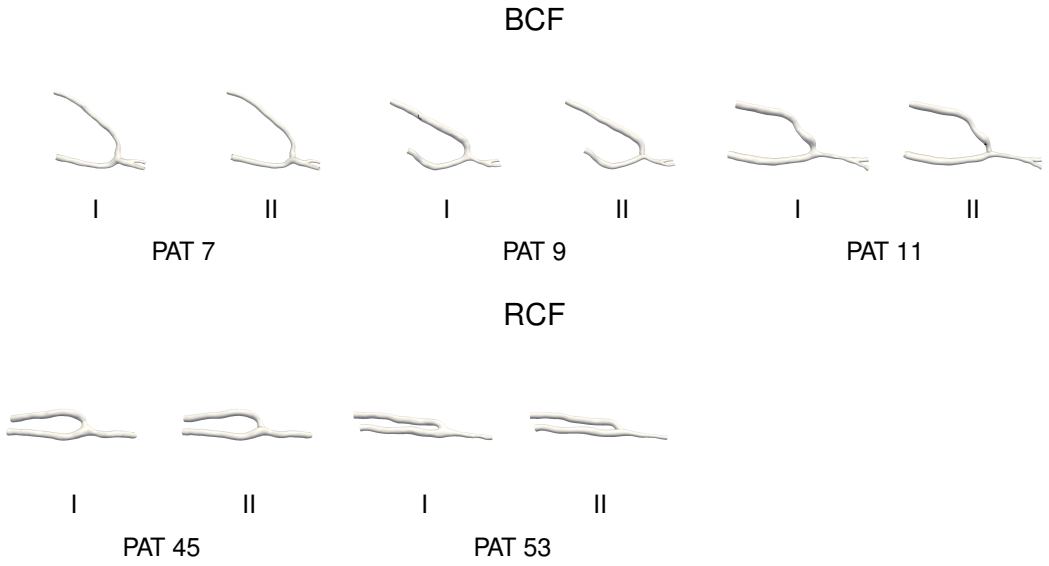
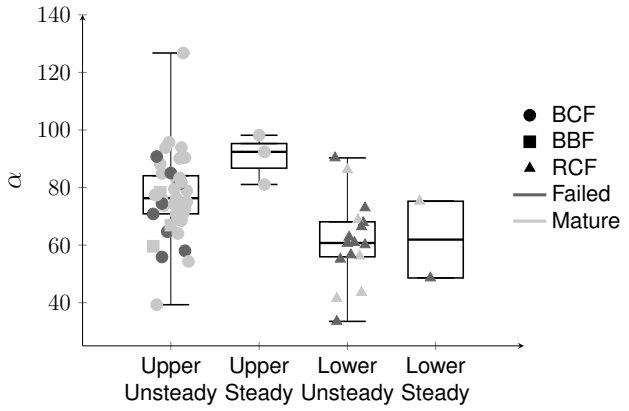


Figure 6.12: Geometries predicted to suppress unsteady flow patterns. (I) Geometry in $\mathbf{S}_R$, (II) Geometry in $\mathbf{S}_L$. All the geometries are coloured by $\overline{\psi}_t(\mathbf{x})$.

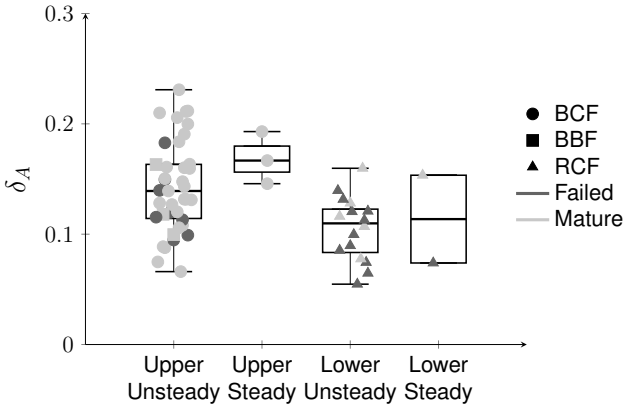
6.4.3 Blood Flow Unsteadiness and Anatomic Variability

Fig. 6.13 shows respectively the values of the anastomotic angle α and the arterial curvature δ_{PA} for the geometries predicted to have steady and unsteady flow in the upper AVFs (BCF∪BBF) and in the lower AVFs (RCF) in all the set of simulations. Fig. 6.14 show respectively the values of the planarity indexes χ_A, χ_V and χ for the same groups. From Fig. 6.13 it appears that the steady BCF have relatively high anastomosis angle, but there is no evident correlation between flow stabilisation and α for the RCF. It seems also that BCF with steady flow

have relatively high arterial curvature. From Fig. 6.14 it seems that BCF with relatively high values of χ_A generate steady flow. On the other hand there is no evident relationship between χ_A and simulated steady flow in RCF. However, none of these correlations are statistically significant because of the small sample size of the subgroups tested.

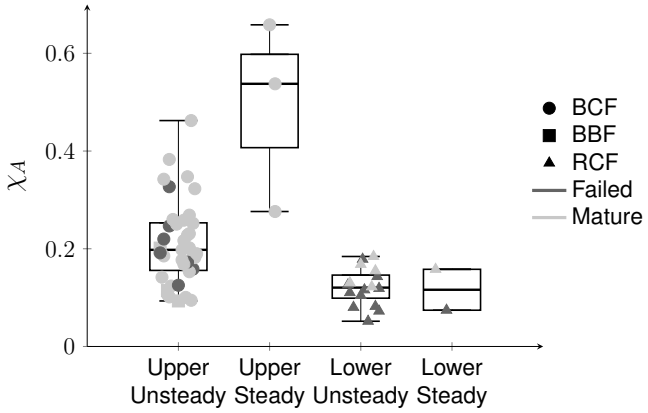


(a)

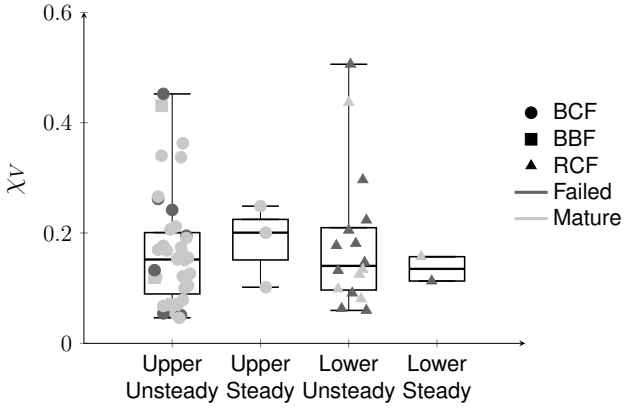


(b)

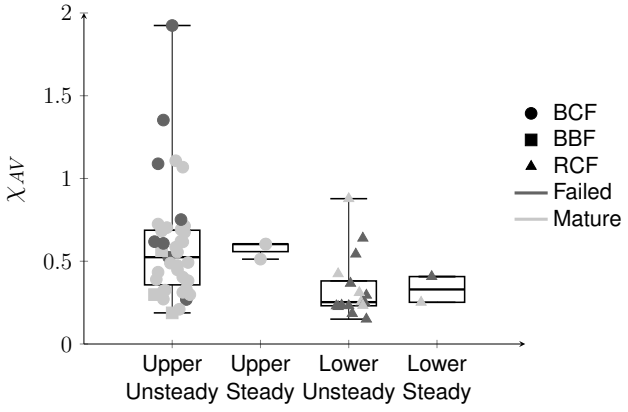
Figure 6.13: (a) Anastomosis angle α (b) arterial average curvature δ_A for AVF with predicted steady and unsteady flow in the upper arm (BCF∪BBF), and in the lower arm (RCF). The AVF that did not mature are coloured in dark grey, while the AVF that matured are coloured in light grey. It seems that the steady BCFs have relatively high anastomosis angle, it seems also that relatively high arterial curvature δ_A may help in stabilising the flow in BCF. However, none of the correlation is statistically significant because of the small sample size of the subgroups tested. There is no preferable values of angle and curvature for the two steady RCFs.



(a)



(b)



(c)

Figure 6.14: (a) arterial planarity index χ_A, (b) venous planarity index χ_V and (c) AVF planarity index χ for AVF with predicted steady and unsteady flow in the upper arm (BCF∪BBF), and in the lower arm (RCF). The AVF that did not mature are coloured in dark grey, while the AVF that matured are coloured in light grey. Only BCFs with relatively high values of χ_A seem to be steady, while there is no preferable χ_A for the steady RCF. None of the possible correlations is statistically significant because of the small sample size of the steady geometries tested.

6.4.4 Blood Flow Unsteadiness and Clinical Outcome

Of the 5 geometries that were predicted to have steady flow with both boundary conditions and both geometric reconstruction methods, only 1 RCF and 0 BCF failed between the 4th to 6th week after surgery. The only RCF steady AVF that failed had a very low measured blood peak flow at day 0 extremely low ($\max_t Q_{PA} = 115$ml/min), which was the lowest systolic flow measured among all the patients, and hence potentially never reached an adequate blood flow for dialysis. A summary of the relationship between steady flow, clinical outcome and AVF position is presented in Tab. 6.4 and in Fig. 6.15

	Steady RCF	Steady BCF ∪ BBF	Unsteady RCF	Unsteady BCF ∪ BBF
Failed	1	0	11	8
Mature	1	3	5	31

Table 6.4: Mature and failed AVF divided by AVF position (upper arm vs lower arm), and predicted unsteady vs steady flow. Between the 5 geometries that were predicted to have steady flow under both the tested boundary conditions, only 1 RCF and 0 BCF failed between 4th and 6th weeks since surgery.

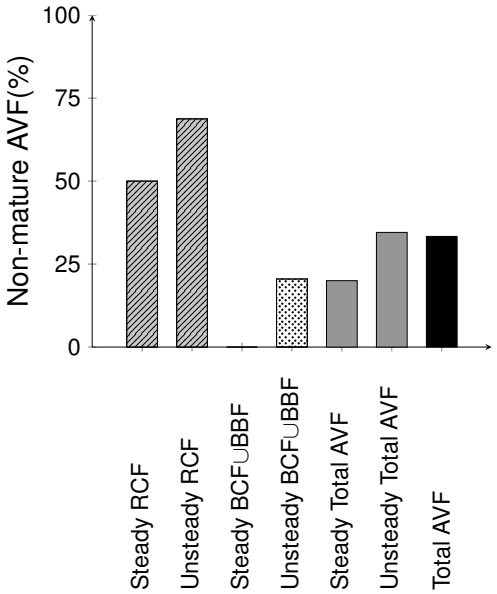


Figure 6.15: AVF failure rate in predicted steady and unsteady RCF (bars with diagonal line); in predicted steady and unsteady BCF (dotted bars); in predicted steady and unsteady total AVF (gray bars); in all AVF (black bar).

The steady geometries seem to have a better outcome compared to the unsteady geometries. However, analysing the results with a Fisher's significance test for the total steady AVF and the total unsteady AVF group, the difference was not found to be statistically significant. Analysis on much wider groups, with possibly pulsatile simualtions, are required to understand whether geometry-induced flow stability may result in a better AVF outcome rate.

6.5 Discussion

In this chapter 60 realistic geometries were analysed, 39 BCF, 18 RCF and 3 BBF, studying their geometric variability. Steady simulations with physiological boundary conditions analysed the nature of the flow inside the AVF, together with the suitability of the geometry reconstruction method. Finally, the possible correlation between the geometric parameters which characterised each AVF and the suppression of unsteady flow was studied under more generic boundary

conditions.

High variability between upper arm (BCF and BBF) AVF and lower arm (RCF) AVF was found. Specifically, lower arm AVF have overall a smaller anastomosis angle, a smaller curvature and more planar arteries than upper arm AVF.

A weak correlation was found between AVF maturation and anastomosis angle, and between AVF maturation and arterial planarity. A stronger correlation was found between maturation and arterial curvature and between maturation and venous diameter. These correlations are all ascribable to the greater RCF failure rate, and it is difficult to assess whether the RCFs are more likely to fail because they have on average smaller venous diameters, smaller anastomosis angles, and more planar and straighter arteries, or if since the RCF, which naturally have smaller diameters, smaller anastomosis angle and more planar and straighter arteries, are more likely to fail for other, uncorrelated, reasons.

The analysis of geometric differences between t_0 and t_1 suggest that AVF maturation causes an enlargement of the venous diameter, which is in line with previous findings [122, 20]. No statistically significant group-wide variations of the other parameters was found between t_0 and t_1, however there can be a high patient-specific variation in single cases.

The results of steady inflow simulations, both under patient-specific boundary conditions and under averaged boundary conditions, suggest that most of the AVF configurations induce unsteady flow. This result is in line with recent findings [67, 68, 70].

The results also suggest that wider anastomosis angle, arterial curvature and vascular non planarity may enhance flow stability only in upper arm AVF, but for RCF the data are unclear. The results for BCF are in line with previous studies [135, 60] that suggested that vascular non-planarity may help in stabilising the flow, and with the optimisation process described in chapter 4, which found steady flows only for wide anastomotic angles. However, the potentially

steady geometries that were found were too few to have a statistically significant correlation.

Different studies [136, 137, 138] have used lofted surfaces with circular cross sections to reconstruct patient specific geometries. The main rationale behind this, is to avoid wall irregularities due to imaging artifacts, and therefore to have a more realistic approximation of the wall. However, already in [125] and in [139] it was found that small geometric variations can highly affect WSS patterns locally. The results presented in this chapter showed that the simulated flow can be highly sensitive to the surface reconstruction method, and that small geometric variations can have a great effect on the nature of the flow for some patient-specific geometries and less for others. The results suggest the importance of quantifying the uncertainties derived by the segmentation approach in patient specific simulations. In addition, in the publication of McGah *et al.* [77] it was suggested that accounting for deformable walls did not have a great effect on the averaged WSS field in AVF. However, fully resolved fluid structure interaction may be needed in geometries that produce flow patterns that are highly sensitive to small geometric variations.

Finally, results suggest that the possibly-steady geometries have lower failure rate than the unsteady ones. However, the correlation is not statistically significant. All the results presented here must be subjected to further scrutiny in a larger study group, which takes into account more physiological boundary conditions at the day of surgery and investigates the suitability of the rigid wall hypothesis.

Chapter 7

Conclusions

The research presented here focused on studying high-frequency flow unsteadiness in idealised and realistic AVF, and on how to suppress this potentially-pathogenic flow characteristic.

In Chapter 3 the effect of realistic arterial curvatures and flow boundary conditions were studied. Results suggested that forming an AVF by connecting a vein onto the outer curvature of an arterial bend does not, necessarily, suppress high-frequency unsteady flow in the artery, contrary to what hypothesised in [1] where idealised geometries and steady boundary conditions were employed. Specifically, during systole, outer configurations appeared more unstable than inner configurations, and whilst this appeared somewhat reversed in diastole, the situation was less clear, and all configurations exhibit a degree of unsteadiness.

In Chapter 4 a new shape was found after optimising idealised geometries for flow unsteadiness under steady boundary conditions. The optimal geometry was successfully tested under the same realistic boundary conditions of Chapter 3, and proved to stabilise the flow. In Chapter 5 the optimal geometry was translated into an extra-vascular device that was tested in a porcine model. Preliminary results suggest that the device can successfully suppress flow unsteadiness, however

the current data is too few to have any statistical significance.

Finally, in Chapter 6 the geometries of 60 patients were studied, knowing their clinical outcome and flow measurements. The patient geometry was analysed through the vascular curvature, the anastomotic angle and a new planarity coefficient. A significant geometry variability was found between AVF in the upper arm and in the lower arm, which may be correlated with the greater patency of upper arm fistula. Blood flow simulations were analysed in in an effort to correlate flow unsteadiness and geometric parameters, however, the number of AVF that seemed to effectively suppress high-frequency flow unsteadiness was too small to find any statistically significant correlation. The geometries that seemed to suppress high-frequency unsteadiness presented a better patency-rate compared to the geometries that seemed more unsteady, however, also in this case, the small number of possible-steady geometries meant that the correlation was not statistically significant. Future work should aim to definitively validate/disprove the relationship between high-frequency flow unsteadiness and AVF patency using both animal models and clinical datasets from wider patient cohorts.

Both animal models and data analysis on a wider patient group should focus on validate/disprove the relationship between high-frequency flow unsteadiness and AVF patency. In particular, the porcine studies described in Chapter 5 should be extended: if they demonstrate that the new device increases AVF patency, it would represent a new validation of the hypothesis that IH is caused by high flow unsteadiness. Moreover, it may lead to further testing of the proposed device in a clinical trial, in the long term possibly resulting in a improvement in AVF patency rates, and improved clinical outcomes. However, even if the animal studies suggest that the new device effectively suppresses flow unsteadiness, but does not increase AVF patency, it would suggest that other mechanisms, such as low TAWSS and hypoxia, may be predominant in the development of IH.

Bibliography

[1] F Iori, L Grechy, R W Corbett, W Gedroyc, N Duncan, C G Caro, and P E Vincent. The effect of in-plane arterial curvature on blood flow and oxygen transport in arterio-venous fistulae. *Physics of Fluids*, 27(3):031903, 2015.

[2] A Grassmann, S Gioberge, S Moeller, and G Brown. ESRD patients in 2004: global overview of patient numbers, treatment modalities and associated trends. *Nephrology, Dialysis, Transplantation*, 20(12):2587–2593, 2005.

[3] G M Fleming. Renal replacement therapy review: past, present and future. *Organogenesis*, 7(1):2–12, 2011.

[4] United States Renal Data System. 2015 USRDS Annual Data Report: Epidemiology of kidney disease in the United States. Volume 2, Chapter 4: Vascular Access. *American Journal of Kidney Diseases*, 67(3):S197–S210, 2015.

[5] ERA-EDTA Registry. ERA-EDTA Registry Annual Report 2013. Technical report, Academic Medical Center, Department of Medical Informatics, Amsterdam, The Netherlands, 2015.

[6] J Webster. *Medical instrumentation: application and design.* Wiley; 4 edition, 2009.

[7] National Kidney Foundation. KDOQI, Clinical practice guidelines for vascular access. *American Journal of Kidney Diseases*, suppl 1(48):S176–S47, 2006.

[8] M J Brescia, J E Cimino, K Appell, B J Hurwich, and B H Scribner. Chronic hemodialysis using venipuncture and a surgically created arteriovenous fistula. *Journal of the American Society of Nephrology*, 10(1):193–199, 1966.

[9] K Konner. History of vascular access for haemodialysis. *Nephrology, Dialysis, Transplantation*, 20(12):2629–35, 2005.

[10] J Tordoir, B Canaud, P Haage, K Konner, A Basci, D Fouque, J Kooman, A Martin-Malo, L Pedrini, F Pizzarelli, J Tattersall, M Vennegoor, C Wanner, P ter Wee, and R Vanholder. Ebpg on vascular access. *Nephrology Dialysis Transplantation*, 22(suppl 2):ii88–ii117, 2007.

[11] T Lee, M Mokrzycki, L Moist, I Maya, M Vazquez, and C E Lok. Standardized definitions for hemodialysis vascular access. *Seminars in Dialysis*, 24(5):515–524, 2011.

[12] K. Konner. The Arteriovenous Fistula. *Journal of the American Society of Nephrology*, 14(6):1669–1680, 2003.

[13] A Besarab. Resolved: fistulas are preferred to grafts as initial vascular access for dialysis. *Journal of the American Society of Nephrology*, 19(9):1629–1631, 2008.

[14] P Roy-Chaudhury, V P Sukhatme, and A K Cheung. Hemodialysis vascular access dysfunction: a cellular and molecular viewpoint. *Journal of the American Society of Nephrology*, 17(4):1112–1127, 2006.

[15] B S Dixon, L Novak, and J Fangman. Hemodialysis vascular access survival: upper-arm native arteriovenous fistula. *American Journal of Kidney Diseases*, 39(1):92–101, 2002.

[16] M Allon and ML L Robbin. Increasing arteriovenous fistulas in hemodialysis patients: problems and solutions. *Kidney International*, 62(4):1109–1124, 2002.

[17] M C Riella and P Roy-Chaudhury. Vascular access in haemodialysis: strengthening the Achilles' heel. *Nature Reviews. Nephrology*, 9(6):348–357, 2013.

[18] S Pastan, J M Soucie, and W M McClellan. Vascular access and increased risk of death among hemodialysis patients. *Kidney International*, 62(2):620–626, 2002.

[19] T C Rothuizen and C Y Wong. Arteriovenous access failure: more than just intimal hyperplasia? *Nephrology Dialysis Transplantation*, 28(5), 2013.

[20] B S Dixon. Why don't fistulas mature? *Kidney International*, 70(8):1413–22, 2006.

[21] A Al-Jaishi, M J Oliver, S M Thomas, C E Lok, J C Zhang, A X Garg, S D Kosa, R R Quinn, and Le M Moist. Patency rates of the arteriovenous fistula for hemodialysis: a systematic review and meta-analysis. *American Journal of Kidney Diseases*, 63(3):464–78, 2014.

[22] P Roy-Chaudhury, L Arend, J Zhang, M Krishnamoorthy, Y Wang, R Banerjee, A Samaha, and R Munda. Neointimal hyperplasia in early arteriovenous fistula failure. *American Journal of Kidney Diseases*, 50(5):782–90, 2007.

[23] W G Schenk. Improving dialysis access: regional anesthesia improves arteriovenous fistula prevalence. *The American Surgeon*, 76(9):938–942, 2010.

[24] L M Dember, G J Beck, and M Allon. Effect of clopidogrel on early failure of arteriovenous fistulas for hemodialysis: A randomized controlled trial. *Journal of the American Medical Association*, 299(18):2164–2171, 2008.

[25] A C Wells, B Fernando, A Butler, E Huguet, J A Bradley, and G J Pettigrew. Selective use of ultrasonographic vascular mapping in the assessment of patients before haemodialysis access surgery. *British Journal of Surgery*, 92(11):1439–1443, 2005.

[26] D Puskar, J Pasini, I Savić, G Bedalov, and Z Sonicki. Survival of primary arteriovenous fistula in 463 patients on chronic hemodialysis. *Croatian Medical Journal*, 43(3):306–311, 2002.

[27] M Allon, M E Lockhart, R Z Lilly, M H Gallichio, C J Young, J Barker, M H Deierhoi, and M L Robbin. Effect of preoperative sonographic mapping on vascular access outcomes in hemodialysis patients. *Kidney International*, 60(5):2013–2020, 2001.

[28] T A Pflederer, S Kwok, B L Ketel, and T Pilgram. A comparison of transposed brachiobasilic fistulae with nontransposed fistulae and grafts in the fistula first era. *Seminars in Dialysis*, 21(4):357–363, 2008.

[29] I D Maya, J C O'Neal, C J Young, J Barker-Finkel, and M Allon. Outcomes of brachiocephalic fistulas, transposed brachiobasilic fistulas, and upper arm grafts. *Clinical Journal of the American Society of Nephrology*, 4(1):86–92, 2009.

[30] A Asif, C Leon, D Merrill, B Bhimani, R Ellis, M Ladino, and F N Gadalean. Arterial steal syndrome: a modest proposal for an old paradigm. *American Journal of Kidney Diseases*, 48(1):88–97, 2006.

[31] M R De Vries, K H Simons, J W Jukema, J Brau, and P H A Quax. Vein graft failure: from pathophysiology to clinical outcomes. *Nature Reviews Cardiology*, 13:451–470, 2016.

[32] T H Spaet, M B Stemerman, F J Veith, and Lejnieks I. Intimal injury and regrowth in the rabbit aorta; medial smooth muscle cells as a source of neointima. *Circulation Research*, 36(1):58–70, 1975.

[33] C G Caro, J. M. Fitz-Gerald, and R. C. Schroter. Arterial wall shear and distribution of early atheroma in man. *Nature*, 223:1159–1161, 1969.

[34] C G Caro, F J M Gerald, and R C Schroter. Atheroma and arterial wall shear observation, correlation and proposal of a shear dependent mass transfer mechanism for atherogenesis. *Proceeding of the Royal Society of London*, 177(1046):109–133, 1971.

[35] V Peiffer, S J Sherwin, and P D Weinberg. Does low and oscillatory wall shear stress correlate spatially with early atherosclerosis? A systematic review. *Cardiovascular Research*, 99(2):242–50, 2013.

[36] F Loth, S A Jones, C K Zarins, D P Giddens, R F Nassar, S Glagov, and H S Bassiouny. Relative contribution of wall shear stress and injury in experimental intimal thickening at PTFE end-to-side arterial anastomoses. *Journal of Biomechanical Engineering*, 124(1):44–51, 2002.

[37] N DePaola, M A. Gimbrone, P F Davies, and C F Dewey. Vascular endothelium responds to fluid shear stress gradients [published erratum appears in Arterioscler Thromb 1993 Mar;13(3):465]. *Arteriosclerosis, Thrombosis, and Vascular Biology*, 12(11):1254–1257, 1992.

[38] J M Dolan, J Kolega, and H Meng. High wall shear stress and spatial gradients in vascular pathology: a review. *Annals of Biomedical Engineering*, 41(7):1411–27, 2013.

[39] D N Ku, D P Giddens, C K Zarins, and S Glagov. Pulsatile flow and atherosclerosis in the human carotid bifurcation. Positive correlation be-

tween plaque location and low oscillating shear stress. *Arteriosclerosis, Thrombosis, and Vascular Biology*, 5(3):293–302, 1985.

[40] H A Himburg, D M Grzybowski, A L Hazel, J A LaMack, X M Li, and M H Friedman. Spatial comparison between wall shear stress measures and porcine arterial endothelial permeability. *American Journal of Physiology. Heart and Circulatory Physiology*, 286(5):H1916–H1922, 2004.

[41] J J Chiu and S Chien. Effects of disturbed flow on vascular endothelium: pathophysiological basis and clinical perspectives. *Physiological Reviews*, 91(1):1–106, 2011.

[42] V Peiffer, S J Sherwin, and P D Weinberg. Computation in the rabbit aorta of a new metric - the transverse wall shear stress - to quantify the multi-directional character of disturbed blood flow. *Journal of Biomechanics*, 46(15):2651–2658, 2013.

[43] Y Mohamied, E M Rowland, E L Bailey, S J Sherwin, M A Schwartz, and P D Weinberg. Change of direction in the biomechanics of atherosclerosis. *Annals of Biomedical Engineering*, 43(1):16–25, 2015.

[44] J M Dolan, F J Sim, H Meng, and J Kolega. Endothelial cells express a unique transcriptional profile under very high wall shear stress known to induce expansive arterial remodeling. *American Journal of Physiology. Cell Physiology*, 302(8):C1109–C1118, 2012.

[45] M S Alnaes, J Isaksen, K A Mardal, B Romner, M K Morgan, and T Ingebrigtsen. Computation of hemodynamics in the circle of Willis. *Stroke*, 38(9):2500–2505, 2007.

[46] I Nathan and A Imparato. Vibrational analysis in experimental models of atherosclerosis. *Bulletin of the New York Acedemy of Medicine*, 53(10):849–868, 1977.

[47] M F Fillinger, E R Reinitz, R a Schwartz, D E Resetarits, a M Paskanik, D Bruch, and C E Bredenberg. Graft geometry and venous intimal-medial hyperplasia in arteriovenous loop grafts. *Journal of Vascular Surgery*, 11(4):556–66, 1990.

[48] P F Davies, A Remuzzi, E J Gordon, C F Dewey, and M A Gimbrone. Turbulent fluid shear stress induces vascular endothelial cell turnover in vitro. *Proceedings of the National Academy of Sciences of the United States of America*, 83(7):2114–2117, 1986.

[49] S Pongkitwitoon, E M Weinheimer-Haus, T J Koh, and S Judex. Low-intensity vibrations accelerate proliferation and alter macrophage phenotype in vitro. *Journal of Biomechanics*, 49(5):793–796, 2016.

[50] F Loth, P F Fisher, N Arslan, C D Bertram, S E Lee, T J Royston, W E Shaalan, and H S Bassiouny. Transitional flow at the venous anastomosis of an arteriovenous graft: potential activation of the ERK1/2 mechanotransduction pathway. *Journal of Biomechanical Engineering*, 125(2):49–61, 2003.

[51] S G E Barker, J E Beesley, P A Baskerville, and J F Martin. The influence of the adventitia on the presence of smooth muscle cells and macrophages in the arterial intima. *European Journal of Vascular and Endovascular Surgery*, 9(2):222–227, 1995.

[52] W C Heuper. Atherosclerosis: the anoxemia theory. *Archives Patholology*, 38:350–364, 1944.

[53] D G Buerk and T K Goldstick. Arterial wall oxygen consumption rate varies spatially. *The American Journal of Physiology*, 243(6):H948–958, 1982.

[54] R Okamoto, M Hatani, M Tsukitani, a Suehiro, M Fujino, N Imai, S Takano, Y Watanabe, and H Fukuzaki. The effect of oxygen on the devel-

opment of atherosclerosis in WHHL rabbits. *Atherosclerosis*, 47(1):47–53, 1983.

[55] S G E Barker, A Talbert, S Cottam, P A Baskerville, and J F Martin. Arterial intimal hyperplasia after occlusion of the adventitial vasa vasorum in the pig. *Arteriosclerosis, Thrombosis, and Vascular Biology*, 13(1):70–77, 1993.

[56] E S Lee, G E Bauer, M P Caldwell, and S M Santilli. Association of artery wall hypoxia and cellular proliferation at a vascular anastomosis. *Journal of Surgical Research*, 91(1):32–37, 2000.

[57] S Misra, A a Fu, D K Rajan, L a Juncos, M A McKusick, H Bjarnason, and D Mukhopadhyay. Expression of hypoxia inducible factor-1 alpha, macrophage migration inhibition factor, matrix metalloproteinase-2 and -9, and their inhibitors in hemodialysis grafts and arteriovenous fistulas. *Journal of Vascular and Interventional Radiology*, 19(2 Part 1):252–259, 2008.

[58] C Lata, D Green, J Wan, S Roy, and S M Santilli. The role of short-term oxygen administration in the prevention of intimal hyperplasia. *Journal of Vascular Surgery*, 58(2):452–429, 2013.

[59] S J Sherwin, O Shah, D J Doorly, J Peirò, Y Papaharilaou, N Watkins, C G Caro, and C L Dumoulin. The influence of out-of-plane geometry on the flow within a distal end-to-side anastomosis. *Journal of Biomechanical Engineering*, 122(1):86–95, 2000.

[60] Y Papaharilaou, D J Doorly, and S J Sherwin. The influence of out-of-plane geometry on pulsatile flow within a distal end-to-side anastomosis. *Journal of Biomechanics*, 35(9):1225–39, 2002.

[61] G Coppola and C G Caro. Oxygen mass transfer in a model three-dimensional artery. *Journa of the Royal Society Interface*, 5(26):1067–1075, 2008.

[62] G Coppola and C G Caro. Arterial geometry, flow pattern, wall shear and mass transport: potential physiological significance. *Journal of the Royal Society, Interface*, 6(35):519–528, 2009.

[63] B Ene-Iordache and A Remuzzi. Disturbed flow in radial-cephalic arteriovenous fistulae for haemodialysis: low and oscillating shear stress locates the sites of stenosis. *Nephrology, Dialysis, Transplantation*, 27(1):358–368, 2012.

[64] B Ene-Iordache, L Cattaneo, G Dubini, and A Remuzzi. Effect of anastomosis angle on the localization of disturbed flow in 'side-to-end' fistulae for haemodialysis access. *Nephrology, Dialysis, Transplantation*, 28(4):997–1005, 2013.

[65] M K Krishnamoorthy, R K Banerjee, Y Wang, J Zhang, A S Roy, S F Khoury, L J Arend, S Rudich, and P Roy-Chaudhury. Hemodynamic wall shear stress profiles influence the magnitude and pattern of stenosis in a pig AV fistula. *Kidney International*, 74(11):1410–1419, 2008.

[66] E Rajabi-Jagahrgh, M K Krishnamoorthy, Y Wang, A Choe, P Roy-Chaudhury, and R K Banerjee. Influence of temporal variation in wall shear stress on intima-media thickening in arteriovenous fistulae. *Seminars in Dialysis*, 26(4):511–519, 2013.

[67] M Bozzetto, B Ene-Iordache, and A Remuzzi. Transitional flow in the venous side of patient-specific arteriovenous fistulae for hemodialysis. *Annals of Biomedical Engineering*, pages 1–14, 2015.

[68] L Botti, K Canneyt, R Kaminsky, T Claessens, R N Planken, P Verdonck, A Remuzzi, and La Antiga. Numerical Evaluation and Experimental Validation of Pressure Drops Across a Patient-Specific Model of Vascular Access for Hemodialysis. *Cardiovascular Engineering and Technology*, 4(4):485–499, 2013.

[69] L D Browne, P Griffin, K Bashar, S R Walsh, E G Kavanagh, and M T Walsh. In vivo validation of the in silico predicted pressure drop across an arteriovenous fistula. *Annals of Biomedical Engineering*, 43(6):1275–1286, 2015.

[70] L D Browne, M T Walsh, and P Griffin. Experimental and numerical analysis of the bulk flow parameters within an arteriovenous fistula. *Cardiovascular Engineering and Technology*, 6(4):450–462, 2015.

[71] A Caiazzo, D Evans, J L Falcone, J Hegewald, E Lorenz, B Stahl, D Wang, J Bernsdorf, B Chopard, J Gunn, R Hose, M Krafczyk, P Lawford, R Smallwood, D Walker, and A Hoekstra. A Complex Automata approach for in-stent restenosis: Two-dimensional multiscale modelling and simulations. *Journal of Computational Science*, 2(1):9–17, 2011.

[72] E Cilla, Mand Peña and M A Martínez. Mathematical modelling of atheroma plaque formation and development in coronary arteries. *Journal of the Royal Society, Interface*, 11:20130866, 2014.

[73] A M Gambaruto, D J Doorly, and T Yamaguchi. Wall shear stress and near-wall convective transport: Comparisons with vascular remodelling in a peripheral graft anastomosis. *Journal of Computational Physics*, 229(14):5339–5356, 2010.

[74] S-W Lee, L Antiga, J D Spence, and D A Steinman. Geometry of the carotid bifurcation predicts its exposure to disturbed flow. *Stroke*, 39(8):2341–2347, 2008.

[75] M Sigovan, V Rayz, W Gasper, H F Alley, C D Owens, and D Saloner. Vascular remodeling in autogenous arterio-venous fistulas by MRI and CFD. *Annals of Biomedical Engineering*, 41(4):657–68, 2013.

[76] P M McGah, D F Leotta, K W Beach, E R Zierler, and A Aliseda. Incomplete restoration of homeostatic shear stress within arteriovenous fistulae. *Journal of Biomechanical Engineering*, 135(1):011005, 2013.

[77] P M McGah, D F Leotta, K W Beach, and A Aliseda. Effects of wall distensibility in hemodynamic simulations of an arteriovenous fistula. *Biomechanics and Modeling in Mechanobiology*, 13(3):679–695, 2014.

[78] A G Brown, Y Shi, A Marzo, C Staicu, I Valverde, P Beerbaum, P V Lawford, and D R Hose. Accuracy vs. computational time: Translating aortic simulations to the clinic. *Journal of Biomechanics*, 45(3):516–523, 2012.

[79] H a Himburg and M H Friedman. Correspondence of low mean shear and high harmonic content in the porcine iliac arteries. *Journal of Biomechanical Engineering*, 128(6):852–6, 2006.

[80] A Marzo, P Singh, P Reymond, N Stergiopulos, U Patel, and R Hose. Influence of inlet boundary conditions on the local haemodynamics of intracranial aneurysms. *Computer Methods in Biomechanics and Biomedical Engineering*, 12(4):431–444, 2009.

[81] J L Lumley. The structure of inhomogeneous turbulent flows. In A M Yaglom and V I Tatarski, editors, *Atmospheric Turbulence and Radio Propagation*, pages 166–178. Nauka, Moscow, 1967.

[82] L Sirovich and J D Rodriguez. Coherent structures and chaos: A model problem. *Physics Letters A*, 120(5):211–214, 1987.

[83] L Grinberg, A Yakhot, and G E Karniadakis. Analyzing transient turbulence in a stenosed carotid artery by proper orthogonal decomposition. *Annals of Biomedical Engineering*, 37(11):2200–2217, 2009.

[84] P J Schmid. Dynamic mode decomposition of numerical and experimental data. *Journal of Fluid Mechanics*, 656:5–28, 2010.

[85] J A Moore and C R Ethier. Oxygen mass transfer calculations in large arteries. *J Biomech Eng*, 119(4):469–475, 1997.

[86] J M Tarbell and Y Qui. *The Biomedical Engineering Handbook, 2nd edn. Arterial wall mass transport: the possible role of blood phase resistance in the localization of arterial disease.* Bronzino, J D and Peterson, D R, CRC Press LLC, 2000 Corporate Blvd, N W, Boca Raton, FL 33431, USA, 2000.

[87] Y Qiu and J M Tarbell. Numerical simulation of oxygen mass transfer in a compliant curved tube model of a coronary artery. *Annals of Biomedical Engineering*, 28(1):26–38, 2000.

[88] K Perktold, A Leuprecht, M Prosi, T Berk, M Czerny, W Trubel, and H Schima. Fluid Dynamics, Wall Mechanics, and Oxygen Transfer in Peripheral Bypass Anastomoses. *Annals of Biomedical Engineering*, 30(4):447–460, 2002.

[89] M R Kaazempur-Mofrad, S Wada, J G Myers, and C R Ethier. Mass transport and fluid flow in stenotic arteries: Axisymmetric and asymmetric models. *International Journal of Heat and Mass Transfer*, 48(22):4510–4517, 2005.

[90] S Tada and J M Tarbell. Oxygen mass transport in a compliant carotid bifurcation model. *Annals of Biomedical Engineering*, 34(9):1389–1399, 2006.

[91] S Tada. Numerical study of oxygen transport in a carotid bifurcation. *Physics in Medicine and Biology*, 55(14):3993–4010, 2010.

[92] X Liu, Y Fan, and X Deng. Effect of spiral flow on the transport of oxygen in the aorta: a numerical study. *Annals of Biomedical Engineering*, 38(3):917–926, 2010.

[93] L Grechy. Cfd for arterio-venous fistulas in haemodialysis. M.s. thesis, Università degli Studi di Roma Tor Vergata, 2013.

[94] P A Yushkevich, J Piven, H C Hazlett, R G Smith, S Ho, J C Gee, and G Gerig. User-guided 3d active contour segmentation of anatomical structures: significantly improved efficiency and reliability. *Neuroimage*, 31(3):1116–1128, 2006.

[95] L Antiga, M Piccinelli, L Botti, B Ene-Iordache, A Remuzzi, and D A Steinman. An image-based modeling framework for patient-specific computational hemodynamics. *Medical and Biological Engineering and Computing*, 46(11):1097–1112, 2008.

[96] W Huberts, A S Bode, W Kroon, R N Planken, J H M Tordoir, F N van de Vosse, and E M H Bosboom. A pulse wave propagation model to support decision-making in vascular access planning in the clinic. *Medical Engineering and Physics*, 34(2):233–248, 2012.

[97] S Sivanesan, T V How, and A Bakran. Sites of stenosis in AV fistulae for haemodialysis access. *Nephrology Dialysis Transplantation*, pages 118–120, 1999.

[98] B K Chandran, P A Yoganathan, and E S Rittgers, editors. *Biofluid Mechanics*. Taylor and Francis, 2007.

[99] R L Whitmore. *Rheology of the circulation*. Pergamon Press, 1 edition, 1968.

[100] X Y Luo and Z B Kuang. A study on the constitutive equation of blood. *Journal of Biomechanics*, 25(8):929–934, 1992.

[101] E W Merrill. Rheology of blood. *Physiological Reviews*, 49(4):863–888, 1969.

[102] Z Kharboutly, V Deplano, E Bertrand, and C Legallais. Numerical and experimental study of blood flow through a patient-specific arteriovenous fistula used for hemodialysis. *Medical Engineering and physics*, 32(2):111–118, 2010.

[103] S Pant, B Fabrèges, J-F Gerbeau, and I Vignon-Clementel. A methodological paradigm for patient-specific multi-scale CFD simulations: from clinical measurements to parameter estimates for individual analysis. *International Journal for Numerical Methods in Biomedical Engineering*, 30(12):1614–1648, 2014.

[104] S C R Dennis and N G MICHAEL. Dual solutions for steady laminar flow through a curved tube. *The Quarterly Journal of Mechanics and Applied Mathematics*, 35(3):305–324, 1982.

[105] B Klitzman, A S Popel, and B R Duling. Oxygen transport in resting and contracting hamster cremaster muscles: Experimental and theoretical microvascular studies. *Microvascular Research*, 25(1):108 – 131, 1983.

[106] H Masuda, Y J Zhuang, T M Singh, K Kawamura, M Murakami, C K Zarins, and S Glagov. Adaptive remodeling of internal elastic lamina and endothelial lining during flow-induced arterial enlargement. *Arteriosclerosis, Thrombosis, and Vascular Biology*, 19(10):2298–2307, 1999.

[107] E Sho, M Sho, T M Singh, C Xu, C K Zarins, and H Masuda. Blood flow decrease induces apoptosis of endothelial cells in previously dilated arteries

resulting from chronic high blood flow. *Arteriosclerosis, Thrombosis, and Vascular Biology*, 21(7):1139–1145, 2001.

[108] E Sho, H Nanjo, M Sho, M Kobayashi, M Komatsu, K Kawamura, C Xu, C K Zarins, and H Masuda. Arterial enlargement, tortuosity, and intimal thickening in response to sequential exposure to high and low wall shear stress. *Journal of Vascular Surgery*, 39(3):601–612, 2004.

[109] C Irace, C Cortese, E Fiaschi, C Carallo, E Farinaro, and A Gnasso. Wall shear stress is associated with intima-media thickness and carotid atherosclerosis in subjects at low coronary heart disease risk. *Stroke*, 35(2):464–468, 2004.

[110] D D Heistad, M L Marcus, G E Larsen, and M L Armstrong. Role of vasa vasorum in nourishment of the aortic wall. *The American journal of physiology*, 240:H781–H787, 1981.

[111] R J Paul. The cardiovascular system: vascular smooth muscle. In D F Bohr, A P Somlyo, H V Sparks, and S R Geiger, editors, *Handbook of Physiology*. American Physiological Society, 1980.

[112] C G Caro, T J Pedley, and R C Schroter. *The Mechanics of the Circulation*. Cambridge University Press, 2011.

[113] C Audet and J E Dennis. Mesh adaptive direct search algorithms for constrained optimization. *SIAM Journal on Optimization*, 17(1):188–217, 2006.

[114] C Audet, A L Custódio, and J E Dennis. Erratum: Mesh adaptive direct search algorithms for constrained optimization. *SIAM Journal on Optimization*, 18(4):1501–1503, 2008.

[115] J Sacks, W J Welch, T J Mitchell, and H P Wynn. Design and analysis of computer experiments. *Statistical Science*, 4(4):409—-423, 1989.

[116] A J Booker, J E Dennis, P D Frank, D B Serafini, V Torczon, and M W Trosset. A Rigorous framework for optimization of expensive functions by surrogates. *Structural Optimization*, 17(1):1–13, 1998.

[117] A L Marsden, J A Feinstein, and C A Taylor. A computational framework for derivative-free optimization of cardiovascular geometries. *Computer Methods in Applied Mechanics and Engineering*, 197(21–24):1890–1905, 2008.

[118] W Yang, J a Feinstein, S C Shadden, I E Vignon-Clementel, and A L Marsden. Optimization of a Y-graft design for improved hepatic flow distribution in the fontan circulation. *Journal of Biomechanical Engineering*, 135(January):011002, 2013.

[119] W Yang, J A Feinstein, and A L Marsden. Constrained optimization of an idealized Y-shaped baffle for the Fontan surgery at rest and exercise. *Computer Methods in Applied Mechanics and Engineering*, 199(33-36):2135–2149, 2010.

[120] T J Gundert, A L Marsden, W Yang, and J F LaDisa. Optimization of cardiovascular stent design using computational fluid dynamics. *Journal of Biomechanical Engineering*, 134(January):011002, 2012.

[121] N W Bressloff, G Ragkousis, and N Curzen. Design optimisation of coronary artery stent systems. *Annals of Biomedical Engineering*, 44(2):357–367, 2016.

[122] A Caroli, S Manini, L Antiga, K Passera, B Ene-Iordache, S Rota, G Remuzzi, A Bode, J Leermakers, F N van de Vosse, R Vanholder, M Malovrh, J Tordoir, and A Remuzzi. Validation of a patient-specific hemodynamic computational model for surgical planning of vascular access in hemodialysis patients. *Kidney International*, 84(6):1237–45, 2013.

[123] S Sivanesan, T V How, and A Bakran. Characterizing flow distributions in AV fistulae for haemodialysis access. *Nephrology Dialysis Transplantation*, 13:3108–3110, 1998.

[124] S Lophaven, H Nielsen, and J Søondergaard. DACE: A MATLAB Kriging toolbox version 2.0. Technical Report IMM-REP-2002-12, Informatics and mathematical modelling, technical university of Denmark, 2002.

[125] S Hammer, A Jeays, P L Allan, R Hose, D Barber, W J Easson, and P R Hoskins. Acquisition of 3-D Arterial Geometries and Integration with Computational Fluid Dynamics. *Ultrasound in Medicine and Biology*, 35(12):2069–2083, 2009.

[126] W Schroeder, K Martin, and B Lorensen. *The Visualization Toolkit: An Object-oriented Approach to 3D Graphics*. Kitware, 2006.

[127] M D Ford, Y Hoi, M Piccinelli, L Antiga, and D A Steinman. An objective approach to digital removal of saccular aneurysms: technique and applications. *The British Journal of Radiology*, 82(Spec No 1):S55–S61, 2009.

[128] J Marsden and A Weinstein. *Calculus III*. Springer-Verlag, 2000.

[129] T Lewiner, J D Gomes, H Lopes, and M Craizer. Curvature and torsion estimators based on parametric curve fitting. *Computers & Graphics*, 29(5):641–655, 2005.

[130] D W Holdsworth, C J D Norley, R Frayne, D A Steinman, and B K Rutt. Characterization of common carotid artery blood-flow waveforms in normal human subjects Characterization of common carotid artery blood-flow waveforms in normal human subjects. *Physiological Measurement*, 20(3):219–240, 1999.

[131] R S Rosenson, A McCormick, and E F Uretz. Distribution of blood viscosity values and biochemical correlates in healthy adults. *Clinical Chemistry*, 42(8 Pt 1):1189–95, 1996.

[132] R Core Team. *R: A Language and Environment for Statistical Computing*. R Foundation for Statistical Computing, Vienna, Austria, 2016.

[133] N Sadaghianloo, E Jean-Baptiste, K Rajhi, E François, S Declemy, A Dardik, and R Hassen-Khodja. Increased reintervention in radial-cephalic arteriovenous fistulas with anastomotic angles of less than 30 degrees. *Journal of Vascular Surgery*, pages 1–7, 2015.

[134] J B Thomas, L Antiga, S L Che, J S Milner, D A H Steinman, J D Spence, B K Rutt, and D A Steinman. Variation in the carotid bifurcation geometry of young versus older adults: implications for geometric risk of atherosclerosis. *Stroke*, 36(11):2450–2456, 2005.

[135] C G Caro, D J Doorly, M Tarnawski, K T Scott, Q Long, and C L Dumoulin. Non-planar curvature and branching of arteries and non-planar-type Flow. *Proceedings of the Royal Society A: Mathematical, Physical and Engineering Sciences*, 452(1944):185–197, jan 1996.

[136] T J Gundert, S C Shadden, A R Williams, B K Koo, J Feinstein, and J F Ladisa. A rapid and computationally inexpensive method to virtually implant current and next-generation stents into subject-specific computational fluid dynamics models. *Annals of Biomedical Engineering*, 39(5):1423–1437, 2011.

[137] A L Marsden, V Mohan Reddy, S C Shadden, F P Chan, C Taylor, and J Feinstein. A new multiparameter approach to computational simulation for fontan assessment and redesign. *Congenital Heart Disease*, 5:104–117, 2010.

[138] J P Ku, M T Draney, F R Arko, W A Lee, F P Chan, N J Pelc, C K Zarins, and C A Taylor. In vivo validation of numerical prediction of blood flow in arterial bypass grafts. *Annals of Biomedical Engineering*, 30(6):743–752, 2002.

[139] P E Vincent, A M Plata, A A E Hunt, P D Weinberg, and S J Sherwin. Blood flow in the rabbit aortic arch and descending thoracic aorta. *Journal of the Royal Society, Interface*, 8(65):1708–1719, 2011.

Appendix A

A.1 Simple Kriging

The Simple Kriging method implemented in the dace toolbox [124] is described. Given a deterministic response $y(\mathbf{x})$, which relates $\mathbb{R}^n \rightarrow \mathbb{R}$, where n is the parameter space dimension, the Kriging surrogate model $\hat{y}$ will express $y(\mathbf{x})$ as a realization of a random function that includes a regression model $\mathcal{F}$ and a stochastic process $\mathcal{Z}$

$$\hat{y}(\mathbf{x}) = \mathcal{F}(\boldsymbol{\beta}, \mathbf{x}) + \mathcal{Z}(\mathbf{x}), \tag{A.1}$$

where $\mathcal{F}(\boldsymbol{\beta}, \mathbf{x}) = \sum_{j=1}^{p} \beta_j f_j(\mathbf{x}) = \mathbf{f}'\boldsymbol{\beta}$, and β_j are the regression parameters. The random process $\mathcal{Z}(\cdot)$ is assumed to have mean zero and covariance between $\mathcal{Z}(\boldsymbol{\omega})$ and $\mathcal{Z}(\mathbf{x})$

$$E[\mathcal{Z}(\boldsymbol{\omega}), \mathcal{Z}(\mathbf{x})] = \sigma^2 R(\boldsymbol{\omega}, \mathbf{x}), \tag{A.2}$$

where σ^2 is the process variance and R the correlation. Now let's suppose that $\hat{y}$ is a linear predictor of y, which means that, given m design data $\mathbf{S} = [s_1, ..., s_m]$ and responses $\mathbf{y}_S = [y_1, ..., y_m]$, the predictor

$$\hat{y}(\mathbf{x}) = \mathbf{c}'\mathbf{y}_S, \tag{A.3}$$

with $\mathbf{c} = \mathbf{c}(\mathbf{x}) \in \mathbb{R}^m$. The error

$$\begin{aligned} \hat{y}(\mathbf{x}) - y(\mathbf{x}) &= \mathbf{c}'\mathbf{y}_S - y((x)) \\ &= \mathbf{c}'(\mathbf{F}\boldsymbol{\beta} + \mathbf{Z}) - (\mathbf{f}'\boldsymbol{\beta} + z) \\ &= \mathbf{c}'\mathbf{Z} - z + (\mathbf{F}'\mathbf{c} - \mathbf{f})'\boldsymbol{\beta}, \end{aligned} \tag{A.4}$$

where $\mathbf{F}$ is a matrix $m \times p$ with $F_{ij} = f_j(\mathbf{s}_i)$, and $\mathbf{Z} = [z_1, ..., z_m]'$ are the errors at the design sites. To keep the predictor unbiased

$$\mathbf{F}'\mathbf{c} = \mathbf{f}. \tag{A.5}$$

Therefore, the mean square error (MSE) of the predictor is:

$$\begin{aligned} MSE = E\left[(\hat{y}(\mathbf{x}) - y(\mathbf{x}))^2\right] &= E\left[(\mathbf{c}'\mathbf{Z} - z)^2\right] \\ &= E\left[z^2 + \mathbf{c}'\mathbf{Z}\mathbf{Z}'\mathbf{c} - 2\mathbf{c}'\mathbf{Z}z\right] \\ &= \sigma^2(1 + \mathbf{c}'\mathbf{R}\mathbf{c} - 2\mathbf{c}'\mathbf{r}), \end{aligned} \tag{A.6}$$

with $\mathbf{R}$ the correlation matrix, where $R_{ij} = R(\mathbf{s_i}, \mathbf{s_j})$, and $\mathbf{r}$ the correlation array where the element $r_j = R(\mathbf{s_i}, \mathbf{x})$. The Lagrangian function to minimise Eq. A.6 is

$$\mathcal{L}(\mathbf{c}, \lambda) = \sigma^2(1 + \mathbf{c}'\mathbf{R}\mathbf{c} - 2\mathbf{c}'\mathbf{r}) - \boldsymbol{\lambda}'(\mathbf{F}'\mathbf{c} - \mathbf{f}), \tag{A.7}$$

$$\nabla_{\mathbf{c}}\mathcal{L}(\mathbf{c}, \boldsymbol{\lambda}) = 2\sigma^2(\mathbf{R}\mathbf{c} - \mathbf{r}) - \mathbf{F}\boldsymbol{\lambda}, \tag{A.8}$$

having Eq. A.5 as an unbiased constrained, the following system needs to be solved

$$\begin{bmatrix} \mathbf{R} & \mathbf{F} \\ \mathbf{F}' & \mathbf{0} \end{bmatrix} \begin{bmatrix} \mathbf{c} \\ \widetilde{\boldsymbol{\lambda}} \end{bmatrix} = \begin{bmatrix} \mathbf{r} \\ \mathbf{f} \end{bmatrix}, \tag{A.9}$$

with $\widetilde{\boldsymbol{\lambda}} = \boldsymbol{\lambda}/(2\sigma^2)$ which has solution

$$\begin{aligned} \widetilde{\boldsymbol{\lambda}} &= (\mathbf{F}'\mathbf{R}^{-1}\mathbf{F})^{-1}(\mathbf{F}'\mathbf{R}^{-1}\mathbf{r} - \mathbf{f}), \\ \mathbf{c} &= \mathbf{R}^{-1}(\mathbf{r} - \mathbf{F}\widetilde{\boldsymbol{\lambda}}). \end{aligned} \tag{A.10}$$

From Eq. A.10 and A.3

$$\begin{aligned} \hat{y}(\mathbf{x}) &= (\mathbf{R}^{-1}(\mathbf{r} - \mathbf{F}(\mathbf{F}'\mathbf{R}^{-1}\mathbf{F})^{-1}(\mathbf{F}'\mathbf{R}^{-1}\mathbf{r} - \mathbf{f}))'\mathbf{y}_S \\ &= \mathbf{r}'\mathbf{R}^{-1}\mathbf{y}_S - (\mathbf{F}'\mathbf{R}^{-1}\mathbf{r} - \mathbf{f})'(\mathbf{F}'\mathbf{R}^{-1}\mathbf{F})^{-1}\mathbf{F}'\mathbf{R}^{-1}\mathbf{y}_S. \end{aligned} \tag{A.11}$$

For the regression problem

$$\mathbf{F}\boldsymbol{\beta} \simeq \mathbf{y}_S, \tag{A.12}$$

the generalized least square solution respect to $\mathbf{R}$ will be

$$\boldsymbol{\beta}^* = (\mathbf{F}'\mathbf{R}^{-1}\mathbf{F})^{-1}\mathbf{F}'\mathbf{R}^{-1}\mathbf{y}_S, \tag{A.13}$$

therefore the predictor $\hat{y}(\mathbf{x})$ will be

$$\hat{y}(\mathbf{x}) = \mathbf{f}'\boldsymbol{\beta}^* + \mathbf{r}'\mathbf{R}^{-1}(\mathbf{y}_S - \mathbf{F}\boldsymbol{\beta}^*) = \mathbf{f}'\boldsymbol{\beta}^* + \mathbf{r}'\boldsymbol{\gamma}^*. \tag{A.14}$$

To obtain the MSE associated with the prediction, an estimate of σ^2 is required. The maximum likelihood estimate of the variance results in

$$\sigma^2 = \frac{1}{n}(\mathbf{y}_S - \mathbf{F}\boldsymbol{\beta})'\mathbf{R}^{-1}(\mathbf{y}_S - \mathbf{F}\boldsymbol{\beta}). \tag{A.15}$$

In this work the correlation function is assumed to be of the form $R = \exp\left(\sum_{j=1}^{n} -\theta_j|x_j - s_{ij}|\right)$, with x_j the jth component of $\mathbf{x}$, and the parameters $\boldsymbol{\theta} = [\theta_1, ..., \theta_n]$ are obtained via an optimisation problem from the seeding parameters inside the dace toolbox [124]. The regression function used was a 0-order

regression function, which means that $y(\mathbf{x}) = \sum_{j=1}^{p} \beta_j + z(\mathbf{x})$.

A.2 Dynamic Mode Decomposition

Dynamic Mode Decomposition (DMD) was introduced by Schmid in 2010 [84]. Given $\mathbf{v}(\mathbf{x}, t)$, a function of space $\mathbf{x}$ and time t, a series of measurements of $\mathbf{v}(\mathbf{x}, t)$ will be referred to $\mathbf{V}_1^N = \{\mathbf{v_1}, \mathbf{v_2}, \mathbf{v_3}, ..., \mathbf{v_N}\}$, where N is the number of snapshots and $\mathbf{v_i}$ the array containing the M measurements in space at time i and $i \in [1, N]$. DMD will generate a set of spatial basis functions Φ of $\mathbf{V}_1^N$, with an associated frequency intensity γ.

The goal of DMD, is to extract the dynamic characteristics of $\mathbf{v}(\mathbf{x}, t)$ through a linear mapping $\mathbf{A}$ calculated from $\mathbf{V}_1^N$. Specifically, it is assumed that, beyond a critical number of snapshots, as $\mathbf{V}_1^N$ captures the dominant features of the process, there is a linear mapping $\mathbf{A}$ which connects $\mathbf{v_{i+1}}$ and $\mathbf{v_i}$, that is

$$\mathbf{v_{i+1}} = \mathbf{A}\mathbf{v_i}, \tag{A.16}$$

and that this mapping is the same over the full sampling interval. Subsequently, $\mathbf{V}_1^N$ can be rewritten as:

$$\mathbf{V}_1^N = \{\mathbf{v_1}, \mathbf{A}\mathbf{v_1}, \mathbf{A}^2\mathbf{v_1}, ..., \mathbf{A}^{N-1}\mathbf{v_1}\}. \tag{A.17}$$

When there are enough snapshots, such that adding further $\mathbf{v}_i$ will not improve the vector space spanned by $\mathbf{V}_1^N$, it is assumed that $\mathbf{v}_N$ can be expressed as a combination of the previous vectors $\mathbf{v}_i$, where $i \in [1, N-1]$ and the vectors $\mathbf{v}_i$ are linearly independent.

$$\mathbf{v}_N = a_1\mathbf{v}_1 + a_2\mathbf{v}_2 + ... + a_{N-1}\mathbf{v}_{N-1} + \mathbf{r}, \tag{A.18}$$

can be expressed as:

$$\mathbf{v}_N = \mathbf{V}_1^{N-1}\mathbf{a} + \mathbf{r}, \tag{A.19}$$

with $\mathbf{a} = \{a_1, a_2, ..., a_{N-1}\}^T$ and $\mathbf{r}$ is the residual vector. Therefore,

$$\mathbf{A}\mathbf{V}_1^{N-1} = \{\mathbf{v}_2, \mathbf{v}_3, ..., \mathbf{v}_N\} = \mathbf{V}_1^{N-1}\mathbf{S} + \mathbf{R}, \tag{A.20}$$

with $\mathbf{R} = \mathbf{r}\mathbf{e}_{N-1}^T$, and $\mathbf{e}_{N-1}$ is the $(N-1)$ unit vector, and $\mathbf{S}$ a companion matrix of the form

$$\mathbf{S} = \begin{pmatrix} 0 & & & & & & a_1 \\ 1 & 0 & & & & & a_2 \\ & . & . & & & & . \\ & & . & . & & & . \\ & & & . & . & & . \\ & & & & 1 & 0 & a_{N-2} \\ & & & & & 1 & a_{N-1} \end{pmatrix}. \tag{A.21}$$

The only unknowns in $\mathbf{S}$ are the coefficients a_i of the last column. $\mathbf{S}$ can be computed through the least-square solution of Eq. A.18, which gives

$$\mathbf{a} = \mathbf{R}^{-1}\mathbf{Q}^H\mathbf{v}_N, \tag{A.22}$$

where $\mathbf{Q}^H$ is the conjugate transpose of the matrix $\mathbf{Q}$, and where $\mathbf{QR}$ are the QR decomposition of the data sequence $\mathbf{V}_1^{N-1}$. However, if the data are contaminated with noise, or other uncertainties, it is possible to obtain ill-conditioned results. Therefore, the DMD implements a pre-processing step, where first $\mathbf{V}_1^{N-1}$ is decomposed through an SVD decomposition in

$$\mathbf{V}_1^{N-1} = \mathbf{U}\mathbf{\Sigma}\mathbf{W}^H, \tag{A.23}$$

when substituted into Eq. A.20 gives

$$\mathbf{U}^H\mathbf{A}\mathbf{U} = \mathbf{U}^H\mathbf{V}_2^N\mathbf{W}\mathbf{\Sigma}^{-1} \equiv \widetilde{\mathbf{S}}, \tag{A.24}$$

where $\widetilde{\mathbf{S}}$ is a full matrix related to $\mathbf{S}$ by a similarity transformation, and $\mathbf{V}_2^N$ is the matrix $\{\mathbf{v}_2, \mathbf{v}_3, ..., \mathbf{v}_N\}$.

The DMD spatial modes Φ_i are defined as:

$$\Phi_i = \mathbf{U}\mathbf{y}_i, \tag{A.25}$$

where $\mathbf{y}_i$ is the *ith* eigenvector of $\widetilde{\mathbf{S}}$, i.e. $\widetilde{\mathbf{S}}\mathbf{y}_i = \lambda_i\mathbf{y}_i$.

By definition, the eigenvalues of $\widetilde{\mathbf{S}}$ are an approximation of the eigenvalues of the Koopman operator $\mathbf{A}$, The DMD intensities γ_i associated to each spatial mode Φ_i are calculated from the equation

$$\mathbf{v}_1 = \sum_{i=1}^{N} \Phi_i\gamma_i + \rho, \tag{A.26}$$

where ρ is a residual vector, and are obtained through a least square method.

From Eq. A.26 and Eq. A.16

$$\mathbf{v}_k = \sum_{i=1}^{N} \lambda_i^k\Phi_i\gamma_i. \tag{A.27}$$

From Eq. A.27, the frequency equivalent to the *ith* spatial mode will be defined as:

$$f_i = \mathrm{Im}(\mathbf{log}(\lambda_i))/(2\pi\Delta t), \tag{A.28}$$

where Im() indicates the imaginary part.